

# PORTUGALIAE PHYSICA

VOLUME 21

FASC. 1/2

1992

SOCIEDADE PORTUGUESA DE FÍSICA

## PORTUGALIAE PHYSICA

Fundada em 1943 por A. Cyrillo Soares, M. Telles Antunes, A. Marques da Silva e M. Valadares

### *Director*

J. M. Machado da Silva (Faculdade de Ciências, Universidade do Porto)

### *Co-Directores*

M. Salete Leite (Faculdade de Ciências, Universidade de Coimbra)

Alexandre Quintanilha (ICBAS, Universidade do Porto)

### *Directores-Adjuntos*

Olivério Soares (Faculdade de Ciências, Universidade do Porto)

Maria Helena Vaz de Carvalho Nazaré (Universidade de Aveiro)

Teresa Mora (Universidad Autónoma de Barcelona)

Margarida Costa (Universidade de Coimbra)

J. Bartolomé (Universidad de Zaragoza)

### *Comissão Redactorial*

B. Barbara (Laboratório Louis Néel, CNRS — Grenoble)

Kim Carneiro (Instituto Dinamarquês de Metrologia. Lingby)

F. Bragança Gil (Faculdade de Ciências, Universidade de Lisboa)

I. R. Harris (Departamento de Metalurgia, Universidade de Birmingham)

M. Salete Leite (Faculdade de Ciências, Universidade de Coimbra)

N. Miura (Instituto de Física do Estado Sólido, Universidade de Tokyo)

M. Ida (Faculdade de Ciências, Universidade de Kobe)

F. D. Santos (Faculdade de Ciências, Universidade de Lisboa)

J. M. Machado da Silva (Faculdade de Ciências, Universidade do Porto)

J. B. Sousa (Faculdade de Ciências, Universidade do Porto)

R. Stinchcombe (Departamento de Física Teórica, Universidade de Oxford)

M. Velarde (Faculdade de Ciências, UNED — Madrid)

J. P. Burger (Université de Paris, Orsay)

F. R. N. Nabarro (University of Witwatersrand, Johannesburg)

### *Anteriores Directores*

A. Cyrillo Soares (1943-1949), A. Monteiro (1951-1954)

A. da Silveira (1965-1975), J. M. Araújo (1979-1986)

ISSN 0048 - 4903

PORTUGALIAE  
PHYSICA

VOLUME 21

FASC. 1/2

1992

117



## ENHANCED NUCLEAR MAGNETISM

B. BLEANEY

Clarendon Laboratory, Parks Road, Oxford, U.K. OX1 3PU

[Received March 1992]

**ABSTRACT**-Enhanced nuclear magnetism is of particular interest in Van Vleck paramagnets, in which the electronic ground state is a singlet or non-Kramers doublet. The enhancement of the nuclear moment arises through admixture of electronic magnetic moment by the hyperfine interaction. Magnetic resonance measurements on ions of the lanthanide group, using both electromagnetic and acoustic waves, are surveyed. In some compounds an ordered magnetic state is observed at milliKelvin temperatures.

### 1- PREFACE

The earliest direct measurements of atomic magnetic moments were based on the deflection of atoms by a magnetic field gradient [1, 2]. The results agreed with values from optical Zeeman spectroscopy, and with those calculated from the orbital and spin magnetic moments, interacting through the spin-orbit coupling. Values of nuclear magnetic moments were deduced indirectly from optical spectroscopic measurements of the hyperfine interaction. It soon became apparent that nuclear moments

were not easily predictable, nor simply related to the nuclear magneton, even for the proton with spin  $1/2$ . The neutron, though an uncharged particle, was also found to have spin  $1/2$ , and a magnetic moment.

In 1939 Rabi [3] took the bold step of making direct measurements of nuclear moments by magnetic resonance, detected through changes in the deflection of molecular beams by magnetic field gradients. Interrupted by the second world war, this method was overtaken by simpler radio-frequency techniques, but the use of atomic or molecular

beams continued to be developed for measurements of many kinds; a detailed account is given by Ramsey [4]. High precision can be obtained, and since 1963 [5] the unit of time has been defined as the interval containing exactly 9 192 631 770 cycles of the hyperfine frequency in zero magnetic field of the stable isotope (mass 133) of the caesium atom.

In 1944-6, two forms of magnetic resonance in condensed matter were developed independently. The first electron

paramagnetic resonance (EPR) experiments were carried out in the U.S.S.R. by Zavoisky [6] on manganese ions in solution and in solids. The electronic magnetic moment is much greater than any nuclear moment, and the frequencies used by Zavoisky were of order 500 MHz. These measurements were made at room temperature, where spin-lattice relaxation rates are sufficiently fast to allow the electron spins to reach thermal equilibrium, even in a solid.

n	Configuration	Atom	Divalent ion	Trivalent ion	$\xi_J$
2	$^3H_4$	-	-	$Pr^{3+}$	0.805
4	$^5I_4$	Nd	$Nd^{2+}$	$Pm^{3+}$	0.603
6	$^7F_0$	Sm	$Sm^{2+}$	$Eu^{3+}$	
8	$^7F_6$	-	-	$Tb^{3+}$	1.492
10	$^5I_8$	Dy	$Dy^{2+}$	$Ho^{3+}$	1.242
12	$^3H_6$	Er	-	$Tm^{3+}$	1.164

Table 1. Ground configuration for some non-Kramers atoms and ions of the 4f group, with n electrons in the 4f shell. Note that the atoms, not the ions, also have two electrons filling the 6s shell. Values of  $\xi_J$  are rounded to the third decimal place.

In condensed matter, nuclear magnetic resonance (NMR) was observed in the U.S.A. at frequencies of order 10 to 50 MHz [7, 8]. The nuclei were protons in water, the advantage of a liquid with low viscosity being that the resonance

lines have an exceedingly small width because of motional narrowing. A further important point is that spin-lattice relaxation rates are not prohibitively slow, as would be expected in a solid. Early efforts by Gorter [9] to observe

NMR at low temperatures in solids were defeated by excessively long times to achieve thermal equilibrium. The first successful experiments below room temperature were in Oxford [10] and extended to protons in liquid hydrogen at 20 K [11].

The effects considered in this review involve both nuclear and electronic moments, coupled together through the large magnetic field exerted on the nucleus by the surrounding atomic electrons - the hyperfine interaction. Such effects occur quite generally, but this article is concerned mainly with the rare earth group, with magnetic electrons in the 4f shell. For the trivalent ions the

electronic configurations are listed in Table 1.

Most ions of the lanthanide group have stable isotopes of odd mass. Nuclei with an odd number of protons have a single stable isotope with a large nuclear magnetic moment; the exceptions are La, Eu & Yb, that each have two stable isotopes. Nearly all the nuclei with an even number of protons have a range of isotopes, mostly of even mass and nuclear spin  $I = 0$ , but with some isotopes of odd mass; these have nuclear spins and relatively small nuclear moments. Table 2 lists their mass, spin, unenhanced magnetic resonance frequency and hyperfine interaction constant.

Ion	Isotope	I	$\gamma_I/2\pi$ MHzT <sup>-1</sup>	$A_J/h$ MHz
Pr	141	5/2	+12.93	+1093
Sm	147	7/2	-1.76	-240
	149	7/2	-1.45	-193
Eu	151	5/2	+10.49	-
	153	5/2	+4.63	-
Tb	159	3/2	+10.13	+530
Ho	165	7/2	+8.99	+812
Tm	169	1/2	-3.49	-394

Table 2. Nuclear data for the trivalent lanthanide ions mentioned in the text. Values of the isotopic mass, the nuclear spin I, the unenhanced nuclear resonance frequency  $\gamma_I/2\pi$  in a field of 1 tesla, and the hyperfine interaction  $A_J/h$ .

## 2. THEORY

Most free atoms possess electronic magnetic moments, while many nuclei have moments, smaller by a factor of order  $10^{-3}$ . In chemical compounds, a few gases ( $O_2$ , NO,  $NO_2$ ) are paramagnetic, but permanent magnetic moments are generally restricted to transition group ions with partly filled 3d, 4d, 5d, 4f or 5f electron shells.

For electrons, both orbit and spin contribute to the permanent magnetic moment; the Zeeman Hamiltonian is

$$\mathcal{H} = \mu_B(\mathbf{L} + g_S\mathbf{S}) \cdot \mathbf{B} = \mu_B g_J(\mathbf{J} \cdot \mathbf{B}) \quad (1)$$

$\mu_B$  is the Bohr magneton, and  $g_S$  is very close to 2. Diagonal terms give a first order Zeeman effect; in second order, quadratic terms produce an induced moment [12], often known as "Van Vleck paramagnetism". In an applied field with component  $B_x$ , the quadratic energy shift may be written as

$$W = - (a_x/2) (g_J \mu_B B_x)^2 \quad (2)$$

with similar terms for the y, z axes. In many compounds the effects are anisotropic, and the x, y, z axes are then the principal axes of a tensor. The parameter  $a_x$  gives the "paramagnetic shift", a sum of terms ( $2\alpha_x^2/X$ ), where  $\alpha_x$  is a matrix element of (1) between two levels separated by energy X. From (2), the

induced electronic moment is

$$m_x = -dW/dB_x = a_x (g_J \mu_B)^2 B_x \quad (3)$$

The second form in (1) applies where L, S are coupled to a resultant J by spin-orbit interaction, as in the lanthanide group, for which the theory below was derived [13]. If the nucleus has spin I, the Hamiltonian in an applied field B becomes

$$\mathcal{H} = g_J \mu_B (\mathbf{B} \cdot \mathbf{J}) + A_J (\mathbf{J} \cdot \mathbf{I}) - \gamma_N \hbar (\mathbf{B} \cdot \mathbf{I}) \quad (4)$$

here the second term is the magnetic hyperfine interaction, and the third is the true nuclear Zeeman interaction. For a free ion, a further rather complex term is required for the nuclear electric quadrupole interaction; only a simpler form is needed in the following discussion.

The quadratic energy (2) now has the form

$$W = - (a_x/2) (g_J \mu_B B_x + A_J I_x)^2 \quad (5)$$

which contains a cross-term in  $B_x I_x$  with magnitude

$$a_x (g_J \mu_B A_J) = \hbar (\gamma_x - \gamma_I). \quad (6)$$

This constitutes the enhanced nuclear Zeeman interaction;  $\gamma_x/2\pi$  is the resonant frequency in unit magnetic field along the x-axis, and there are similar

terms for the y, z axes. In the absence of cubic symmetry, anisotropy arises when the coefficients  $a_x$ ,  $a_y$ ,  $a_z$  are not all equal. Measurements of the NMR frequency may be used to derive indirect values for the Van Vleck moment, since

$$m_x/B_x = (g_J \mu_B / A_J) \hbar (\gamma_x - \gamma_I). \quad (7)$$

This has the advantage that individual contributions from inequivalent ions can be determined, whereas the bulk susceptibility gives only a net value. Quadratic effects of the magnetic hyperfine interaction give rise to a quadrupole-like term

$$P_x I_x^2 + P_y I_y^2 + P_z I_z^2, \quad (8)$$

where

$$P_x = -(a_x/2) A_J^2 = -(A_J/2 g_J \mu_B) \hbar (\gamma_x - \gamma_I). \quad (9)$$

In cubic symmetry the x, y, z components are equal, and their sum becomes a constant that may be ignored. With axial symmetry (8) reduces to

$$P_2 [I_x^2 - I(I+1)/3] \quad (10)$$

with

$$P_2 = (A_J/2 g_J \mu_B) \hbar (\gamma_{\perp} - \gamma_{\parallel}), \quad (11)$$

where the last two subscripts refer to directions perpendicular and parallel to the axis of symmetry. In addition terms

$P_1$ ,  $P_3$  arise from true quadrupole interactions [14] with field gradients of the 4f electrons on the parent ion and the remainder of the lattice respectively.

### 3. LANTHANIDE IONS

In condensed matter, a magnetic ion is subjected to an electric field set up by the surrounding ions, the "crystal field". This is represented by an electrostatic potential of complex form that depends on the crystal lattice, and its symmetry. If the symmetry is cubic, the levels may be singlets, doublets, triplets or quartets. In lower symmetry, ions with an even number of electrons may have a singlet ground state, but for other ions the levels must retain at least double degeneracy, by Kramers' theorem. In the 4f group, the  $2J \pm 1$  electronic levels of a manifold J' are split by amounts ranging up to several hundred wave numbers; at low temperatures, only a few levels have appreciable thermal population. The hyperfine parameter in eq. (4) has form

$$A_J = 2 \mu_B \gamma_N \hbar \langle r^{-3} \rangle \langle J \parallel N \parallel J \rangle \quad (12)$$

for the lanthanide group; the parameter  $\langle J \parallel N \parallel J \rangle$  is positive, and so is  $g_J$ . Thus the matrix elements that contribute to the cross term of eq. (6) are positive provided that they are within a manifold

of given  $J$ . Other terms involving the neighbouring manifolds  $J \pm 1$  are of opposite sign, but are generally much smaller because the energy denominators in perturbation theory are much larger. Typically, the energies of manifolds  $J+1$  lie at several thousand wavenumbers, while excited states of the same  $J$  may be separated only by ten to a few hundred wave numbers. Effects involving the latter are therefore generally dominant, but two exceptions are mentioned below.

For magnetic ions not at a site of cubic symmetry, the effective nuclear Zeeman interaction becomes anisotropic, and for nuclei with  $I > 1$ , there may be an appreciable nuclear quadrupolar interaction from quadratic effects of the magnetic hyperfine interaction [14]. Such effects occur also for 3d ions, but are more important for lanthanide ions, where the crystal field splittings tend to be smaller, and the hyperfine interaction larger.

In electron spin resonance (ESR) using a large magnetic field, electronic transitions are strongest in which the nuclear magnetic quantum number  $m_x$  does not change. The frequency is displaced by the hyperfine interaction, but does not directly involve the nuclear Zeeman interaction. At lower frequencies comparable with those of hyperfine interaction, transitions in which  $m_z$  changes are allowed, and the resonant frequen-

cies are then displaced by amounts proportional to the nuclear Zeeman energy, including the "enhanced nuclear Zeeman effect". However, the latter is determined more directly and much more accurately by means of ENDOR. A simple illustration is given by the detailed measurements [15] on the stable samarium isotopes of mass 147, 149 in (La, Sm)  $\text{Cl}_3$ . The crystal symmetry is hexagonal, and the trivalent samarium ion (configuration  $4f^5$ ,  $^6\text{H}$ ) has a number of levels relatively low in energy. The electronic ground state is a Kramers doublet, and the enhancement of the effective nuclear magnetic moment is anisotropic. In fact it is positive for magnetic fields normal to the symmetry axis, but negative for fields along this axis, because effects from excited states of  $J$  are then dominant. The second order contribution to the nuclear electric quadrupole interaction was also determined.

Similar terms arise also for an electronic singlet, and were first derived [16] for the trivalent europium ion,  $4f^6$ , for which the ground state is  $J = 0$ . Matrix elements to the first excited state  $J = +1$  give a negative contribution that nearly cancels the true nuclear Zeeman effect for the singlet. For other ions the enhancement is generally positive, and greatest when there are matrix elements to a low lying crystal field level; the anisotropy may be large. An enhanced

NMR signal can sometimes be followed up to temperatures at which excited levels are populated, if there is rapid relaxation between the electronic levels; the measured parameters are then thermal averages. Results for a range of insulating compounds with axial or cubic symmetry are summarised in section 5.

#### 4. MEASUREMENTS ON CONDUCTING COMPOUNDS

Following the suggestion of Al'tshuler [17] of magnetic cooling by substances with singlet electronic ground states, several investigations began on inter-metallic compounds [18] with conduction electrons, for which thermal contact should be much better than with insulators. Compounds of the ions  $^{141}\text{Pr}$  or  $^{169}\text{Tm}$  were chosen to minimize exchange interaction, assumed to vary as  $(g_J - 1)[J(J+1)]^{1/2}$ . Nevertheless, many were found [18] to order at liquid helium temperatures. In general, thulium compounds showed larger enhancement [19], but the nuclear moment is small (Table 2) and  $I=1/2$ ; for Pr, with a larger nuclear moment and  $I = 5/2$ , it is much easier to remove a large fraction of the nuclear entropy in fields of a few tesla.

Two examples are  $\text{PrCu}_5$ , which is hexagonal but shows ferromagnetism below  $\sim 50$  mK [20], and  $\text{PrTi}_3$  [21]. The latter

is cubic, and could be cooled to 1.6 mK; extrapolation suggested that ferromagnetic ordering would set in at about 1 mK. Conventional magnetic measurements were used; other early results are surveyed by Teplov [22].

Some conductors with the cubic NaCl structure [23] were investigated by NMR. In compounds without cubic symmetry, the enhancement is often highly anisotropic, and single crystals are needed. The nuclear resonant frequencies have been measured for the hexagonal compound  $\text{PrNi}_5$ . The enhancement factors at 1.2 K [24] are 6.56 and 13.13, parallel and perpendicular to the symmetry axis. The corresponding resonance frequencies are 82 and 164  $\text{MHzT}^{-1}$ , calculated from  $\gamma_I/2\pi = 12.5 \text{ MHzT}^{-1}$ . [Enhancement factors have often been quoted without specifying the unenhanced value; for praseodymium, the most recent value is 12.93  $\text{MHzT}^{-1}$ ]. In this compound the quadrupole splitting parameter  $P/h$  is not more than 0.6 MHz, considerably less than  $P_2/h \approx +4$  MHz, calculated from eq. (11). Since  $P_1/h$  is estimated to be  $-0.66$  MHz, the lattice contribution  $P_3/h$  must also be negative.

The small value of  $P/h$  is an advantage for magnetic cooling. After adiabatic demagnetisation [25] from a field of 6 T at temperatures between 10 & 29 mK, 0.2 mK was reached, though ferromagnetic order sets in at 0.40(2) mK. The

enhancement factor measured for the randomly oriented sample is 12.2(5); this corresponds to a resonance frequency of  $159 \text{ MHzT}^{-1}$ , rather higher than the mean value of  $137 \text{ MHzT}^{-1}$ , derived from the resonance values for the single crystal. The discrepancy may arise because the sample was not completely random in orientation, or from small induced moments on the nickel ions, that contribute to the bulk susceptibility but do not affect the nuclear resonance frequencies.

The classic compound for magnetic cooling was cerium magnesium nitrate,  $\text{Ce}_2\text{Mg}_3(\text{NO}_3)_{12} \cdot 24\text{H}_2\text{O}$ , for which the lowest temperature reached after demagnetisation is about 3 mK. The electronic entropy is  $R\ln 2$ , but the nuclear entropy of  $\text{PrNi}_5$  is  $R\ln 6$ ; this makes it a useful substance for magnetic cooling into the sub-millikelvin range. With it as a first stage, and metallic copper as a second stage, a temperature of 0.027 mK has been reached after adiabatic demagnetisation [26].

## 5. MEASUREMENTS ON INSULATING COMPOUNDS

The first investigations on insulating compounds began [27] at Kazan in 1967 with hydrated praseodymium sulphate, followed by other single crystals grown from aqueous solution. A wide range of

results has been reviewed recently by Aminov and Teplov [28]. The discussion below is mainly limited to measurements in Oxford on tetragonal crystals with the zircon structure, together with the elpasolites (cubic at room temperature). In most cases the presence of singlet ground states was revealed by optical Zeeman spectroscopy; the data in Table 3 were then obtained by nuclear magnetic resonance.

In many cases the resonant frequencies are highly anisotropic, particularly when large matrix elements to a low lying level exist for one direction of the magnetic field. The NMR signal can be followed up to temperatures at which some excited levels are populated if the hyperfine field is motionally averaged by rapid relaxation between the electronic levels. The measured parameters are then thermal averages; an example is  $\text{PrVO}_4$ , where the results [29] were fitted from 1 to 20 K by including parameters for the first and second excited states.

Holmium vanadate,  $\text{HoVO}_4$  has been studied in considerable detail. The crystal field splittings, measured by high-resolution optical spectroscopy [30], showed that the singlet ground state and doublet at  $21 \text{ cm}^{-1}$ , are nearly pure states:  $|J_z\rangle = |0\rangle$  and  $|\pm 1\rangle$  respectively. Application of a magnetic field confirmed that the former has almost no magnetic moment along the c-axis, but a

Compound	$\gamma_{  }/2\pi$	$\gamma_{\perp}/2\pi$	P/h
PrVO <sub>4</sub>	24.5	77.62	(+)3.35(3)
HoVO <sub>4</sub>	15(5)	1526(3)	+25.9(3)
LiTmF <sub>4</sub>	7.94(1)	245(1)	-
TmPO <sub>4</sub>	11.3	276	-
TmVO <sub>4</sub>	3450(10)*	24 & 94	
TmAsO <sub>4</sub>	706.5*	360 & 60	

Table 3. Enhanced NMR data for insulating compounds with tetragonal symmetry. Values of  $(\gamma/2\pi)$  in MHzT<sup>-1</sup>, and P/h in MHz.

The ground states of TmVO<sub>4</sub> and TmAsO<sub>4</sub> are doublets, split by Jahn-Teller distortions below 2.156 K and 6.1 K respectively. These lower the symmetry and there are domains; the constants marked \* are estimated values, extrapolated to T= 0 K.

large moment normal to it because of matrix elements between the singlet and the doublet.

The single stable isotope is <sup>165</sup>Ho, with  $I = 7/2$ , and (unenhanced) 9.0(1) MHzT<sup>-1</sup>. Novel circuits for NMR experiments at 500 MHz were used [14] to determine the principal resonance parameters (see Table 3); values for a crystal of YVO<sub>4</sub> containing 2% Ho are almost identical. At 1.3 K the anisotropy in the induced magnetic moment is over 200:1, but is considerably less at 20 K. The contributions to the nuclear electric quadrupole interaction are estimated to be  $P_1/h = -35(2)$  MHz,  $P_2/h = +35.3$  MHz; since these almost cancel, the measured value  $P/h = (+)25.6(3)$  MHz implies a lattice

contribution  $P_3/h \approx +25$  MHz. The NMR signals are strong, because the enhancement applies also to the r.f. field, provided this is in the (001) plane, and normal to the steady field. Essentially the r.f. field causes the induced moment to oscillate in direction, producing a greatly enhanced r.f. field at the nucleus through the hyperfine interaction. A further study [31] has provided more detail and a better fit between optical spectroscopy and NMR results.

TmPO<sub>4</sub> [32] also shows considerable anisotropy (see Table 3). Changes above 4 K were fitted to crystal field levels determined by optical and Raman spectroscopy. The anisotropic paramagnetic shifts in the NMR spectrum of <sup>31</sup>P ( $I =$

1/2) were found to be proportional to the electronic susceptibilities.

For  $\text{TmVO}_4$  and  $\text{TmAsO}_4$  the tetragonal field leaves non-Kramers doublets as ground states, but these are split by Jahn-Teller distortions at temperatures below 2.156(5) K [33] and 6.13(3) K respectively [34]. At lower temperatures the enhanced NMR frequency is unusually large along the c-axis, particularly so for the former, since the doublet splitting is rather small, with a maximum value of  $2.97(4) \text{ cm}^{-1}$  for  $T = 0 \text{ K}$  [35]. Zeeman effects in some excited electronic states have been observed in fields up to 7 T [36].

Elpasolite compounds with the formula  $\text{Cs}_2\text{NaLnCl}_6$  are cubic at room temperature, but many undergo structural transitions at lower temperatures. Three compounds with the non-Kramers trivalent ions  $\text{Ln} = \text{Pr}, \text{Tb}$  and  $\text{Tm}$  have singlet states; for these, investigations by enhanced NMR [37] have revealed small tetragonal distortions, but  $\text{Cs}_2\text{NaHoCl}_6$  was shown to remain cubic [38]. It differs in that the ground state of the trivalent holmium ion is a non-Kramers doublet, split in second order by the Zeeman effect; this produces a temperature-dependent anisotropy consistent with the cubic symmetry. Below 4 K it was studied by enhanced NMR of the  $^{165}\text{Ho}$  ions, together with the NMR paramagnetic shifts of the diamagnetic Na and Cs

ions. Electron spin resonance of the impurity ions  $\text{Gd}^{3+}$ ,  $\text{Dy}^{3+}$ ,  $\text{Er}^{3+}$  and  $\text{Yb}^{3+}$ , and of the holmium ion [39] has also been observed. The latter was shown to be consistent with theory [40]; an improved theory of the nuclear interactions was given later [41].

## 6- ENHANCED ACOUSTIC RESONANCE

Longitudinal acoustic waves were used for enhanced nuclear resonance in a single crystal of  $\text{PrF}_3$  [42] at 20-40 MHz; much higher frequencies (0.8 GHz) were used later for  $\text{HoVO}_4$  [43]. The acoustic strains produce an effect in third order, involving both the applied magnetic field and the hyperfine interaction. Essentially the fluctuating acoustic strain modulates the direction of the electronic moment induced by the applied field; at the nucleus, through the magnetic hyperfine interaction, this produces an oscillating magnetic field, giving rise to resonance transitions within the nuclear spin system. Matrix elements from electric quadrupole interactions also cause transitions, but the intensity is smaller at a given frequency [44].

For  $\text{HoVO}_4$ , measurements were made with a magnetic field in the (001) plane; acoustic waves, propagated in this plane, were generated by a transducer of

zinc oxide, grown directly onto a single crystal by sputtered epitaxial deposition. Pulses of order 100 ns duration were applied, the transducer being switched alternately from transmit to receive. Signals are observed from two sets of transitions in which the nuclear magnetic quantum number changes either by  $\pm 1$ , or by  $\pm 2$ ; the former are much stronger, and have maxima and minima at different orientations of the magnetic field. Also, the intensities are larger by a factor 100 for acoustic waves propagated along a [100] axis than for similar waves along a [110] axis. The non-resonant magneto-acoustic absorption has also been studied and analysed [45].

As in magnetic resonance with electromagnetic waves, the signal intensity is proportional to the energy quantum and the difference in population of the two levels involved; it has contributions involving both second and fourth powers of the frequency. The process of absorption of energy from an acoustic wave is identical with the "direct process" by which thermal phonons induce transitions in the spin system, maintaining it in thermal equilibrium with the lattice. Rates calculated from the acoustic absorption measurements are in marked contrast to the overall relaxation rate, determined by observing recovery of the signal after saturation [46]. Between 0.08 and 1.33 K, the latter is faster by a factor  $10^{13}$  to  $10^{15}$  at a

field of 5 millitesla. Though transverse waves may give faster rates of relaxation, this enormous discrepancy must be ascribed primarily to paramagnetic impurities. The mechanism has been identified by novel experiments [47] on the enhanced holmium spin system in holmium vanadate, magnetized at a temperature of 50 mK in a field of 2 T, and then demagnetized to about 5 mK in a field of 50 mT. The results suggest that energy is transferred by spin-spin interaction to impurity ions with electronic moments. For example, the electronic resonance frequency of dysprosium would be 7 GHz, with a width 1.5 GHz resulting from interactions with the enhanced holmium moments. These impurity spins "talk" to a wide band of phonons that transmit energy rapidly to the dilute liquid Helium 3 bath at 100 mK, the last barrier being the Kapitza resistance at the surface. Such a mechanism may well account for the much faster relaxation rates observed directly.

## 7- THE ORDERED STATE

Most electronic paramagnetic compounds enter an ordered state at milliKelvin or much higher temperatures; nuclear moments order only at much lower temperatures (58 nanoKelvin in copper metal). Obviously, enhanced

nuclear magnets form an intermediate group. Holmium vanadate enters an antiferromagnetic state at about 4.5 mK, close to the predicted value [48]; this has been studied by nuclear orientation [49], [50] of radioactive isotope  $^{166\text{m}}\text{Ho}$  ( $I = 7$ ), as well as by nuclear quadrupole resonance of  $^{51}\text{V}$  [51]. A neutron diffraction study [52] has also produced a structure consistent with the proposed model.

In  $\text{TmVO}_4$ , enhanced nuclear cooling produced no signs of ordering [53] at suggested temperature [33] of 0.2 mK.

For  $\text{TmPO}_4$  a different approach was used - first dynamical nuclear polarisation (60%) of the enhanced thulium moments by "pumping" on an impurity ion,  $\text{Yb}^{3+}$ , followed by "adiabatic demagnetisation in the rotating frame" [54], [55]. The existence of the ordered state was monitored through the NMR signal of the nucleus  $^{31}\text{P}$ .

The elpasolite  $\text{Cs}_2\text{NaHoCl}_6$  is of particular interest because its electronic ground state is a non-Kramers doublet (see above). It orders at 4.8 mK, and measurements of magnetic susceptibility and heat capacity have been made [56], [57]. In a neutron diffraction study [58], no antiferromagnetic diffraction peaks were observed, but enhanced antiferromagnetic resonance has been detected [59]. A theoretical study of electronic and nuclear order suggests that a transition at about 600 mK [61] arises

from electronic quadrupole-quadrupole interactions.

## REFERENCES

- [1] Stern, O., *Zeits.f. Physik Z.*, 418 (1921).
- [2] Gerlach, W. and Stern, O., *Ann.Physik*, **74**, 673 (1924); *Ann.Physik*, **76**, 163 (1925).
- [3] Rabi, I. I., Millman, S., Kusch, P. and Zacharias, J. R., *Phys.Rev.*, **55**, 526, (1939).
- [4] Ramsey, N. F., "Molecular Beams", Clarendon Press, Oxford (1956).
- [5] Essen, L., *Vistas Astron.*, **2**, 45 (1969).
- [6] Zavoisk, E., *Fiz. Zh.* **9**, 211 (1945).
- [7] Purcell, E. M., Torrey, H. C. and Pound, R.V., *Phys. Rev.* **70**, 474 (1946).
- [8] Bloch, F., Hansen, W. W., and Packard, M., *Phys. Rev.* **70**, 474 (1946).
- [9] Gorter, C. J., *Paramagnetic Relaxation* (Elsevier), 126 (1947).
- [10] Rollin, B. V., *Nature* **158**, 669 (1946).
- [11] Rollin, B. V. and Hatton, J., *Nature* **159**, 201 (1947).
- [12] Van Vleck, J. H., *Phys. Rev.*, **31**, 587 (1928).
- [13] Baker, J. M. and Bleaney, B., *Proc. R. Soc. Lond.* **A245**, 156 (1958).
- [14] Bleaney, B., Robinson, F. N. H., and Wells, M. R., *Proc. R. Soc.Lond.* **A362**, 170 (1978).
- [15] Chan, I. Y. and Hutchison, C.A. Jr., *Phys.*

- Rev. **B5**, 3387 (1972).
- [16] Elliott, R. J., Proc. Phys. Soc. **B70**, 119 (1957).
- [17] Al'tshuler, S. A., JETP lett. **3**, 112 (1966).
- [18] Andres, K., Cryogenics 473-478 (1978).
- [19] Andres, K. and Bucher, E., J. App. Phys. **42**, 1522 (1971).
- [20] Andres, K., Bucher, E., Schmidt, P. H., Maita, J. P. and Darack, S., Phys. Rev. **B11**, 4364 (1975).
- [21] Andres, K. and Darack, S., Phys. Rev. **B10**, 1967 (1974).
- [22] Teplov, M. A., in Crystal Field Effects in Metals and Alloys, (ed. A. Furrer, Plenum Press, N. Y.), 318 (1977).
- [23] Jones, E. D., Phys. Rev. Lett. **19**, 432 (1967); Phys. Rev. **180**, 455, (1969).
- [24] Kaplan, N., Williams, D. LL. and Grayevsky, A., Phys. Rev. **821**, 899 (1980).
- [25] Kubota, M., Folle, H. R., Buchal, Ch., Mueller, R. M. and Pobell, F. Phys. Rev. Lett. **45**, 1812 (1980).
- [26] Ishimoto, H. N., Nishida, T., Furubayashi, M., Shinohara, Y., Takano, Y., Miura, Y. and Ono, K., J. Low Temp. Phys. **55**, 17 (1984).
- [27] Al'tshuler, S. A., and Teplov, M. A., JETP Lett. **5**, 167 (1967).
- [28] Aminov, L. K. and Teplov, M. A., Sov. Sci. Rev. A Phys., **14**, 1(1990).
- [29] Bleaney, B., Harley, R. T., Ryan, J. F., Wells, M. R. and Wiltshire, M. C. K., J. Phys.C. **11**, 3059 (1978).
- [30] Battison, J. E., Kasten, A., Leask, M.J. M. and Lowry, J. B., Phys. Lett. **55A**, 173 (1975).
- [31] Bleaney, B., Gregg, J. F., Hansen, P., Huan, C.H.A., Lazzouni, M., Leask, M. J. M., Morris, I. and Wells, M. R., Proc. R. Soc. Lond. **A416**, 63 (1980).
- [32] Bleaney, B., Pasman, J. H. T. and Wells, M. R., Proc. R. Soc. Lond. **A387**, 75-90 (1983).
- [33] Bleaney, B. and Wells, M. R., Proc. R. Soc. Lond., **A370**, 131-153 (1980).
- [34] Bleaney, B., Gregg, J. F., Leask, M. J. M. and Wells, M. R., Proc. R. Soc. Lond. **A394**, 69-85 (1984).
- [35] Becker, P. J., Leask, M. J. M. and Tyte, R. N., J. Phys. C. **5**, 2027-2036 (1972)
- [36] de Wolf, I., Janssen, P. amd Bleaney, B., Phys. Lett. **108A**, 221 (1985).
- [37] Bleaney, B., Stephen, A. G., Walker, P. J. and Wells, M. R., Proc. R. Soc. Lond. **A381**, 1 (1982).
- [38] Bleaney, B., Stephen, A. G., Walker, P. J. and Wells, M. R., Proc. R. Soc. Lond. **A376**, 235 (1982).
- [39] Bleaney, B., Stephen, A. G., Sung Ho Choh and Wells, M. R., Proc. R. Soc. Lond. **A376**, 253 (1982).
- [40] Bleaney, B., Proc. R. Soc. Lond. **A376**, 217 (1982).
- [41] Abragam, A. and Bleaney, B., Proc. R. Soc. Lond. **A382**, 61 (1982).

- [42] Al'Tshuler, S. A., Duglav, A. Kh., Kasanov, I. G. and Teplov, M.A., JETP Lett. **29**, 625 (1979).
- [43] Bleaney, B., Briggs, G. A. D., Gregg, J. F., Huan, C. H. A., Morris, I. D. and Wells, M. R. Proc. R. Soc. Lond. **A416**, 93 (1988).
- [44] Bleaney, B. and Gregg, J. F., Proc. R. Soc. Lond. **A413**, 313 (1987).
- [45] Bleaney, B., Gregg, J. F., Huan, C. H. A., Morris, I. D. and Wells, M. R., Proc. R. Soc. Lond. **A416**, 75 and 83 (1988).
- [46] Suzuki, H., (private communication) (1986).
- [47] Jacquinet, J-F., Gregg, J. F. Roinel, Y., Fermon, C. and Bouffard, V., J. Low Temp. Phys. **64**, 115 (1986).
- [48] Bleaney, B., Proc. R. Soc. Lond., **A370**, 313 (1980).
- [49] Allsop, A. L., Bleaney, B., Bowden, G. J., Nambudripad, N., Stone, N. J. and Suzuki, H. Proc. R. Soc. Lond., **A372**, 19 (1980).
- [50] Clark, R. G., Allsop, A. L., Stone, N. J. and Bowden, G. J., J. Phys. C. **20**, 797 (1987).
- [51] Bleaney, B., Clark, R. G., Gregg, J. F. Roinel, Y., and Stone, N. J., J. Phys. C **20**, 3175 (1987).
- [52] Suzuki, H., Ohtsuka, T., Kawarazaki, S., Kunitoni, N., Moon, R. M. and Nicklow, R. M., Solid State Comm. **49**, 1157 (1984).
- [53] Suzuki, H., Inoue, T., Higashino, Y. and Ohtsuka, T., Physics Letters **77A**, 185 (1980).
- [54] Abragam, A., Bouffard, V., Fermon, C., Fournier, G., Gregg, J. F., Jacquinet, J-F. and Roinel, Y., Comptes Rendus, **99**, 509 (1984).
- [55] Fermon, C., Gregg, J. F., Jaquinot, J-F., Roinel, Y., Bouffard, V., Fournier, G. & Abragam, A., J. Phys. (Paris), **47**, 1053 (1986).
- [56] Suzuki, H., Miyamoto, M., Masuda, Y. and Ohtsuka, T., J. Low. Temp. Phys., **48**, 297 (1982).
- [57] Suzuki, H., Masuda, Y, Miyamoto, M., Dakatsume, S., Walker, P. J. and Ohtsuka, T., J. Mag. Magn. Mat., **31**, 741 (1983).
- [58] Masuda, Y., Suzuki, H., Ohtsuka, T. and Tamaki, A., Jap. J. Applied Physics, **26**, Supplement 26-3, 433 (1987).
- [59] Suzuki, H., Masuda, Y. and Arthur, J., Jap. J. Appl. Phys, **26**, Supplement 26-3, 437 (1987).
- [60] Bowden, G. J., Elliott, R. J. and Oitmaa, J., Proc. R. Soc. Lond., **A399**, 73 (1985).
- [61] Bongers, E., Brom, H. B., Veenendal, E. J., Huiskamp, W. J. and Amberger, H. D., Physica **115B**, 72 (1983).

# THE PROBLEM OF SPURIOUS COLOR BOUND STATES IN NAMBU JONA-LASINIO TYPE LAGRANGIANS \*

ALEX H. BLIN, BRIGITTE HILLER AND JOÃO DA PROVIDÊNCIA

Centro de Física Teórica (INIC). Universidade de Coimbra P-3000 Coimbra. Portugal

[Received January 1992]

**ABSTRACT** - Quark-antiquark states in a chiral invariant four fermion interaction lagrangian without confinement are investigated. We issue a warning regarding the possible existence of color bound states in this type of lagrangians frequently used in low energy hadron physics. Simply ignoring the color terms as a consequence of confinement is not sufficient, since the appearance of bound color states indicates that the physics of confinement has also an effect at low energies.

## 1. INTRODUCTION

The original Nambu Jona-Lasinio (NJL) model [1] has been mainly designed as a mechanism to create Goldstone bosons via dynamical chiral symmetry breaking in a four fermion interaction. Many authors have used NJL-type lagrangians to describe other mesonic states as well, see e.g. [2-5], although no confinement is included. One usually argues that as long as the two quarks are bound, that is for energies below the mass of two quarks, confinement should not significantly change the results. Also, since the lagrangian does not contain

confinement, one simply and arbitrarily disregards the color sector which, if not already existent in the direct terms, appears after fierzing. But how reliable is a model whose langrangian gives rise to color terms in which, for instance, a bound color state appears? We should not expect that confinement only suppresses this state without changing as well the physical meson masses. Just disregarding color terms is certainly not the way to mimic confinement. To see whether the color sector can have the alarming behavior of allowing for bound color mesons or significant strength in the quark-antiquark ( $q\bar{q}$ ) continuum, we

---

\* Partially supported by CRUP and JNICT (nº PMCT/C/CEN/72/90).

study, as an example, a simple quartic NJL-type model corresponding to the quark sector of the 't Hooft lagrangian [6, 7], which has been used by several authors [2, 4, 8].

It is not our intention to calculate a complete meson spectrum from an NJL-lagrangian, nor to elaborate on more complicated non-local interactions, but to concentrate upon the significance of the color sector in a specific case which serves as an example. We anticipate our findings by saying that there are indeed color bound states and strength in the  $q\bar{q}$ -continuum in this special model. There is no reason to believe that other types of lagrangians without confinement will be free of this type of problems.

In section 2 we present the general properties of the model and calculate the bound and continuum states of the color singlet in sect. 3 and of the color octet in

sect. 4. Sect. 5 summarizes the conclusions, and calculational details are discussed in the appendix.

## 2- GENERAL PROPERTIES OF THE MODEL

The interaction between two quarks in this model is [6, 7]

$$v_{12} = g_{\text{eff}} [I + \gamma_5(1)\gamma_5(2)] [I - \tau(1)\tau(2)] [a + b\Lambda(1)\Lambda(2)] \quad (1)$$

with  $\tau$  the isospin vector,  $\Lambda$  the Gell-Mann SU(3) color vector and  $I$  unit matrices. The coefficients are  $a=2$  and  $b=-3/8$ . With this interaction, the Fierz transformed lagrangian becomes (suppressing indices 1 and 2)

$$\begin{aligned} \mathcal{L}(x) = & \bar{\Psi}(x)(i\partial - m_c)\Psi(x) + 2g_{\text{eff}} \left[ [\bar{\Psi}(x)\Psi(x)]^2 + [\bar{\Psi}(x)i\gamma_5\tau\Psi(x)]^2 + [\bar{\Psi}(x)i\tau\Psi(x)]^2 + [\bar{\Psi}(x)\gamma_5\Psi(x)]^2 \right] + \\ & \frac{3}{16} g_{\text{eff}} \left[ [\bar{\Psi}(x)\Lambda\Psi(x)]^2 + [\bar{\Psi}(x)i\gamma_5\tau\Lambda\Psi(x)]^2 + [\bar{\Psi}(x)i\tau\Lambda\Psi(x)]^2 + [\bar{\Psi}(x)\gamma_5\Lambda\Psi(x)]^2 \right] + \\ & \frac{9}{32} g_{\text{eff}} \left[ [\bar{\Psi}(x)i\tau\sigma_{\mu\nu}\Psi(x)]^2 + [\bar{\Psi}(x)\sigma_{\mu\nu}\Lambda\Psi(x)]^2 \right] \end{aligned} \quad (2)$$

where  $\Psi$  and  $\bar{\Psi}$  are the quark and anti-quark fields, and the effective coupling  $g_{\text{eff}}$  is constant. Although the point interaction is an approximation to the lagrangian derived by 't Hooft, we think that the structure of the forces, which we

keep, is more important than their range. We take the current quark mass  $m_c=0$ . Calculations are done to one-loop order, i.e. to Hartree-Fock approximation. The lagrangian contains explicitly color-octet terms.

As in the case of the NJL model [1], the quartic interaction lagrangian is non-renormalizable and we take a covariant cutoff  $L$  for the loop momenta in one-loop approximation. As usual, the quark self-energy leads in Hartree-Fock approximation to the self-consistency equation

$$1 = 12 g_0 \int_0^{\lambda^2} \frac{dy y}{4\pi^2 y+1} = \frac{12}{4\pi^2} g_0 [\lambda^2 - \ln(1+\lambda^2)] \quad (3)$$

with the dimensionless quantities  $g_0 = g_{\text{eff}} \cdot m^2$  and  $\lambda^2 = L/m^2$  where the factor 12 arises from taking traces over spin, isospin and color matrices and from the coupling. In addition to the self consistency equation, the cutoff and the quark mass are related through the expression for the weak decay constant  $f_\pi = 93$  MeV of the pion, calculated the same way as in the NJL model [9-11]

$$f_\pi^2 = \frac{3m^2}{4\pi^2} \left[ \ln(1+\lambda^2) - \frac{\lambda^2}{1+\lambda^2} \right] \quad (4)$$

### 3- COLOR SINGLET STATES

We proceed to determine the poles of the propagators corresponding to the different couplings from the Bethe-Salpeter equation to one-loop order. The meson propagators have the structure

$$G_i = [1 - J_i(\rho^2)]^{-1} \quad (5)$$

(omitting couplings and with  $\rho^2 = k^2/4m^2$ ,  $k^2 =$  square of invariant meson mass), where  $J_i(\rho^2)$  is the fundamental  $q\bar{q}$ -loop for the  $i$ -th type of meson and 1 stands for the self consistency eq. (3). In analogy to the NJL model, the pion emerges as a Goldstone mode in the course of dynamical breaking of chiral symmetry, and the scalar-isoscalar meson appears as a  $q\bar{q}$  bound state with mass  $2m$ , at the threshold of the  $q\bar{q}$ -continuum, with the  $q\bar{q}$ -loops  $J_\pi$  and  $J_\sigma$  given in the appendix.

The residue at the pole of  $G_\pi$  is the square of the strength (henceforth always denoted as strength) of the  $\pi$ - $q\bar{q}$  coupling and is given by  $m^2/f_\pi^2$ . In the case of the scalar-isoscalar mode, the  $\sigma$ - $q\bar{q}$  strength is calculated in [12] and reduces to  $m^2/f_\pi^2$  for large  $\lambda^2$ . In the  $q\bar{q}$ -continuum  $\rho^2 > 1$  the strengths  $S_i$  of the pseudoscalar-isovector and scalar-isoscalar modes are related to the cut of  $J_i$  along the imaginary axis.

The pseudo scalar-isoscalar mode is not a bound state (see appendix). A numerical test shows that the scalar-isovector mode has no pole for cutoffs  $\lambda^2 > 0.1$ . As in the NJL-model, only two bound states appear, the pion and the scalar-isoscalar, for any value of the cutoff. For  $\lambda^2 = 3.7$  (corresponding to  $m = 386$  MeV), a value taken in previous works [11,12], all other mesons have

their strength distributed in the  $q\bar{q}$ -continuum [12]. The corresponding strengths are given in the appendix.

#### 4-COLOR OCTET STATES

We turn now to the discussion of the color octet. The  $\sigma_{\mu\nu}$  terms lead to vector modes in the Bethe-Salpeter equation to one-loop order. Similarly to [11], the vector-isoscalar mode has never a pole, also in the color sector. However, the vector-isovector mode shows poles whenever the cutoff  $\lambda^2 < 1.5$ , corresponding to quark masses  $m > 600$  MeV. Another pole appears for the pseudoscalar-isovector octet for  $\lambda^2 < 0.2$

or  $m > 2700$  MeV. The other octet modes have no poles. We observe that the disturbing poles appear here at constituent quark masses larger than the commonly used value  $m \approx 300 \dots 400$  MeV.

We find that there is some strength in the  $q\bar{q}$ -continuum (see expression in the appendix). We checked numerically that the strength of the scalar octet states is smaller than that of the corresponding singlet states (see table 1). We note that the 't Hooft lagrangian favors the color singlet states to a certain degree, except for the vector-isovector mode, which does not exist in the color singlet. To suppress the color octet states completely, one would of course need to include confinement.

Mode	Singlet	Octet	Ratio Singlet/Octet
Scalar-isoscalar	9.97	1.01	9.91
Pseudoscalar-isovector	10.20	1.34	7.61
Scalar-isovector	0.88	0.19	4.63
Pseudoscalar-isoscalar	0.67	0.22	3.12
Vector-isovector	0.	finite	$\infty$

The integrated strengths in the singlet and octet modes (including residues of poles in the singlet) and their ratios, calculated using the cutoff  $\lambda^2 = 3.7$ .

#### 5- CONCLUSIONS

Our intention was to exhibit the shortcomings of NJL-type models without

confinement used in low-energy hadron physics. We do not adhere to the common opinion that simply ignoring the color terms in the lagrangian is sufficient

as a consequence of confinement in the low-energy range, since the appearance of color bound states indicates that confinement should also act down to energies below twice the quark mass, the threshold of the  $q\bar{q}$ -continuum. Therefore, one should expect that physical (uncolored) bound states are also affected by confinement. In the special example considered, color bound states appear only for constituent quark masses larger than the frequently used values of  $m = 300...400$  MeV, and the strengths of color mesons are somehow suppressed as compared to the color singlet mesons with the same quantum numbers. However, there is no guarantee that in other NJL-lagrangians color bound states could not appear for the usual quark masses. Also, the quark mass values of  $m \approx 600$  MeV at which a bound color vector mode starts to appear in this study is dangerously close to the usually accepted value. The suppression of color meson strengths is not very strong and could also get worse in other models. This, however, might be acceptable since confinement really does act in the  $q\bar{q}$ -continuum.

## 6- APPENDIX

In the color singlet, the  $q\bar{q}$ -loop expressions for the pseudo scalar-isovector ( $\pi$ ) and scalar-isoscalar ( $\sigma$ ) modes are:

$$J_{\pi}(\rho^2) = \frac{12 g_{\Omega}}{4\pi^2} \int_0^{\lambda^2} dy y \int_0^1 dx \frac{[y + \rho^2(1-x^2)+1]}{[y + \rho^2(x^2-1)+1]^2} \quad (A1)$$

$$J_{\sigma}(\rho^2) = \frac{12 g_{\Omega}}{4\pi^2} \int_0^{\lambda^2} dy y \int_0^1 dx \frac{[y + \rho^2(1-x^2) - 1]}{[y + \rho^2(x^2-1)+1]^2} \quad (A2)$$

The integrals in (A1) and (A2) are explicitly evaluated in ref. [12]. The corresponding strengths in the  $q\bar{q}$ -continuum are given by

$$S_i(\rho^2) = 2g_{\text{eff}} \text{Im}[(1-J_i(\rho^2))^{-1}], \quad i = \pi, \sigma \quad (A3)$$

The pseudoscalar-isoscalar mode is not a bound state, since the corresponding  $q\bar{q}$ -loop has the opposite sign of  $J_{\pi}(\rho^2)$  and is therefore always negative, implying that there is no pole in the propagator, see eq. (5). The respective strength in the continuum has the form

$$S_{\eta}(\rho^2) = 2g_{\text{eff}} \text{Im}[(1-J_{\pi}(\rho^2))^{-1}] \quad (A4)$$

The scalar-isovector mode has a  $q\bar{q}$ -loop equal to the negative of the scalar-isoscalar loop  $J_{\sigma}(\rho^2)$ . Its strength in the continuum is calculated as

$$S_{\delta}(\rho^2) = 2g_{\text{eff}} \text{Im}[(1+J_{\sigma}(\rho^2))^{-1}] \quad (A5)$$

In the color octet, the pseudoscalar-isoscalar octet mode is not a bound state,

since the corresponding expression for the  $q\bar{q}$ -loop  $J_{\eta\Lambda}$  is proportional to the negative of  $J_\pi$ . The  $q\bar{q}$ -loop of the scalar-isoscalar mode is  $J_{\eta\Lambda} = J_6/16$ ;  $J_6$  in turn has its pole at  $\rho^2=1$  the maximum allowed value. Hence to find a pole,  $\rho^2$  would have to be greater than one, since  $J_\sigma$  is monotonically increasing with  $\rho^2$ . We determined numerically the non-existence of bound states for the scalar-isovector mode of the color octet with  $q\bar{q}$ -loop  $J_{\delta\Lambda}$ . The pseudoscalar-isovector octet with  $q\bar{q}$ -loop  $J_{\pi\Lambda}$  has also no pole for  $\lambda^2 > 0.2$ , which corresponds to quark masses smaller than 2700 MeV, according to eq. (4).

The expressions for the strengths in the color octet related to the scalar-isoscalar ( $\sigma\Lambda$ ), pseudoscalar-isovector ( $\pi\Lambda$ ), scalar-isovector ( $\delta\Lambda$ ) and pseudoscalar-isoscalar ( $\eta\Lambda$ ) modes are given by

$$\begin{aligned} S_{\sigma\Lambda}(\rho^2) &= \frac{3}{16} g_{\text{eff}} \text{Im}[(1 - \frac{1}{16} J_\sigma(\rho^2))^{-1}] \\ S_{\pi\Lambda}(\rho^2) &= \frac{3}{16} g_{\text{eff}} \text{Im}[(1 - \frac{1}{16} J_\pi(\rho^2))^{-1}] \\ S_{\delta\Lambda}(\rho^2) &= \frac{3}{16} g_{\text{eff}} \text{Im}[(1 + \frac{1}{16} J_\sigma(\rho^2))^{-1}] \\ S_{\eta\Lambda}(\rho^2) &= \frac{3}{16} g_{\text{eff}} \text{Im}[(1 + \frac{1}{16} J_\pi(\rho^2))^{-1}] \end{aligned} \quad (\text{A6})$$

#### ACKNOWLEDGMENTS

The authors are grateful to M. Schaden for fruitful discussions. This work was

supported by the Instituto Nacional de Investigação Científica, Portugal.

#### REFERENCES

- [1] Nambu, Y. and Jona-Lasino G., Phys. Rev. **122**, 345 (1961) and Phys. Rev. **124**, 246 (1961).
- [2] Bernard, V. and Meissner, U.G., Phys. Rev. **D38**, 1551 (1988); Bernard, V., Jaffe, R. L. and Meissner, U. G., Nucl. Phys. **B308**, 753 (1988) and Phys. Lett. **B198**, 92 (1987).
- [3] Bernard, V., and Meissner, U. G., Nucl. Phys. **A489**, 647 (1988).
- [4] Volkov, M. K., Ann. Phys. **157**, 282 (1984); Ebert, D. and Reinhardt, H., Nucl. Phys. **B271**, 188 (1986).
- [5] Klimt, S., Lutz, M., Vogl, U. and Weise, W., preprint Universität Regensburg **TPR-89-26** (1989).
- [6] 't Hooft, G., Phys. Rev. **D14**, 3432 (1976).
- [7] Shifman, M. A., Vainshtein, A. I. and Zakharov, V. I., Nucl. Phys. **B163**, 46 (1980).
- [8] Alkofer, R. and Reinhardt, H., Z. Phys. **C45**, 275 (1989); Alkofer, R. and Zahed, I., Phys. Lett. **B238**, 149 (1990) and Mod. Phys. Lett. **A18**, 1737 (1989).
- [9] Hatsuda, T. and Kunihiro, T., Phys. Lett. **145B**, 7 (1984) and Progr. Theor. Phys. **71**, 1332 (1984).
- [10] Bernard, V., Phys. Rev. **D34**, 1601 (1986).
- [11] Blin, A. H., Hiller, B. and Schaden, M., Z. Phys. **A331**, 75 (1988).
- [12] Blin, A. H., Hiller, B. and da Providência, J., Phys. Lett. **B241**, 1 (1990).

# STRUCTURE AND PHYSICAL PROPERTIES OF THE QUATERNARY PHASE "CAALSIFER" IN INDUSTRIAL Fe-Si ALLOYS

F. MARGARIDO<sup>1</sup>, M. O. FIGUEIREDO<sup>2</sup>

1-Dep. Eng. Materiais, IST and Centro de Valorização de Recursos Minerais, INIC, Av. Rovisco Pais, 1096 Lisboa Codex.

2-Centro de Cristalografia e Mineralogia, Instituto de Investigação Científica Tropical,

Al. D. Afonso Henriques, 41, 4 E, 1000 Lisboa, Portugal.

[Received March 1992]

**ABSTRACT** -From the structural study of Fe-Si alloys with 75 wt.% Si it was possible to detect, beyond the well recognized phases - Si, FeSi<sub>2</sub> ( $\alpha$  and  $\beta$ ), Ca-Si, Fe-Si-Al, Ca-Al-Si - a quaternary phase Fe-Al-Si-Ca isotypic with  $\alpha$ -Fe<sub>1-x</sub>Si<sub>2</sub> (leboite) which we designate as "Caalsifer" from the chemical constitution.

By comparing the X-ray intensities diffracted by " $\alpha$ -Fe<sub>1-x</sub>Si<sub>2</sub>" phases with the corresponding values calculated on the basis of various chemical-structural models, the composition (Fe<sub>0.8</sub>Al<sub>0.1</sub>□<sub>0.1</sub>)(Si<sub>0.8</sub>Ca<sub>0.2</sub>)<sub>2</sub> was assigned to that phase.

A mechanism for the structural transition  $\alpha \rightarrow \beta$  "FeSi<sub>2</sub>" is suggested based on crystalchemical data of these phases. We suggest an explanation for the hindering of such structural transformation in these alloys and for the properties of the quaternary phase Caalsifer.

## 1 - INTRODUCTION

Studies on the metallurgical structures of iron alloys, namely of ferro-silicon alloys, are not frequently available, a fact that may be due to the assumption that these alloys are produced to be remelted and, therefore, their physical metallurgy is of minor importance [1]. However, the phase composition of ferro-silicon alloys may significantly affect some

properties, beyond playing an important role in the leaching treatment for silicon extraction.

Fe-Si alloys contain, besides iron and silicon, minor elements, like Al, Ca, Ti, Cr, V, Mn. The fundamental chemical components, likely to give rise to changes in the constitution of the main phases are Fe, Si, Ca and Al. The other elements found in minute percentages are dispersed in the dominant phases.

Structurally, these alloys are essentially a composite formed by silicon metal, iron disilicide (an intermetallic phase with nominal composition  $\text{FeSi}_2$ ) and some "spurious" phases (Ca-Si, Fe-Si-Al, Ca-Al-Si) which contain other impurities [2].

Gibbs phase's rule ( $P+F=C+2$ ) does not hold, since alloy solidification takes place outside the equilibrium conditions. The number of observed phases is then higher than expected for an essentially quaternary system (Si, Fe, Al, Ca). The presence of trace elements and the large span of percentages of main elements (Fe+Si versus Al+Ca) give sporadically rise to the appearance and local concentration of phases with minute dimensions.

The growing demand of high grade silicon metal together with the high level of energy-consumption associated to the electrometallurgical process of refining, have led to the development of an alternative hydrometallurgical treatment for ferro-silicon alloys with 75 wt. % Si.

The leaching efficiency depends critically on the access of the leaching agent to those intermetallic phases. The corrosive attack by this acid solute must give rise to an early disintegration of the alloy and dissolve the impurities (Fe, Ca and Al) to the desired level, leaving the less contaminated and chemically stable silicon grains unaltered [3]. Conse-

quently, the ferro-silicon microstructure, its fracture, intra and inter-phase residual stresses will be important factors to take into account when the hydrometallurgical process is optimized.

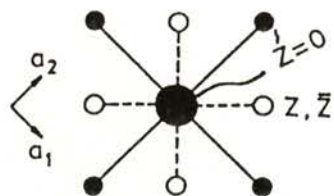
## 2 - CRYSTALCHEMISTRY AND PHYSICAL PROPERTIES OF " $\text{FeSi}_2$ " PHASES

In the silicon rich region of Fe-Si phase diagram, two structural forms of the intermetallic compound " $\text{FeSi}_2$ " exist beyond silicon: the  $\alpha$  phase, usually called "leboite", stable at high temperature, and the low temperature  $\beta$  phase.

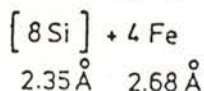
The high temperature  $\alpha$  phase, exhibits a non-stoichiometric composition " $\text{Fe}_{1-x}\text{Si}_2$ " and has a tetragonal crystal symmetry with parameters  $a = 2.68 \text{ \AA}$  and  $c = 5.134 \text{ \AA}$ , space group  $P4/mmm$ , with iron in the equivalent position 1(a) (0,0,0), silicon in  $2(h) \pm (\frac{1}{2}, \frac{1}{2}, z)$  and a positional parameter  $z = 0.27$  [4].

The Si-Si interatomic distance is  $2.36 \text{ \AA}$  along the quaternary axis. Parallel to (001) there are quadrangular layers of Fe atoms with interatomic distances Fe-Fe =  $2.68 \text{ \AA}$ , similar to those found in the metal [5,6]. Fe atoms are almost cubically surrounded by eight Si atoms at a distance of  $2.35 \text{ \AA}$ , and by four Fe atoms in the (001) plane at  $z = 0$  and at a distance of  $2.68 \text{ \AA}$ . However, the actual situation is more complex because the Fe sublattice contains 13-23% vacancies,

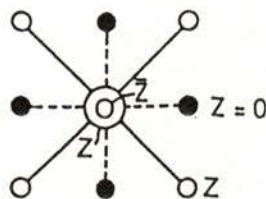
which means that there is no real equivalency of all the Fe atoms in the compound [7]. The nearest neighbours of silicon are four Fe atoms at a distance of 2.35 Å and six Si atoms at 2.36 Å (1), 2.68 Å (4), and 2.77 Å (1) [4].



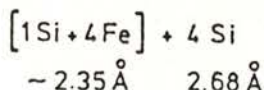
Coordination of Fe( $Z=0$ )



Fe and Si coordinations in the structure of  $\alpha\text{-Fe}_{1-x}\text{Si}_2$  phase are represented in Fig. 1. The structural characteristics of this phase determine, as a result of the above mentioned Fe layer, the bidimensional character of its physical properties.



Coordination of Si( $Z$ )



● — Fe atoms

○ — Si atoms

Fig. 1 -Coordination of Fe and Si atoms in  $\alpha\text{-Fe}_{1-x}\text{Si}_2$  structure.

The stoichiometric  $\beta$  phase has an orthorhombic crystal lattice with parameters  $\mathbf{a} = 9.8795 \pm 0.0005$  Å;  $\mathbf{b} = 7.7977 \pm 0.0003$  Å;  $\mathbf{c} = 7.8392 \pm 0.0003$  Å [8],  $Cmca$  space group symmetry, and contains 48 atoms per unit cell (16 Fe and 32 Si) [9]. This phase has an atomic arrangement corresponding to a severe distortion of fluorite ( $\text{CaF}_2$ ) structure type, with two kinds of deformed  $[\text{FeSi}_8]$  cubes, with Fe atoms in their centers, identified by I and II but in crystallographically distinct equivalent positions (Fig. 2).

Si atoms occupy two crystallographically identical mono-variant equivalent points with distinct positional  $z$  parameters, ( $\text{Si}_I$  and  $\text{Si}_{II}$ ). Si-Si interatomic distances are comparatively more homogeneous (2.51 - 2.59 Å) in  $[\text{Fe}_{II}\text{Si}_8]$  cubes, while in  $[\text{Fe}_I\text{Si}_8]$  cubes such distances give rise to long (3.56 Å) and short (2.45 Å) edges. Consequently,  $\text{Fe}_I$  atoms are geometrically surrounded by Si in a more regular way than  $\text{Fe}_{II}$  atoms, a feature clearly apparent in the Mössbauer spectrum of  $\beta$  phase [8].

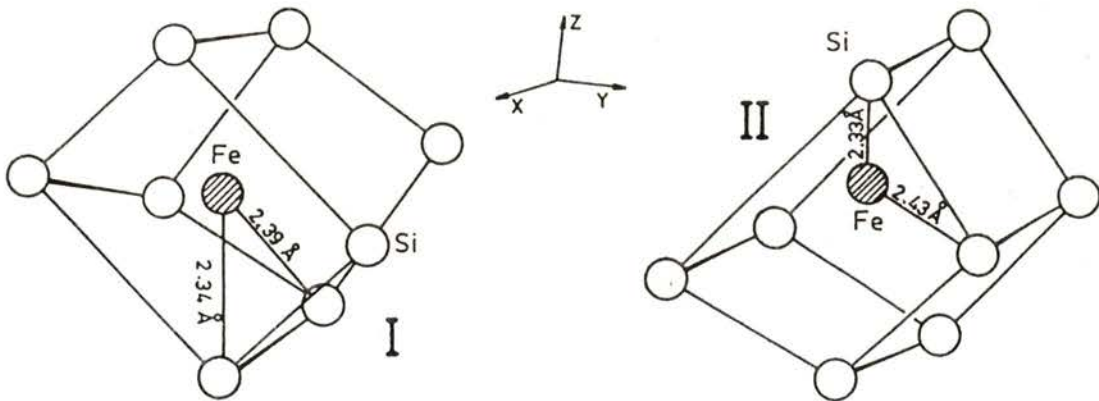


Fig. 2 - Fe coordination in  $\beta$ -FeSi<sub>2</sub> structure.

Si atoms are in an approximately tetrahedral coordination, being surrounded by two Fe<sub>I</sub> and two Fe<sub>II</sub> atoms. This coordination geometry approaches that of Si atoms in silicon "metal" and is quite different from that found in  $\alpha$ -Fe<sub>1-x</sub>Si<sub>2</sub> phase, where each silicon atom is surrounded by four iron atoms and by another silicon atom at a short distance (2.36 Å) plus (1+4)Si atoms at larger distances (2.77 Å+2.68 Å).

The  $\alpha \rightarrow \beta$  transition of FeSi<sub>2</sub> takes place during the cooling of the ferro-silicon alloy, at a temperature close to 1210K, changing from a metallic behaviour at higher temperature to a semiconductor behaviour at lower temperature [10]. The technical importance of FeSi<sub>2</sub> arises from the thermoelectric properties of  $\beta$  phase, and also from its electric properties that show at  $T_1$  a metal-nonmetal transition. According to an

energy band model, this transition is related to the occurrence of vacancies in the Fe sublattice, and therefore it is not a true metal-nonmetal transition in the usual sense [11].  $\beta$ -FeSi<sub>2</sub> is a semiconductor compound of *n* type when doped with cobalt and of *p* type if doped with aluminium impurities.

### 3 - CONTRIBUTION TO THE MECHANISM OF $\alpha \rightarrow \beta$ "FeSi<sub>2</sub>" STRUCTURAL TRANSITION

The mechanism of the  $\alpha \rightarrow \beta$  transformation was explained by some previous authors within a structural [12,13] or crystallographic [14] framework, but it may also be explained using crystalchemical data.

$\alpha$ -Fe<sub>1-x</sub>Si<sub>2</sub> is grown from a liquid rich in silicon; however, owing to the large amount of iron present, during the so-

lidification of this phase, Si atoms do not occur in a tetrahedral configuration characteristic of the "metal". A tetragonal Fe-Si phase is formed with two consecutive Si layers, alternating with one Fe layer, and as a result, each Si atom is linked to another Si atom at a short distance (2.36 Å) close to the Si-Si distance in the metal (2.352 Å). This phase can easily accommodate some chemical elements (impurities) which are present in the liquid phase, due to the variety of chemical bonding: quasi metallic for Fe atoms and intermetallic for Si atoms.

On the other hand, the structure of  $\alpha$ -Fe<sub>1-x</sub>Si<sub>2</sub> seems to have a "memory effect", causing an atomic rearrangement leading to the stoichiometric orthorhombic type ( $\beta$ -Fe<sub>1-x</sub>Si<sub>2</sub>), where Si layers alternate with half-filled Fe layers. In this new structure the Si atoms

are not bonded to each other, but tetrahedrally surrounded by Fe atoms, in an environment geometrically similar to that of Si "metal". The plane of Fe atoms in the  $\alpha$  phase separates into two levels during the structural rearrangement, thus breaking the Si-Si double layer and giving rise to alternate [Si<sub>2</sub>-Fe-Si<sub>2</sub>-Fe] layers in  $\beta$  phase. Physical properties displayed by these two FeSi<sub>2</sub> phases agree with this mechanism, the  $\alpha$  phase exhibiting metallic behaviour due to Fe quadrangular layers identical to those present in iron metal. Conversely,  $\beta$  phase exhibits semiconductor properties similar to those of metallic silicon.

(001) and (100) planes of  $\alpha$  and  $\beta$  phases respectively, are represented in Fig. 3. By comparing lattice parameters it is clear that  $a_\beta = 2c_\alpha$  and  $b_\beta = c_\beta = 2\sqrt{2}a_\alpha$ .

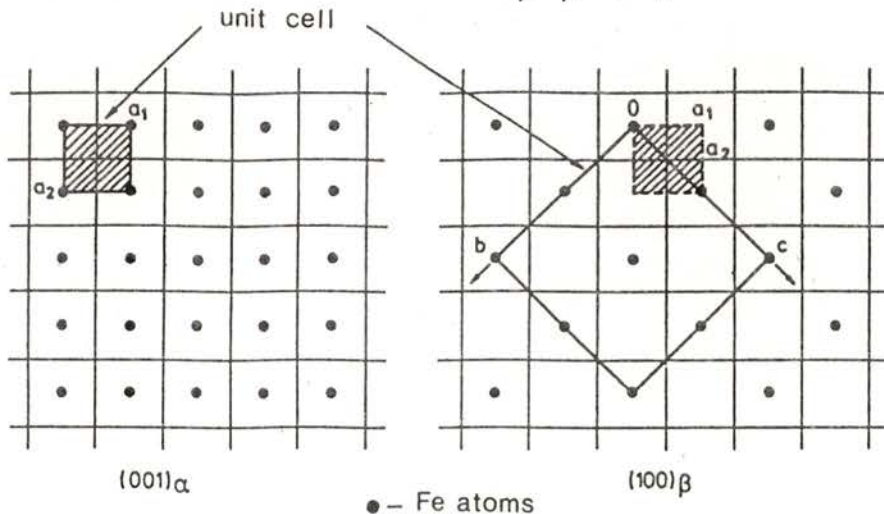


Fig. 3 - Sketch of (001) and (100) planes of  $\alpha$  and  $\beta$  phase, respectively, at the level of Fe layer.

#### 4 - EXPERIMENTAL RESULTS

A structural characterization by X-ray diffraction (XRD) and microstructural observations by scanning electron microscopy (SEM-EDS) were performed on four alloys with 75 wt. % Si and other chemical elements.

X-ray diffraction patterns (XRPD) were recorded in a non-automated Phillips powder diffractometer under optimized instrumental conditions, namely a curved graphite crystal monochromator, small aperture slits and a scanning speed of  $(1/4)^\circ 2\theta.\text{min}^{-1}$ . The following phases were found:  $\alpha\text{-Fe}_{1-x}\text{Si}_2$  (tetrag.),  $\beta\text{-Fe}_{1-x}\text{Si}_2$  (orthorh.),  $\text{CaAl}_2\text{Si}_{1.5}$ ,  $\text{CaSi}_2$  and Al-Fe-Si.

A distinct asymmetry in the " $\alpha\text{-Fe}_{1-x}\text{Si}_2$ " X-ray reflections was detected which was tentatively ascribed to the presence of calcium and aluminium impurities in solid solution. This would imply the coexistence of the major  $\alpha\text{-Fe}_{1-x}\text{Si}_2$  phase (practically free from Ca and Al) with domains containing a minor Al-Si-Ca phase plus a quaternary Fe-Si-Ca-Al phase isostructural with  $\alpha$ -leboite.

The crystalchemical model could explain the presence of such quaternary Fe-Si-Ca-Al phase, in view of the structural similarity with the binary phase  $\alpha\text{-Fe}_{1-x}\text{Si}_2$  [15]. In fact, the domains with quaternary composition, observed by SEM-EDS and which do not correspond

to an explicit phase in the XRPD pattern, can be related to the asymmetry effect just mentioned.

The equidistances ( $d, \text{\AA}$ ) of hkl reflections of  $\text{FeSi}_2$  phases were calibrated against coexisting silicon as an internal standard. 28 reflections observed for " $\alpha\text{-Fe}_{1-x}\text{Si}_2$ " phases (binary and quaternary) were recorded at least three times each, and the mean value of the areas under the peaks were used as a weighing of the intensities of the X-ray spectra.

The two  $\text{FeSi}_2$  "phases" with tetragonal structure and slightly different lattice parameters turned out to be very important. The presence of this quaternary phase has implications on the hydrometallurgical treatment of industrial Fe-Si alloys, which will be more liable to chemical attack due to internal stresses. Its presence could, therefore, benefit the hydrometallurgical processing of ferro-silicon alloys for silicon production.

#### 5 - STRUCTURE AND COMPOSITION OF THE QUATERNARY PHASE Fe-Al-Si-Ca

Four different structural models were considered for the structural analysis of the quaternary phase and calculation of the structure factors. These models differ due to the nature and distribution of substitutional impurities (Ca and Al) and other structural defects (vacancies):

model I - stoichiometric  $\text{FeSi}_2$ ; model II - non-stoichiometric, with 20% vacant iron sites ( $\text{Fe}_{0.8}\text{Si}_2$ ); model III - still defective, with some aluminium replacing iron and some calcium substituting for silicon, with the formula  $(\text{Fe}_{0.8}\text{Al}_{0.1}\square_{0.1})(\text{Si}_{0.8}\text{Ca}_{0.2})_2$ ; model IV - stoichiometric, with calcium partially replacing silicon, with the formula  $\text{Fe}(\text{Si}_{0.8}\text{Ca}_{0.2})_2$ .

For each model three hypothetical values of the positional z parameter of the equivalent position 2(h) occupied by Si atoms were deduced. This parameter influences directly the Si-Si interatomic distance in  $\alpha$ -leboite crystal structure, being therefore sensitive to any extensive replacement of silicon in the ideal structural models.

The discrepancy factor (R %) of each model was obtained by comparing the intensities diffracted by  $\alpha$ - $\text{Fe}_{1-x}\text{Si}_2$  phases to those calculated from the proposed model. The best (minimum) discrepancy factor is attained for model III -  $(\text{Fe}_{0.8}\text{Al}_{0.1}\square_{0.1})(\text{Si}_{0.8}\text{Ca}_{0.2})_2$  and z close to 0.28 (R = 18%). Consequently the quaternary phase detected in this study will have a tetragonal crystal structure similar to  $\alpha$ -leboite, with unit cell parameters  $a = 2.69$  (0) Å,  $c = 5.1$  (9) Å. We called this phase "Caalsifer" [16] in order to stress its quaternary constitution.

A high R' value relating observed and calculated intensities for model III is ac-

ceptable in view of the reduced number of reflections used for the structural analysis (necessarily performed over the industrial composite) and given the low concentration of iron disilicide in these alloys. The structure model of the Caalsifer phase is shown in Fig.4.

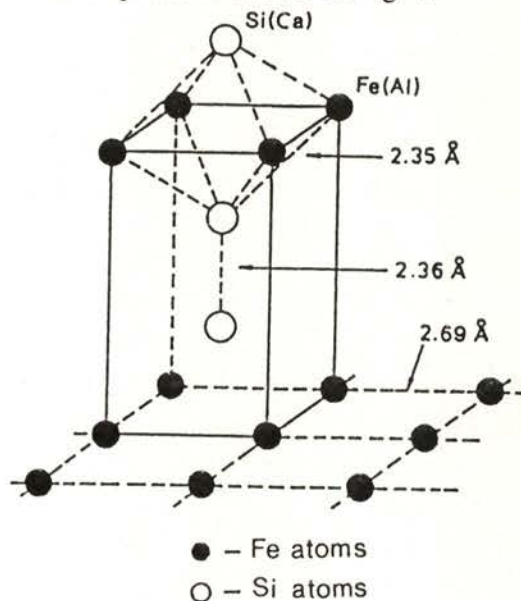


Fig. 4 - Structural model of Caalsifer phase.

## 6 - HINDERING MECHANISM OF $\alpha \rightarrow \beta$ "FeSi<sub>2</sub>" STRUCTURAL TRANSITION.

The structural study of Fe-Si alloys with 75 wt. % Si shows that the formation, during cooling, of the stable phase at room temperature  $\beta$ - $\text{FeSi}_2$  (orthorh.), is intrinsically associated to the precipitation of binary phases Ca-Si and ternary Ca-Al-Si and Al-Si-Fe phases. Even in alloys with similar content of

impurities (Ca and Al), the amounts of these spurious phases are clearly lower when the high temperature phase  $\alpha\text{-Fe}_{1-x}\text{Si}_2$  (tetrag.) remains metastable at room temperature, e.g., when domains of the binary phase  $\alpha\text{-Fe}_{1-x}\text{Si}_2$  coexist with the quaternary phase,  $(\text{Fe}_{0.8}\text{Al}_{0.1}\text{Si}_{0.1})_2(\text{Si}_{0.8}\text{Ca}_{0.2})_2$ .

It was checked that the  $\alpha \rightarrow \beta$  transformation was effectively hindered by the formation of the quaternary phase [17].

The presence of useful impurities in the right amounts allows the stabilization of the quaternary phase and prevents the formation of the stoichiometric compound  $\beta\text{-FeSi}_2$  (Fig. 5) which is stable at low temperature.

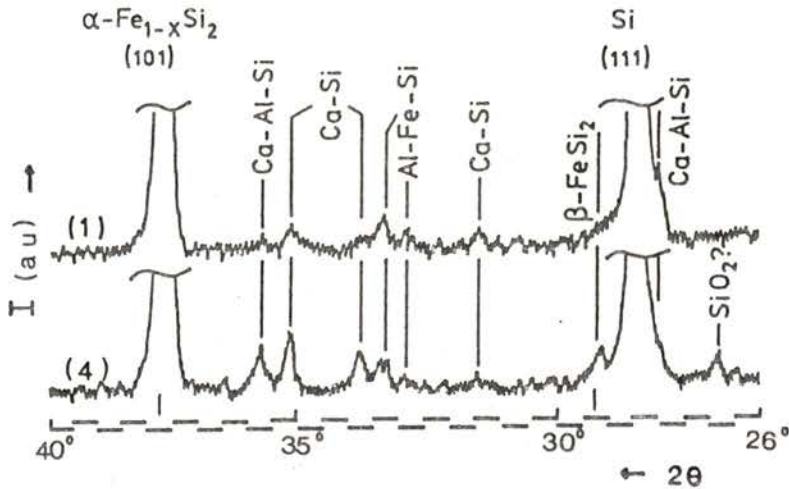


Fig. 5 - XRPD patterns (Cu  $K\alpha$  radiation) and phase identification.

Actually, when  $\beta$  phase precipitation is observed, the content of impurities in the remanent phase is reduced and several extra compounds are formed - binary Ca-Si and ternary Ca-Al-Si and Al-Fe-Si; on the other hand, for alloys where the  $\alpha$  phase is abundant at room temperature, the precipitation of  $\beta$  phase is not

significant and the content of extra phases is attenuated.

It was inferred that the joint incorporation of two elements with different structural functions - Ca and Al - in  $\alpha$ -leboite structure, improves the stability of this phase, preventing the  $\alpha \rightarrow \beta + \text{Si}$  eutectoid transformation to take place.

## 7 - CONCLUSIONS

In spite of the low concentration of quaternary phase Caalsifer in ferro-silicon alloys, and of the reduced number of measurable reflections in the X-ray diffraction pattern, the discrepancy factor obtained in the present structural study suggests that, beyond the normal  $\alpha$ -Fe<sub>1-x</sub>Si<sub>2</sub> phase, domains of defect concentration are present containing a Fe-Si-Ca-Al phase, isostructural with  $\alpha$ -leboite, with approximate formula (Fe<sub>0.8</sub>Al<sub>0.1</sub>□<sub>0.1</sub>)(Si<sub>0.8</sub>Ca<sub>0.2</sub>)<sub>2</sub>. A relevant conclusion is that Al replaces Fe, whose sublattice still keeps vacancies while Ca replaces preferably Si.

The positional z parameter of Si/Ca atoms will be close to 0.28 (0.27 for  $\alpha$ -leboite). Taken together with the increase in lattice parameter c it implies that both interatomic distances Fe-Si(Ca) and Si(Ca)-Si(Ca) will increase.

On the other hand, the fact that the lattice parameter a does not change, implies that the Fe(Al)-Fe(Al) distances are kept approximately constants. This is in agreement with the close atomic dimensions of the two metals, Fe and Al.

It is then confirmed that in industrial Fe-Si alloys where a high amount of impurities and a proper Ca/Al ratio occur, a quaternary phase isotypic with  $\alpha$ -leboite (FeSi<sub>2</sub> tetrag.) will be present.

The importance of the quaternary phase, whose structural study was done under

particularly unfavourable conditions, makes it necessary that laboratory synthesis of alloys with this phase clearly dominant should be made, in order to achieve the desirable crystal structure refinement.

## REFERENCES

- [1] Dehuff, J. A., Coppolechia, V. D. and Lesnewich, A., The Electric Furnace Proceedings, AIME, **27** 167/74 (1969).
- [2] Margarido, F., Figueiredo, M. O. and Bastos, M. H. . 2º Encontro Sociedade Portuguesa de Materiais, Porto, Actas, Tema I, 16 pp (1985).
- [3] Aas, H. , The Silgrain Process: Silicon Metal From 90% FerroSilicon, AIME STP **A71-47**, 653, (1971).
- [4] Aronsson, B., Acta Chem. Scand., **14**, 1414/18, (1960).
- [5] Sidorenko, F. A., Ryzhenko, B. V., El'ner, V. Ya and Gel'd, P. V., Sov. Phys. JETP, **43**, **3**, 518/21, (1976).
- [6] Schubert, K., Zeit. Kristall., **179**, 192/3, (1987).
- [7] Sidorenko, F. A., El'ner, V. Ya., Ryzhenko, B. V. and Gel'd, P. V., Sov. Phys. Solid State, **21**, **4**, 705/6, (1979).
- [8] Wandji, R., Le Corre, C., Genin, J. M. and Roques, B., Phys. Stat. Sol. (b), **45**, K123/7, (1971).
- [9] Wäppling, R., Häggström and Rundqvist, S., Chemical Phys. Letters, **2**, **3**, 160/1, (1968).

- [10] Nishida, I., *Phys. Rev. B*, **7**, **6**, 2710/3, (1973).
- [11] Blauw, C., Woude, F. and Sawatzky, G. A., *J. Phys. C. Solid State Phys.*, **6**, **14**, 2371/81, (1973).
- [12] Kojima, T., Masumoto, K. and Nishida, I., *J. Japan. Inst. Metals*, **48**, **8**, 843/7, (1984).
- [13] Boomgaard, J., *J. Iron Steel Inst.* **210**, 276/9, (1972).
- [14] Le Corre, C. and Genin, J. M., *Phys. Stat. Sol. (b)*, **51**, K85/8, (1972).
- [15] Figueiredo, M.O. and Margarido, F., II Simpósio Ibérico de Física da Matéria Condensada, Sevilha (communication), (1986).
- [16] Margarido, F. and Figueiredo, M.O., *Materials Science and Engineering*, **A104**, 249/54, (1988).
- [17] Margarido, F., Figueiredo, M.O. and Bastos, M. H., 5<sup>a</sup> Conferência da Sociedade Portuguesa de Física, Braga (communication), (1986).

## ELECTRON DENSITY STUDIES IN THE LAVES PHASE $\text{FeBe}_2$

M.M.R. COSTA, M.J.M. DE ALMEIDA AND J.A. PAIXÃO

Centro FC1, INIC - Department of Physics - University of Coimbra 3000 COIMBRA, PORTUGAL

[Received January 1992]

**ABSTRACT** -The main features of the charge density distribution in the hexagonal Laves phase  $\text{FeBe}_2$  have been deduced from preliminary studies based on X-ray diffraction measurements carried out at room temperature in one single crystal.

Thermal and positional parameters were obtained from a spherical refinement of high order data; final agreement factors  $R=2.1\%$  and  $R_w=2.5\%$  were obtained. Difference density maps were calculated using these refined values. Finally the results are summarized and briefly discussed.

### 1 - INTRODUCTION

The structure of Laves phase compounds with stoichiometric composition  $\text{AB}_2$  can be described in terms of the stacking of triangular nets of A and B atoms between Kagamé nets of B atoms. Different possibilities for this stacking give rise to distinct structural types, namely the  $\text{MgZn}_2$  (C14) and  $\text{MgNi}_2$  (C36) hexagonal structures and the  $\text{MgCu}_2$  (C15) cubic structure. These have been first proposed by Friauf [1] and Laves et al. [2]; a review of crystal and band structures and physical properties of Laves phases has been given by Sinha [3].

The size of constituent atoms has been assumed to be determinant in the formation of Laves phase compounds; the ideal ratio  $R_A/R_B$  corresponding to closest packing is 1.225. However, several Laves phases are known to exist with values of  $R_A/R_B$  ranging from 1.05 to 1.68.

Several authors [4,5] have suggested that a close relationship also exists between the crystallographic structure and the electron concentration  $e/a$ . This assumption is supported by the occurrence of phase boundaries for the three types of structure at the same values of  $e/a$ , for several systems investigated.

Electron densities in binary Laves phases with transition metals for which  $R_A/R_B \neq 1.225$  have been determined in this Laboratory by X-ray diffraction. The deviation of  $R_A/R_B$  from the ideal value suggests changes in the valence of the constituent atoms, which should be detectable in careful electron distribution studies.

The presence of two transition elements with rather similar atomic numbers in the Laves phases investigated, TiCo<sub>2</sub> [6], TiMn<sub>2</sub> [7] and TiFe<sub>2</sub> [7] is, in a way, an unfavourable situation when investigating eventual departures from spherical symmetry.

Therefore it was decided to carry out similar studies in the binary Laves phase FeBe<sub>2</sub> with only one transition metal, the other constituent being a non transition light element. For this alloy  $R_A/R_B = 1.129$ .

## 2 - CRYSTAL DATA AND EXPERIMENTAL

The Laves phase FeBe<sub>2</sub> has the MgZn<sub>2</sub> (C14) hexagonal structure, with space group P6<sub>3</sub>/mmc. Atomic positions the unit cell are shown in fig.1.

A single crystal with approximate dimensions (0.07×0.07×0.08)mm<sup>3</sup> was selected from the material kindly offered by Dr. P.J. Brown, Institut Laue Langevin, Grenoble, France.

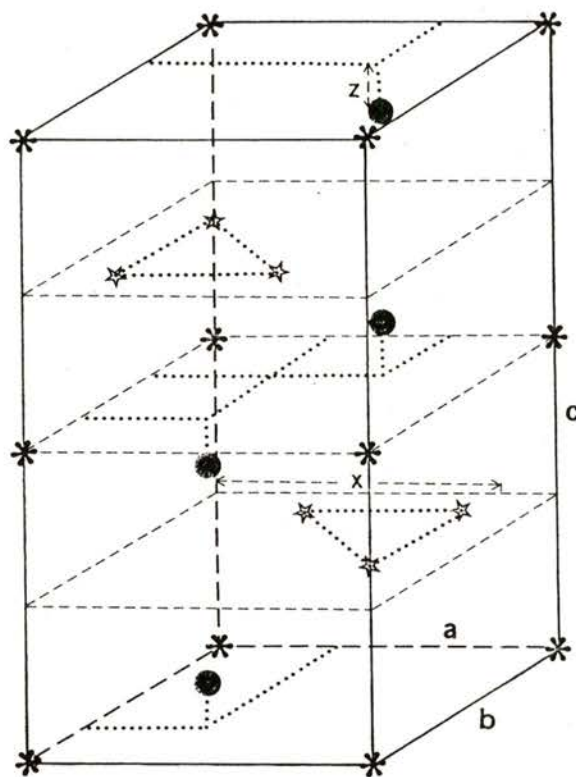


Fig.1 - Unit cell of Laves phase with C14 hexagonal structure: ● - Fe atoms; \* - Be(I) atoms; ☆ - Be(II) atoms

Diffraction data were collected on a single crystal diffractometer CAD4, using Mo-K $\alpha$  radiation ( $\lambda = 0.7017\text{\AA}$ ) and a graphite (002) monochromator. The absorption coefficient of the alloy for this type of radiation is  $\mu = 66.1\text{cm}^{-1}$ .

Lattice parameters were refined using a standard least-squares technique and the CAD4 available software, from 25 reflections with  $11.8^\circ < 2\theta < 60.5^\circ$ :

$$\begin{aligned} a &= b = 4.2224(10)\text{\AA} \\ c &= 6.8700(11)\text{\AA} \end{aligned}$$

$$\alpha = \beta = 90^\circ ; \quad \gamma = 120^\circ$$

A set of 6527 independent reflections out to  $\sin\theta/\lambda=1.1\text{\AA}^{-1}$  in reciprocal space were measured at room temperature ( $293\pm 2$  K) using  $\omega$ - $2\theta$  scans. For each  $hkl$ , up to 24 symmetry-equivalent reflections were measured in order to evaluate and correct for absorption effects.

Five standard reflections were measured every 3 hours; maximum fluctuations of 4% over an exposure period of 272 hours were detected and attributed to variations of the main beam intensity and detector sensitivity. All intensities were rescaled against the standards in order to correct for this effect.

The orientation of the sample was checked after measuring every 60 reflections. Whenever the direction of the scattering vector was found to differ more than 10% from that derived from the UB matrix, a set of 5 reflections previously selected was measured in order to re-orientate the crystal.

### 3 - DATA ANALYSIS

The analysis of the experimental data was performed with the SDP-Plus programs [8] using a MICROVAX II with VMS operating system.

Lorentz and polarization corrections appropriate to the current geometry were

applied to the integrated intensities. An absorption correction based on psi-scans of a few reflections with  $\chi$  close to  $90^\circ$  and of their geometrically accessible equivalents suggested by North *et al* [9] was applied to the data. Relevant information concerning this correction is presented in Table 1.

Maximum absorption correction	0.9965
Minimum absorption correction	0.8167
Agreement factors ( $F_{\text{obs}}$ )	0.042

Table 1 - Relevant information concerning absorption correction applied to the data.

Averaging of equivalent reflections was subsequently performed, the total number of non-equivalent intensities being 441. Those average intensities for which  $I_{hkl} \leq 3\sigma_{hkl}$ ,  $\sigma_{hkl}$  being the standard deviation of  $I_{hkl}$ , were considered "non-observed"; 129 "observed" reflections were thus obtained.

A set of structure factors for the observed reflections were calculated ( $F_{\text{calc}}$ ) assuming spherical distributions of atomic electrons. Anomalous dispersion corrections were included in the atomic scattering factors using data listed on The International Tables for X-Ray Crystallography [10]. Full matrix least-squares refinements based on  $(F_{\text{obs}} - F_{\text{calc}})^2$  were performed on the observed

data set. A non-Poisson contribution weighting scheme was used, the weight  $w$  of each reflection being calculated as

$$w = 1/(\sigma_F)^2$$

with

$$\sigma_F = \sigma_{F^2} / 2F$$

and

$$\sigma_{F^2} = [\sigma_I^2 + (pF^2)^2]^{1/2}$$

where a value of 0.04 for the instrumental instability factor  $p$  was used to downweight the most intense reflections. Positional and anisotropic thermal parameters  $U_{ij}$  together with a scale factor  $S$  were refined using high angle data which included only 89 reflections with  $[(\sin\theta)/\lambda] \geq 0.6 \text{ \AA}^{-1}$  [11]. Refinements were carried out until a shift/e.s.d. ratio smaller than 0.001 was achieved for all the parameters. Using the structure amplitudes of all observed reflections [out to  $(\sin\theta)/\lambda = 1.1 \text{ \AA}^{-1}$ ] and fixing the refined values of the above parameters, an extinction parameter  $g$  was independently refined using the approximate relationship:

$$|F_{\text{calc}}| = |F_{\text{obs}}| (1 + gI_{\text{calc}})$$

derived by Stout and Jensen [12].

Values of the ratio  $F_{\text{obs}}^{\text{corr}}/F_{\text{obs}}$  for reflections with  $w(F_{\text{calc}} - F_{\text{obs}}) \leq 2$ , ranged between 1.142 and 1.003. Table 2 shows the results of the above described refinements.

Indep. refl. with $I > 3\sigma$	129
Indep. refl., $I > 3\sigma$ , $\sin\theta/\lambda > 0.6 \text{ \AA}^{-1}$	89
Fe atom	
z	0.06168(9)
$U_{11}=U_{22}$	0.00501(7)
$U_{12}$	0.00250(4)
$U_{33}$	0.00379(7)
Be <sub>1</sub> atom	
$U_{11}=U_{22}$	0.00141(124)
$U_{12}$	0.00070(62)
$U_{33}$	0.00815(173)
Be <sub>2</sub> atom	
x	0.82905(112)
$U_{11}$	0.00699(95)
$U_{22}$	0.00666(129)
$U_{12}$	0.00333(65)
$U_{33}$	0.00620(70)
R	2.1%
$R_w$	2.5%
g	$8.90(52) \cdot 10^{-6}$
S	0.76895(230)

Table 2 - Positional, thermal and extinction parameters obtained from least squares refinement.

Anisotropic thermal parameters  $U_{ij}$  are based on the following expression for the "temperature factor":

$$T = \exp [-2\pi(h^2a^2U_{11} + k^2b^2U_{22} + l^2c^2U_{33} + 2a*b*hkU_{12})]$$

The anisotropy of vibrations of the light atoms Be(I) which are located along the

edges (c-axis) of the unit cell is a striking feature of this structure, and can be inferred either from a comparison of the magnitude of the parameter  $U_{33}$  with those of  $U_{11}(=U_{22})$  and  $U_{12}$ , or from the observation of the ellipsoids of thermal vibrations shown in fig.2 for this atom and (for the sake of comparison) for Be(II).

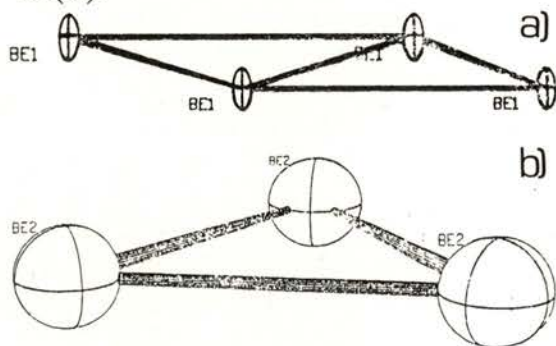


Fig.2 - Ellipsoids of thermal vibrations:

- a) Be(I) atoms; axial ratio:5.8
- b) Be(II) atoms; axial ratio:0.9

#### 4- CHARGE DENSITY RESULTS AND CONCLUSIONS.

Fourier analysis of the observed structure factors was performed, the results of which are represented as density maps. The most representative of these, corresponding to sections of the unit cell through different types of atom are shown in fig.3. The electron density around the Fe (fig.3-b) and Be(II)

(fig.3-a) atomic positions exhibits no apparent unexpected behaviour.

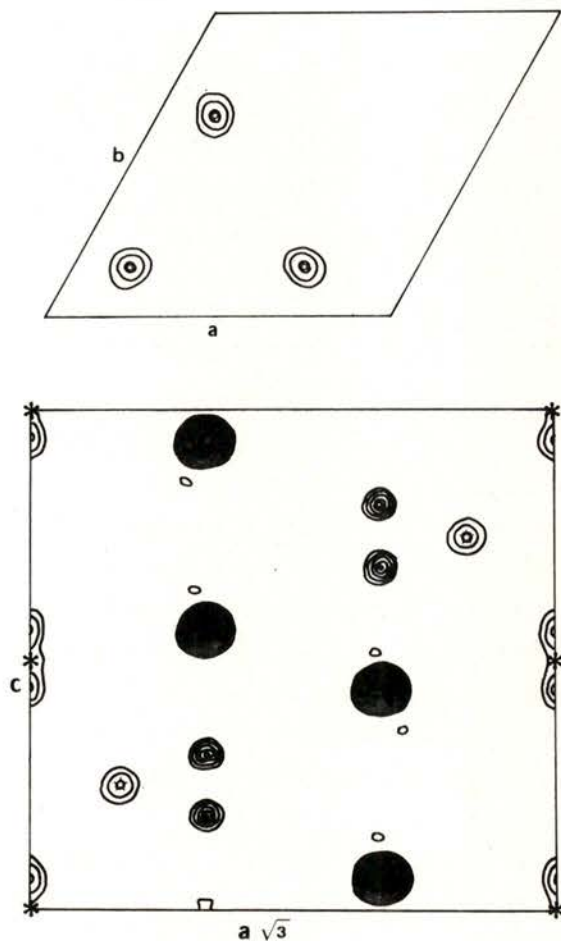


Fig.3 - Fourier maps  $SF_{obs}$ . Contour levels at intervals of  $10 \text{ e}\text{\AA}^{-3}$ : ● - Fe atoms; \* - Be(I) atoms; ☆ - Be(II) atoms.

- a) section [00.1] of the unit cell at  $z=0.25$ .
- b) section [11.0] of the unit cell.

However, at the Be(I) positions (fig.3-b) the density does not have spherical

symmetry; instead two maxima can be seen, symmetrically located with respect to the refined atomic position. Moreover, the density map for section [11.0] (fig.3-b) shows density maxima above and below the triangular arrangement of Be(II) atoms on a line running through the center of the triangles and through the Fe atoms. These maxima correspond to a significantly higher density than that observed at the Be(II) atomic positions.

Subsequent Fourier analysis of the differences ( $SF_{\text{obs}} - F_{\text{calc}}$ ) was carried out in order to investigate the origin of the observed effects. The corresponding difference maps are shown in fig.4 the significance level of which can be compared with the error maps in fig.5. The standard deviation of constant regions is  $0.3e\text{\AA}^{-3}$ . Observation of the difference maps shows that both the effect at the Be(I) positions and that occurring below and above the triangles of Be(II) atoms have disappeared.

Hence, it appears that the correction for thermal motion applied to the  $F_{\text{calc}}$  has taken care of the "anomalies" observed in direct maps. Their origin may therefore be attributed to thermal vibrations perhaps mainly associated with the light Be atoms.

It may also be argued that the models used for correction of absorption and extinction in this crystal are not satisfactory. Furthermore, an eventual twinning effect should also be considered.

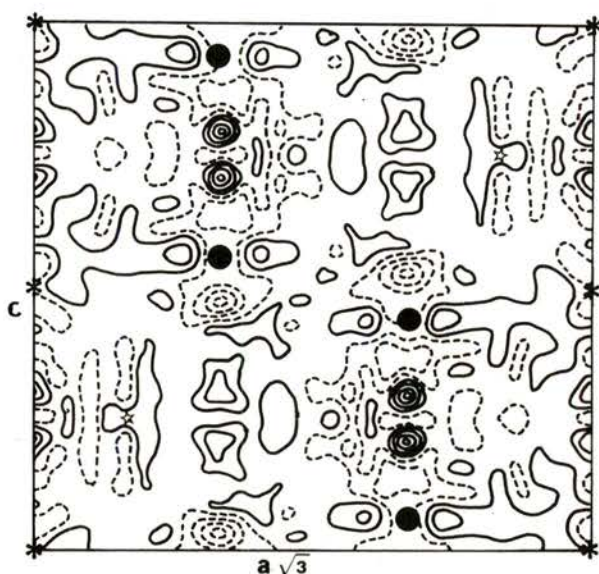
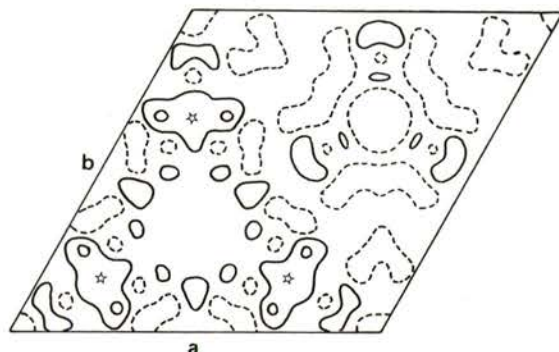


Fig.4 - Fourier difference maps,  $SF_{\text{obs}} - F_{\text{calc}}$ . Contour levels at intervals of  $0.4 e\text{\AA}^{-3}$ . First positive contour at  $0.2 e\text{\AA}^{-3}$ .

- - Fe atoms; \* - Be(I) atoms; ☆ - Be(II) atoms
- a) section [00.1] of the unit cell at  $z=0.25$
- b) section [11.0] of the unit cell.

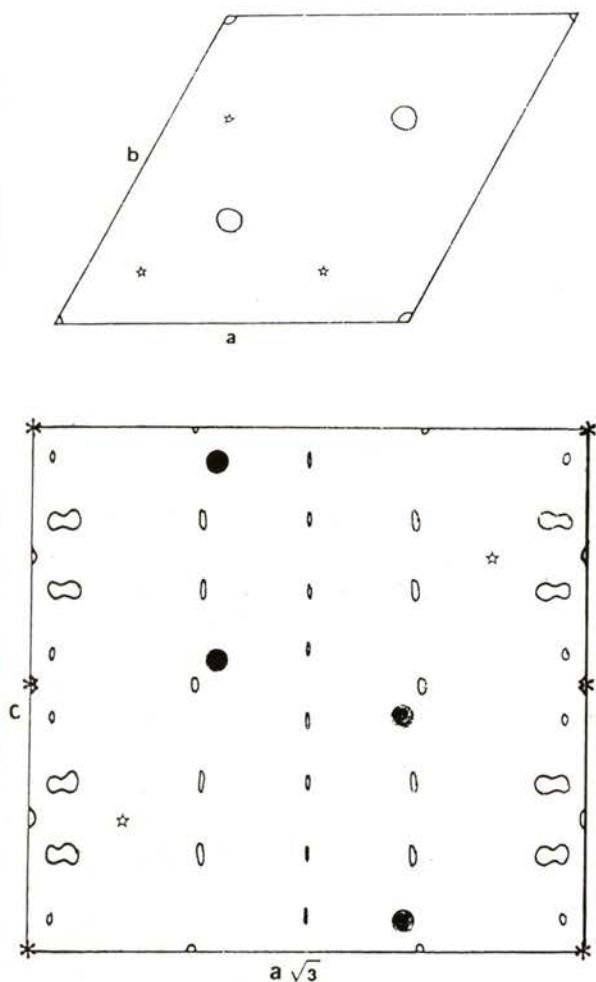


Fig.5 - Fourier maps representing the distribution of errors. Contour levels at intervals of  $0.4 \text{ e}\text{\AA}^{-3}$ . First positive contour at  $0.2 \text{ e}\text{\AA}^{-3}$ .

- - Fe atoms; \* - Be(I) atoms; ☆ - Be(II) atoms
- a) section [00.1] of the unit cell at  $z=0.25$
- b) section [11.0] of the unit cell.

These possibilities will be tested by selecting another crystal with a different shape and volume, for which absorption and extinction effects and eventual twinning should in principle be different.

Significant remaining features on difference density maps are excess density along the direction parallel to the  $c$ -axis, both between two nearest neighbour Fe atoms and between two Be(I) atoms. However these effects should not be emphasized until those much stronger, observed on direct maps, are fully explained and their presence in the electron density from a different crystal is confirmed.

## ACKNOWLEDGEMENTS

We are indebted to the Cultural Service of the German Federal Republic Embassy, the Deutscher Akademischer Austauschdienst (DAAD) and the German Agency for Technical Cooperation (GTZ) for the offer of a CAD4 automatic diffractometer which enabled the experimental work to be carried out.

## REFERENCES

- [1] Friauf, J.B., *J.Am.Chem.Soc.*, **49**, 3107 (1927).
- [2] Laves, F. and Witte, H., *Metallwirtsch. Metallwiss, Metalltech.*, **14**, 645 (1935).

- [3] Sinha, A.K., *Progress in Materials Science*, **15**, 93 (1972).
- [4] Laves, F. and Witte, H., *Metallwirtsch. Metallwiss, Metalltech.*, **15**, 840 (1936).
- [5] Lieser, K.H. and Witte, H., *Z. Metallkd.*, **43**, 396 (1952).
- [6] Beja, A.M., Alte da Veiga, L., Andrade, L.C.R., Costa, M.M.R. and Paixão, J.A., *Portgal. Phys.*, **19**, 293 (1988).
- [7] Almeida, M.J.M, Costa, M.M.R. and Paixão, J.A., *Portgal. Phys.*, **19**, 289 (1988).
- [8] Frenz, B.A., *Enraf-Nonius Structure Determination Package; SDP Users Guide*, Enraf-Nonius, Delft, The Netherlands.
- [9] North, A.C.T., Phillips, D.C. and Mathews, F.S., *Acta Cryst.* **A24**, 351 (1968)
- [10] *International Tables for X-Ray Crystallography*, vol.III, 1974.
- [11] Stevens, E.D. and Coppens, P., *Acta Cryst.* **A31**, 612 (1975).
- [12] Stout, G.H. and Jensen, L.H., *X-Ray Structure Determination*, 410-412, London: Macmillan (1968).

# ON THE QUANTUM HARMONIC OSCILLATOR WITH TIME-DEPENDENT FREQUENCY

FRANCISCO M. FERNÁNDEZ AND EDUARDO A. CASTRO

Programa QUINOR, Facultad de Ciencias Exactas, UNLP, Calle 47 y 115, C.C. 962, 1900 La Plata, Argentina.

[Received December 1991]

**ABSTRACT**-The time evolution operator for the quantum harmonic oscillator with time-dependent frequency is exactly obtained as a product of unitary operators. The calculation is greatly simplified by taking into account the equations of motion for the coordinate and momentum operators in the Heisenberg representation.

## 1. INTRODUCTION

The driven harmonic oscillator is a useful model for many physical systems of practical interest. Among them we mention lattice vibrations in solids and energy transfer in molecular collisions [1-3]. It is also suitable for teaching purposes because the Schrödinger equation is exactly solvable [1,4].

In this paper we are interested in the harmonic oscillator with time-dependent frequency (units are used so that  $\hbar = m = 1$ ).

$$\mathcal{H} = \frac{1}{2}p^2 + \frac{1}{2}w^2(t)q^2 \quad (1)$$

where  $[q,p] = i$ . It is our purpose to obtain the time evolution operator  $U(t)$

that satisfies the equation

$$i \frac{d}{dt} U = \mathcal{H} U \quad (2)$$

with the boundary condition  $U(0)=1$ . The solution of Eq. (2) can be written

$$U=U_1U_2U_3, \quad U_j = \exp(-ia_j(t)A_j) \quad (3)$$

where  $a_j(0)=0$  and

$$A_1 = \frac{1}{2}q^2, \quad A_2 = \frac{1}{2}(qp+pq), \quad A_3 = \frac{1}{2}p^2 \quad (4)$$

because the operators  $A_j$  form a Lie algebra:

$$\begin{aligned} [A_1, A_2] &= 2i A_1, & [A_1, A_3] &= i A_2, \\ [A_2, A_3] &= 2i A_3 \end{aligned} \quad (5)$$

On introducing Eq. (3) into Eq. (2) we are led to a set of nonlinear differential equations that determine exactly the functions  $a_j(t)$  [5]. Besides, nonlinear functions of the  $a_j$ 's can be found that satisfy classical equations of motion [3,6].

It is shown in the present paper that the latter functions and their relationship with the former ones can be much more easily obtained from the equations of motion for the coordinate and momentum operators in the Heisenberg representation. The procedure is discussed in Sec. 2 and its generalization to more complex problems is briefly outlined in Sec. 3.

## 2. THE METHOD

In the Heisenberg representation any linear operator  $O$  is written

$$O_t = U^\dagger O U \quad (6)$$

which satisfies the well known quantum mechanical equation of motion

$$\frac{d}{dt} O_t = U^\dagger \frac{\partial O}{\partial t} U + i U^\dagger [\mathcal{H}, O_t] U \quad (7)$$

In particular, for the coordinate and momentum we have

$$\frac{d}{dt} q_t = p_t$$

$$\frac{d}{dt} p_t = -w^2 q_t \quad (8)$$

that lead to

$$\frac{d^2}{dt^2} q_t = -w^2 q_t \quad (9)$$

Since the coordinate and momentum form a complete set of observables for the oscillator we expect to obtain all the relevant dynamical information about the system from Eqs. (8).

It is clear that the solution of Eqs. (8) must be of the form

$$\begin{aligned} q_t &= Q_1(t) p + Q_2(t) q \\ p_t &= P_1(t) p + P_2(t) q \end{aligned} \quad (10)$$

Where  $Q_1(0)=P_2(0)=0$  and  $Q_2(0)=P_1(0)=1$ . On introducing (10) into (8) we obtain the classical equations of motion

$$\dot{Q}_j = P_j, \quad \dot{P}_j = -w^2 Q_j, \quad j=1,2 \quad (11)$$

where the dot means time derivative, or

$$\ddot{Q}_j = -w^2 Q_j, \quad j=1,2 \quad (12)$$

Only three of the four functions  $Q_j$  and  $P_j$  are independent since  $[q_t, p_t] = U^\dagger [q, p] U = i$ . Therefore,

$$P_1 Q_2 - P_2 Q_1 = 1 \quad (13)$$

which is actually the Wronskian for the

two independent solutions of (12).

In order to obtain the relationship between the functions  $P_j$ ,  $Q_j$  and the functions  $a_k$  we make use of the results in the Appendix. A straightforward calculation shows that

$$\begin{aligned} U_1^\dagger p U_1 &= p - a_1 q, \\ U_2^\dagger p U_2 &= \exp(-a_2) p, \\ U_2^\dagger q U_2 &= \exp(a_2) q, \\ U_3^\dagger q U_3 &= q + a_3 p, \end{aligned} \quad (14)$$

which lead to (cf Eq. (10))

$$\begin{aligned} P_1 &= \exp(-a_2) - a_1 a_3 \exp(a_3), \\ P_2 &= -a_1 \exp(a_2), \\ Q_1 &= a_3 \exp(a_2), \\ Q_2 &= \exp(a_2). \end{aligned} \quad (15)$$

Finally, the time evolution operator can be written

$$U = \exp\left(\frac{iP_2}{2Q_2}q^2\right)\exp\left(-\frac{i}{2}\ln Q_2(qp+pq)\right)\exp\left(-\frac{iQ_1}{2Q_2}p^2\right) \quad (16)$$

which is the result obtained by Pechukas and Light [6] through a rather more involved procedure. It is worth noticing that the time dependence of the wavefunction  $\psi(t)=U(t)\psi(0)$  is determined by the solutions of the equations of motion for the classical analog of (1).

### 3. CONCLUSIONS

The method developed in the present paper is much simpler than the methods reported previously [3,5,6] because a remarkably less number of commutators is required. The reader can convince himself by obtaining the differential equations for the  $a$ 's from Eqs. (2) and (3) [3,5]. In addition to this, the relationship between the functions  $a_j$  and the functions  $P_j$  and  $Q_j$  follows immediately from the form of the coordinate and momentum operators in the Heisenberg representation.

It must be noticed that the phase factor in  $U$  cannot be obtained from the quantum-mechanical equations of motion. For instance, suppose that

$$\mathcal{H} = \sum_{j=1}^5 \mathcal{H}_j(t) A_j \quad (17)$$

where  $A_4 = q$  and  $A_5 = p$ . Such an operator occurs in the treatment of a collinear collision of an atom with a diatomic molecule [3]. In this case the time evolution operator can be written

$$U = \prod_{j=1}^6 U_j \quad (18)$$

where  $A_6 = 1$ . Clearly, the phase factor  $U_6 = \exp(-ia_6)$  does not appear in  $q_t$  or  $p_t$ . However, it can be easily obtained from (2). For example, direct inspection of the terms in  $(i \frac{d}{dt} U)U^\dagger = \mathcal{H}$  shows that  $A_6 = -A_5 a_4$ .

Owing to its great simplicity the present procedure can be applied to more complex problems. We have obtained the time evolution operator for an  $n$ -dimensional oscillator with linear and bilinear terms in coordinate and momenta and arbitrary time dependent coefficients [7]. Such a model originates, for instance, in the semiclassical approximation to the collision between two molecules [2, 3, 8]. As far as we know only approximate solutions had been tried before for the simplest cases [2, 8].

#### 4. APPENDIX

Throughout this paper we had to calculate expressions of the form

$$\tilde{B}(a) = T^{-1}BT \quad (A1)$$

where  $T = \exp(-iaA)$  and  $A$  and  $B$  are linear operators. This can be easily done by taking into account that

$$\frac{d}{da}\tilde{B} = iT^{-1}[A,B]T \quad (A2)$$

Therefore, the  $n$ th derivative of  $B$  with respect to  $a$  can be written

$$\tilde{B}^{(n)} = i^n T^{-1}B_n T, \quad (A3)$$

where

$$B_n = [A, B_{n-1}], \quad n = 1, 2, \dots, \quad B_0 = B \quad (A4)$$

We are thus led to the Taylor series

$$\tilde{B} = \sum_{j=0}^{\infty} \frac{(ia)^j}{j!} B_j \quad (A5)$$

which reduces to a polynomial of degree  $n$  when  $[A, B_n] = 0$ . As an example consider  $A = p^2$  and  $B = q$  ( $n=1$  in this case).

In some cases it is easier to obtain  $\tilde{B}$  by integrating the differential equation that comes from (A3). If, for instance, it is found that  $\tilde{B}' = g\tilde{B}$  then  $\tilde{B} = e^{ga} B$ . This certainly happens when  $A = qp + pq$  and  $B = p$  or  $B = q$ . Other situations are treated exactly in the same way.

#### REFERENCES

- [1] Band, W., *Am. J. Phys.* **30**, 646 (1962).
- [2] Kelley, J. D., *J. Chem. Phys.* **56**, 6108 (1972); Billing, G. D., *Chem. Phys.* **33**, 227 (1978).
- [3] Gazdy, B. and Micha, D. A., *J. Chem. Phys.* **82**, 4926 (1985).
- [4] Fuller, R. W., Harris, S. M. and Slaggie, E. L., *Am. J. Phys.* **31**, 431 (1963); Scarfone, L. M., *ibid* **32**, 158 (1964); Carruthers, P. and Nieto, M. M., *ibid* **33**, 537 (1965); Gilbey, D. M. and Goodman, F. O., *ibid* **34**, 143 (1966); Ninan, M. M and Stipcevic, Z., *ibid* **37**, 734 (1960).
- [5] Wei, J. and Norman, E., *J. Math. Phys.* **4**,

575 (1963).

[6]Pechukas, P. and Light, J. C., *J. Chem. Phys.* **44**, 3897 (1966).

[7]Fernández, F. M. and Castro, E. A., *Phys.*

*Lett. A* **125**, 77 (1987).

[8]Recamier, J., Micha, D. A. and Gazdy, B., *Chem. Phys. Lett.* **119**, 383 (1985) ; *J. Chem.*

*Phys.* **85**, 5093 (1986).

## THE EMISSION MEASURE AND ULTRAVIOLET SPECTRA OF T TAURI STARS

JOÃO J. F. G. AFONSO LIMA AND MARIA TERESA VAZ TORRÃO LAGO

Grupo de Matemática Aplicada e Centro de Astrofísica da Universidade do Porto Rua do Campo Alegre, 823, 4100 Porto, Portugal

[Received March 1992]

**ABSTRACT** - We present the characteristics of the ultraviolet spectra of T Tauri stars and summarise the relevance of ultraviolet Astronomy and its historical development. The emission measure is discussed and related to the quantification of the material responsible for the observed ultraviolet emission. We compare the ultraviolet data for three T Tauri stars (RU Lupi, T Tauri, GW Orionis) and the Sun and show that the energy emitted by these stars in the temperature range  $10^4$ - $5 \cdot 10^4$  K is typically  $10^3$  times higher than the corresponding solar values. This suggests that the "young" Sun, when only a few  $10^6$  years old and still evolving to the main sequence, must have had a much higher ultraviolet flux than at the present time.

### 1 - INTRODUCTION

#### 1.1 - THE ULTRAVIOLET OBSERVATIONS

Astronomical observations at ground level are limited to the narrow band of visible radiation,  $\lambda$ [3250,10000] Å, a few bands in the infrared ( $\lambda$  [ 2.0,4.4 ]  $\mu\text{m}$ ,  $\lambda$  [ 8,13 ]  $\mu\text{m}$ , around 20  $\mu\text{m}$  and 30  $\mu\text{m}$ ) and the radio bands (mm and cm). Therefore most of the electromagnetic spectra is completely inaccessible even from the best placed observatories.

While in the infrared band the situation can be improved using airborne telescopes, for example the Kuiper Airborne Observatory, this procedure is not possible for most bands, for instance, the absorption of ultraviolet radiation by the ozone layer in the earth's atmosphere requires ultraviolet observations to be made at a height above 100 Km.

Astronomical observations in the ultraviolet are very important since for the most abundant atoms and ions, the most relevant radiative transitions occur at ultraviolet wavelengths, namely in the

region  $\lambda$  [1200,2000]Å. Actually, for atoms and ions of H, C(I,II,III,IV), Si(I,II,III,IV), MgII, etc, the energy differences between the first excited level and the ground level are 5 to 10 eV; therefore, electrons with a Maxwellian velocity distribution characteristic of temperatures between  $10^4$  and  $2 \cdot 10^5$  K have sufficient energy to collisionally excite such atoms or ions that will subsequently produce strong spectral lines through radiative decay. These temperatures are typical of stellar atmospheres, galaxies, HII regions, planetary nebulae and other astrophysical objects that will naturally show a very rich ultraviolet spectrum. Furthermore, the absorption of the ultraviolet photons by the lower temperature materials located between the observer and the object, for example, the circumstellar and interstellar medium (in particular the local one, i. e., at a distance up to 100 parsec) or by intergalactic material will also produce spectral lines that will provide information on the properties of such material. The development of ultraviolet Astronomy is quite recent and comprises essentially three distinct phases:

**First phase** - Balloons and rockets (*Aerobee*) transporting simple photometers were used in the second half of the 1950's.

Scanning measurements were made by means of rockets undergoing free

movement in space [1],[2],[3]. The first ultraviolet spectrophotometric observations of stars [4] were made in the 1960's; the first spectrum with enough resolution to allow the detection of individual lines dates from 1965. This was obtained using similar rockets now stabilized in 3 axis thereby allowing longer exposures [5]. By the end of the decade photometric spectroscopic observations for some of the brighter stars were already available. Very short exposures (of the order of minutes) were achieved even though much longer exposures would be required.

**Second phase** - This phase took place during the 1970's. The measurements were made using satellites within the framework of a programme for ultraviolet Astronomy called **Orbiting Astronomical Observatory (NASA)**. These satellites were equipped with low resolution spectrometers and cameras sensitive in the region  $\lambda$ [1200, 4000] Å. In 1972, the satellite **OA0-C** (also known as **Copernicus**) provided very high resolution observations ( $\lambda/\Delta\lambda \approx 10^5$ ) for very bright stars,  $V \leq 6$ . That same year the first european ultraviolet satellite **TD-1**, carried out a complete spectrophotometric survey (wide band photometry 150-200 Å and a spectroscopic survey in the  $\lambda$ [2000, 3000] Å) for stars of magnitude  $V < 11$ , [6,7].

**Third phase** - This is the period in which space observatories started to be used. The International Ultraviolet Explorer was the first ultraviolet space observatory operated in real time, while the experiments just described were preprogrammed. The satellite IUE (NASA, ESA and SERC), launched in 1978, is equipped with a Ritchey-Chrétien telescope with a mirror of 45 cm, aperture F/15 and field of  $\approx 16'$ . It also has two "echelle" spectrographs, one for short wavelengths,  $\lambda[1150, 1950]\text{\AA}$  and another for long wavelengths,  $\lambda[1900, 3200]\text{\AA}$ . Both operate in two resolution modes:

- low resolution (using only one order and limited to objects with  $V \approx 17$ ) with  $\lambda/\Delta\lambda \approx 300 \rightarrow \Delta\lambda \approx 6$  or  $7 \text{\AA}$ , and
- high resolution (about 50 orders, amplitude  $\approx 20\text{\AA}$ ,  $300 \mu\text{m}$  separation, used for objects of magnitude up to  $V \approx 12$ ) with  $\lambda/\Delta\lambda \approx 10^4 \rightarrow \Delta\lambda \approx 0.1$  to  $0.3 \text{\AA}$ .

The IUE detectors are video cameras that are preceded by ultraviolet to visual photon converters. The image, composed of  $768 \times 768$  pixels is transmitted to earth in real time after being digitised in 256 discrete levels of intensity. The data are then subjected to an elaborate sequence of operations including:

- photometric calibration for each pixel,
- correction for non-linearity of the detector at high intensity levels,
- wavelength calibration,

- weighing each element according to its quality,
- correction for the background noise,
- calibration in flux units of the system telescope/ spectrograph /detector.

In this way we obtain a calibrated spectrum ready for analysis.

## 1.2 - T TAURI STARS

T Tauri are recently formed stars, not older than a few  $10^6$  years and still evolving towards the main sequence. They are low mass stars, typically less than three solar masses and exhibit unusual spectra. This makes their study very interesting, because of their intrinsic properties and also from an evolutionary point of view. We aim at establishing a consistent image of stellar evolution, from the initial stages just after the contraction of dense molecular clouds to the arrival of the stars at the main sequence. There are still important problems of these initial phases of evolution to be understood, namely the role of magnetic fields, the reduction of angular momentum and the phenomena of mass accretion and stellar winds. Related to this problem is the formation of the sun and solar system. The ultraviolet observations of T Tauri stars will help the characterisation of conditions prevailing in their atmospheres and relevant to the establishment of models of stellar structure and evolution. They

also provide a way to study the role of the ultraviolet radiation of the "young" Sun in determining the composition of the primitive earth's atmosphere and consequently the origin of the organic molecules that have preceded life on Earth ([8],[9]). We believe that T Tauri stars are precisely in such phase of evolution and that their study helps to understand the conditions that might have prevailed in the "young" Sun.

$\lambda$ (Å)	line
1239-1243	NV(1)
1301-1306	OI(2), SiIII(4)
1335-1336	CII(1)
1394-1403	SiIV(1)
1548-1551	CIV(1)
1657	CI(2)
1697-1727	FeII(38)
1663	OIII
1808-1817	SiII(1)
1859	AlIII(1)
1892	SiIII(1)
1909	CIII(0.01)
2318-2350	CII,SiII
2600-2630	FeII(1)
2795-2803	MgII(1)
2930-2980	FeII(60)

Table 1-Major lines in the ultraviolet spectrum of T-Tauri stars.

### 1.3 - THE ULTRAVIOLET SPECTRA OF T TAURI STARS.

The ultraviolet spectrum of T Tauri stars is dominated by emission lines, mainly in the region  $\lambda < 2000$  Å. The continuum may also be intense for some stars but there are no absorption lines in that spectral region. For  $\lambda > 2000$  Å, the spectrum is generally more complex and includes a photospheric continuum as well as contributions due possibly to numerous lines of FeII.

The present study deals with only the emission line spectrum and its main characteristics can be summarised in the following way:

- the presence of numerous emission lines as shown on Fig.1. Table 1 gives the identification of the lines, the dominant lines being of OI, CII, SiII, CIII, SiIII, CIV, SiIV, FeII and MgII, although with a degree of intensity varying from star to star; the Mg II lines are generally very strong;

- Fig.1, shows that concerning the level of activity (as shown through the intensity of the observed emission lines) there is no simple correlation between the ultraviolet and the optical spectrum of a star.

From the ultraviolet observations it is possible to estimate the amount of material needed to produce the observed energy for each spectral line. This is the so-called emission measure.

2 - THE EMISSION MEASURE

2.1 - DESCRIPTION

The emission measure analysis was introduced by Pottasch [11] as a technique for the study of both the solar transition region and corona. The first studies combined this method with observations of spectral lines in the solar spectrum originated at similar temperatures; as a result, it was possible to evaluate the relative abundances of the various elements associated with those lines. Subsequently, it became clear that the values of the emission measure, together with the equation of hydrostatic equilibrium, were enough to specify uniquely the structure of the outer layers of the solar atmosphere. More recently, with information gathered by means of artificial satellites (Copernicus and IUE) such type of analysis was extended to other cool stars in which emission lines on the ultraviolet part of the spectrum (therefore characteristic of hot circumstellar regions) were observed.

The determination of the emission measure for a given spectral line requires knowledge of the corresponding energy flux at the surface of the star. In general, for a transition between the atomic levels  $j$  and  $i$ , this flux may be written as [12]

$$F_{ji}^* = \frac{hc}{\lambda} \frac{1}{4\pi R^2} \int_{\Delta V} N_j(\vec{r}) A_{ji} P_{ji}(\vec{r}) d^3 \vec{r} \quad (1)$$

where:

$h$  is the Planck's constant,

$c$  the speed of light,

$\lambda$  the wavelength for the transition between levels  $j$  and  $i$ ,

$R$  the radius of the star,

$A_{ji}$  the probability of spontaneous decay,

$\vec{r}$  the positional vector with respect to the star,

$N_j(\vec{r})$  the density of atoms (or ions) in the state  $j$ , as a function of  $\vec{r}$ .

$P_{ji}(\vec{r})$  the probability for the photons to escape from the star, as a function of  $\vec{r}$ ; it has the value 0.5 if we assume that only those photons emitted by the half side of the star facing the observer contribute to the flux.

Assuming that  $\Delta V$  is the volume of a shell of material with spherical symmetry, between radius  $R$  and  $R+\Delta R$ , with  $\Delta R \ll R$ , and using as parameter the height  $h$ , measured from the bottom of the atmosphere, we get

$$F_{ji}^* = \frac{1}{2} \frac{hc}{\lambda} \int_{\Delta V} N_j(h) A_{ji} dh. \quad (2)$$

$N_j$  can be calculated from the equations of statistical equilibrium. Assuming that the atoms are kept in equilibrium through

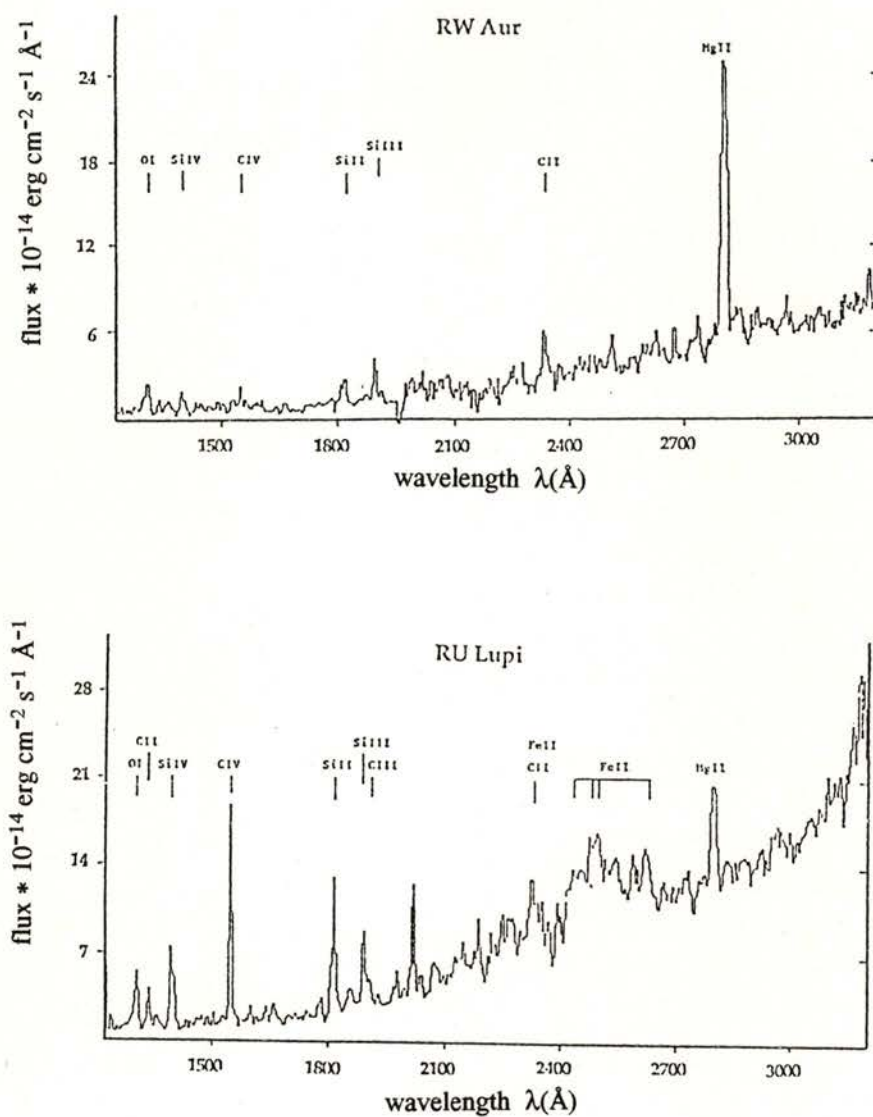


Fig. 1 - Ultraviolet spectrum for the stars RW Aur and RU Lupi. Although these two stars show very similar spectra in the visible region, the intensity of the different emission lines[10] of their ultraviolet counterparts are very different.

collisions and that each excitation by collision is followed by a radiative decay by which the electron returns to its initial stage, the equation of statistical equilibrium takes the simple form

$$N_j A_{ji} = N_i C_{ij} \quad (3)$$

in which  $C_{ij}$  represents the collision rate for electrons on level  $i$  to "ascend" to level  $j$ . Usually such values are not known. Instead, we use the dimensionless quantity  $f_{ij}$ , the "oscillator strength", whose value depends on the intensity of the spectral line and the number of corresponding classical oscillators. The values  $C_{ij}$  can be obtained from the expression of Van Regemorter [13],

$$C_{ij} = 1.7 \cdot 10^{-3} N_e T_e^{-0.5} \chi^{-1} f_{ij} 10^{-(5040\chi/T_e)} P(\chi/k_B T_e) \quad (4)$$

where:

$k_B$  is the Boltzmann constant,  
 $T_e$  the electronic temperature,  
 $N_e$  the electronic density,  
 $\chi$  the excitation energy in eV,  
 $P(\chi/k_B T_e)$  the Gaunt factor (integrated in energy), usually identified by the letter  $g$ .

On the other hand,  $N_i$  can be expressed as

$$N_i = N_e \frac{N_H}{N_e} \frac{N_{el}}{N_H} \frac{N_i}{N_{el}} \quad (5)$$

where:

$N_H$  is the density of hydrogen,  
 $N_{el}$  is the density of the element in all states of ionisation.

For the typical temperatures involved ( $T \sim 10^5 K$ ), hydrogen and helium are almost completely ionised, and we can use the approximation

$$N_e \approx N_H + 2N_{He} \quad (6)$$

For a typical ratio  $N_{He}/N_H = 1/10$ , this gives

$$N_H = 0.8N_e \quad (7)$$

Substituting equations (3), (4), (5) and (7) in equation (2), denoting by  $A$  the abundance of the element ( $N_{el}/N_H$ ), and dropping the indexes  $ij$ , we get

$$F^* = 6.8 \cdot 10^{-4} \frac{hc}{\lambda} \chi^{-1} A g f \int_{\Delta h} G(T_e) N_e^2 dh \quad (8)$$

were

$$G(T_e) = T_e^{-0.5} 10^{-(5040\chi/T_e)} N_i/N_{el} \quad (9)$$

Pottasch [11] in his calculation, replaces the  $G(T_e)$  within the integral by a mean value

$$\langle G(T_e) \rangle = 0.7 G_{\max}(T_m), \quad (10)$$

where  $G_{\max}(T_m)$  is the maximum value of  $G(T_e)$ . He then obtains

$$F^* = 2.97 \cdot 10^{-15} \text{ Agf } G_{\max}(T_m) \int_{\Delta h} N_e^2 dh. \quad (11)$$

The term

$$\int_{\Delta h} N_e^2 dh$$

is called **emission measure (EM)**. It represents the quantity of material needed to produce all the energy flux observed in the emission line, assuming that the line was formed at a single temperature  $T_m$  corresponding to the maximum of the function  $G(T_e)$ . A more refined procedure would need the determination of the normalisation factor (equal to 0.7 in this case) for each spectral line, through the numerical integration of  $G(T_e)$  over a temperature range including  $T_m$ .

## 2.2 - ATOMIC PARAMETERS

Table 2 gives the atomic parameters for the lines of interest in the ultraviolet spectrum of T Tauri stars.

The value of  $gf$  for line 1 is given by [12]; all the others were calculated by means of the equation [15]

$$gf = \frac{6.28 \cdot 10^{-7} \Omega}{\lambda \omega} \quad (12)$$

using the values of the collision strength,  $\Omega$ , and the statistical weight  $\omega$  referred in [14]. In the case of ions with two energy levels in the fundamental state, we use an average value of  $gf$  given by

$$\langle gf \rangle = \frac{\omega_1 f_1 g_1 + \omega_2 f_2 g_2}{\omega_1 + \omega_2} \quad (13)$$

in which the indexes 1 and 2 identify the levels.

line	$\lambda$ (Å)	$gf$	$N_i/N_{el}$	$T_m$
1. CII	1335.3	1.3	1.00	$4.0 \cdot 10^4$
2. SiIV	1398	0.18	0.16	$7.4 \cdot 10^4$
3. CIV	1550	0.23	0.25	$1.1 \cdot 10^5$
4. SiII	1812	0.00237	0.91	$1.5 \cdot 10^4$

Table 2-Atomic parameters for the relevant spectral lines.

The values used for the abundances of carbon and silicon were  $3.2 \cdot 10^{-4}$  and  $6.3 \cdot 10^{-5}$  respectively. The values of

$N_i/N_{el}$  are listed in reference [13];  $T_m$  for the spectrum line 4 is that of reference [13] and the values for all

the other lines are given in reference [16].

T TAURI				
line	$F_{obs}$ (erg cm <sup>-2</sup> s <sup>-1</sup> )	$F^*$ (erg cm <sup>-2</sup> s <sup>-1</sup> )	$F^*/F_{\odot}$	EM (cm <sup>-5</sup> )
1. CII	6.80 10 <sup>-14</sup>	4.34 10 <sup>6</sup>	6.57 10 <sup>2</sup>	1.04 10 <sup>28</sup>
2. SiIV	1.70 10 <sup>-13</sup>	8.91 10 <sup>6</sup>	2.47 10 <sup>3</sup>	1.76 10 <sup>30</sup>
3. CIV	4.60 10 <sup>-13</sup>	2.08 10 <sup>7</sup>	3.19 10 <sup>3</sup>	2.97 10 <sup>29</sup>
4. SiII	2.20 10 <sup>-13</sup>	8.58 10 <sup>6</sup>	3.62 10 <sup>2</sup>	5.18 10 <sup>32</sup>

RU LUPI				
line	$F_{obs}$ (erg cm <sup>-2</sup> s <sup>-1</sup> )	$F^*$ (erg cm <sup>-2</sup> s <sup>-1</sup> )	$F^*/F_{\odot}$	EM (cm <sup>-5</sup> )
1. CII	3.90 10 <sup>-13</sup>	2.76 10 <sup>7</sup>	4.18 10 <sup>2</sup>	6.59 10 <sup>28</sup>
2. SiIV	9.10 10 <sup>-13</sup>	5.91 10 <sup>7</sup>	1.64 10 <sup>4</sup>	1.17 10 <sup>31</sup>
3. CIV	1.50 10 <sup>-12</sup>	9.16 10 <sup>7</sup>	1.40 10 <sup>4</sup>	1.31 10 <sup>30</sup>
4. SiII	1.30 10 <sup>-12</sup>	7.44 10 <sup>7</sup>	3.14 10 <sup>3</sup>	4.49 10 <sup>33</sup>

GW ORIONIS				
line	$F_{obs}$ (erg cm <sup>-2</sup> s <sup>-1</sup> )	$F^*$ (erg cm <sup>-2</sup> s <sup>-1</sup> )	$F^*/F_{\odot}$	EM (cm <sup>-5</sup> )
1. CII	1.50 10 <sup>-13</sup>	9.20 10 <sup>6</sup>	1.39 10 <sup>3</sup>	2.20 10 <sup>28</sup>
2. SiIV	1.40 10 <sup>-13</sup>	7.68 10 <sup>6</sup>	2.13 10 <sup>3</sup>	1.52 10 <sup>30</sup>
3. CIV	2.20 10 <sup>-13</sup>	1.11 10 <sup>7</sup>	1.70 10 <sup>3</sup>	1.58 10 <sup>29</sup>
4. SiII	2.00 10 <sup>-13</sup>	9.27 10 <sup>6</sup>	3.91 10 <sup>2</sup>	5.60 10 <sup>32</sup>

Table 3 - Fluxes and emission measures for some lines in the spectrum of the T Tauri, RU Lupi e GW Orionis stars.

### 2.3 - OBSERVATIONS

From observations in the ultraviolet we can deduce the observed flux,  $F_{obs}$ ; cor-

recting this value for the distance and interstellar absorption we can calculate the flux emitted by the star in each spectral line,  $F^*$ . This is done using

$$F^* = F_{\text{obs}} \left(\frac{d}{R}\right)^2 10^{(0.4A_\lambda)} \quad (14)$$

$$A_\lambda = A_V \left[1 + \frac{1}{3.1} E(\lambda-V)/E(B-V)\right] \quad (15)$$

where

$d$  is the distance of the star,

$A_\lambda$  is the interstellar absorption in magnitude units .

The  $A_\lambda$  values are obtained from the interstellar extinction law defined by Savage e Mathis [17], through linear interpolation of the values  $E(\lambda-V)/E(B-V)$

Table 3 shows the data relative to the stars T Tauri, RU Lupi and GW Orionis. For the distances and radii we have used values extensively quoted in the literature, respectively 160 pc, 150 pc and 500 pc for the distances,  $6R_\odot$ ,  $1.8R_\odot$  and  $8.4R_\odot$  for the radii.

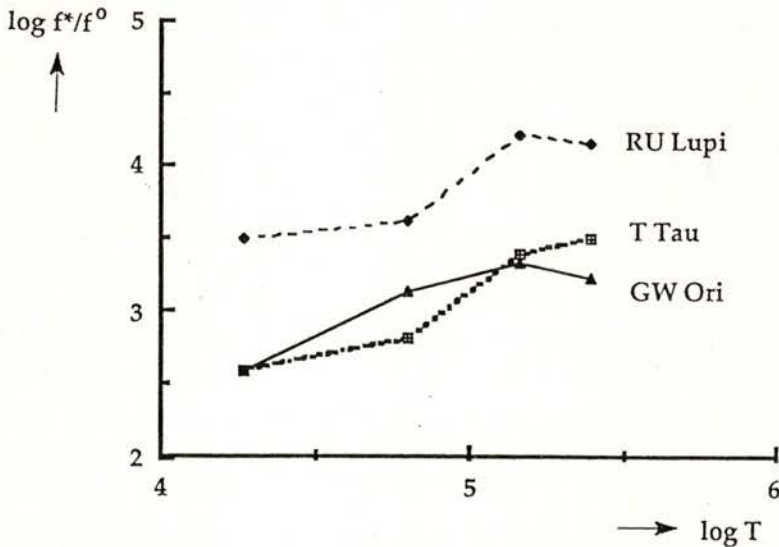


Fig. 2 - Distribution of the energy in the ultraviolet, for the three T Tauri stars. The corresponding emission of the sun is used as unity.

## 2.4 - CONCLUSIONS

Fig. 2 displays the distribution of the emitted energies corresponding to the spectral lines of the sun and of the three T Tauri stars, and summarises the results obtained through the present analysis. It

clearly shows that in the T Tauri stars the energy flux (and consequently the material responsible for its production) coming from the regions with temperature in the interval  $[10^4, 5 \cdot 10^4]$ , is typically  $10^3$  times larger than that of the sun. In other words, the emission

from this so called *transition region*, is highly enhanced in T Tauri stars. On the other hand, there are significant differences amongst the three T Tauri stars regarding not only the amount of energy flux (e.g. RU Lupi and T Tauri) but also its distribution (T Tauri and GW-Orionis). Since some of these stars are similar to, but much younger than the sun (in particular RU Lupi), the results suggest that during evolution towards the main sequence, just a few million years after its formation as a star, the sun might have been the source of a much higher ultraviolet flux than at the present time.

## ACKNOWLEDGMENTS

J.J.F.G.A. Lima acknowledges the award of a grant "Iniciação à Investigação" by JNICT, Proj. 87-27.

## REFERENCES

- [1] Byram, E.T., Chubb, T.A., Friedman, H. and Kupperian, J.E., *The Threshold of Space*, Ed. Zelikoff, M., Pergamon Press, (1957).
- [2] Kupperian, J.E., Boggess, A. and Milligan, J.E., *Astrophys. J.*, **128**, 453 (1958).
- [3] Boggess, A. and Dunkelmann, L., *Astrophys. J.*, **129**, 236 (1959).
- [4] Stecher, T.P. and Milligan, J.E., *Astrophys. J.*, **136**, 1 (1962).
- [5] Morton, D.C. and Spitzer, L., *Astrophys. J.*, **144**, 1 (1966).
- [6] Boksenberg, A., Evans, R.G., Fowler, R.G., Gardner, I.S.K., Housiaux, L., Humphries, C.M., Jamar, C., Macau, D., Malaise, D., Monfils, A., Nandy, K., Thompson, G.I., Wilson, R. and Wroe, H., *Mon. Not. R. astr. Soc.*, **163**, 291 (1973).
- [7] Hoekstra, R., Van der Hucht, K.A., de Jager, C., Kamperman, T.M., Lamers, H.J., Hammerschlag, A. and Werner, W., *Nature*, **236**, 121 (1972).
- [8] Canuto, V.M., Levine, J.S., Augustsson, T.R. and Imhoff, C.L., *Nature*, **296**, 816 (1982).
- [9] Canuto, V.M., Levine, J.S., Augustsson, T.R., Imhoff, C.L. and Giampapa, M.S., *Nature*, **305**, 281 (1983).
- [10] Lago, M.T.V.T., Penston, M.V. and Johnstone, R., *Proceedings of 4th European IUE Conference, ESA SP-218*, 233 (1984).
- [11] Pottasch, S.R., *Astrophys. J.*, **137**, 945 (1963).
- [12] Judge, P.G., *Mon. Not. R. astr. Soc.*, **221**, 119 (1986).
- [13] Johnstone, R.M., Ph.D. Thesis, University of Sussex (1985).
- [14] Brown, A., Ferraz, M.C.M. and Jordan, C., *Mon. Not. R. astr. Soc.*, **207**, 831 (1984).
- [15] Osterbrock, D.E., *Astrophys. of Gaseous Nebulae* Freeman, San Francisco (1974).
- [16] Brown, A., and Jordan, C., (1981) *Mon. Not. R. astr. Soc.*, **196**, 757 (1981).
- [17] Savage, B.D. and Mathis, J.S., *Ann. Rev. of Astr. and Astrophys.*, **17**, 73 (1979).

## CONTENTS

<b>ENHANCED NUCLEAR MAGNETISM</b>	1
B. BLEANEY	
<b>THE PROBLEM OF SPURIOUS COLOR BOUND STATES IN NAMBU JONASINIO TYPE LAGRANGIANS *</b>	15
ALEX H. BLIN, BRIGITTE HILLER AND JOÃO DA PROVIDÊNCIA	
<b>STRUCTURE AND PHYSICAL PROPERTIES OF THE QUATERNARY PHASE "CAALSIFER" IN INDUSTRIAL Fe-Si ALLOYS</b>	21
F. MARGARIDO <sup>1</sup> , M. O. FIGUEIREDO <sup>2</sup>	
<b>ELECTRON DENSITY STUDIES IN THE LAVES PHASE FeBe<sub>2</sub></b>	31
M.M.R. COSTA, M.J.M. DE ALMEIDA AND J.A. PAIXÃO	
<b>ON THE QUANTUM HARMONIC OSCILLATOR WITH TIME-DEPENDENT FREQUENCY</b>	39
FRANCISCO M. FERNÁNDEZ AND EDUARDO A. CASTRO	
<b>ULTRAVIOLET EMISSION AND SPECTRA FOR T TAURI STARS</b>	44
JOÃO J. F. G. AFONSO LIMA AND MARIA TERESA VAZ TORRÃO LAGO	







# SOCIEDADE PORTUGUESA DE FÍSICA

AV. REPÚBLICA, 37 - 4.º • 1000 LISBOA • PORTUGAL

PORTUGALIAE PHYSICA publishes articles or research notes with original results in theoretical, experimental or applied physics; invited review articles may also be included.

Manuscripts, with an abstract, may be written in English or French; they should be typewritten with two spaces and in duplicate. Figures or photographs must be presented in separate sheets and be suitable for reproduction with eventual reduction in size; captions should make the figures intelligible without reference to the text. Authors are requested to comply with the accepted codes concerning references.

There is page charge. Author(s) will get 50 free reprints (without covers); these are to be shared among all the authors of the article. Authors interested in more reprints should say so when sending their manuscripts; quotations shall be sent with the proofs.

Subscription rates for volume 21:

3.600 Escudos (US\$24) — individuals

9.000 Escudos (US\$60) — libraries

PORTUGALIAE PHYSICA may also be sent on an exchange basis; we welcome all suggestions to such effect.

All mail to be addressed to

PORTUGALIAE PHYSICA

C/O LABORATÓRIO DE FÍSICA, FACULDADE DE CIÊNCIAS

PRAÇA GOMES TEIXEIRA

4000 PORTO - PORTUGAL

# PORTUGALIAE PHYSICA

VOL. 21 • NUMB 1/2 • 1992

## CONTENTS

### *Enhanced nuclear magnetism*

B. Bleaney ..... 1

### *The problem of spurious color bound states in Nambu Jona-Lasinio type lagrangians*

Alex H. Blin, Brigitte Hiller and João da Providência ..... 15

### *Structure and physical properties of the quaternary phase «Caalsifer» in industrial Fe-Si Alloys*

F. Margarido and M. O. Figueiredo ..... 21

### *Electron density studies in the laves phase FeBe<sub>2</sub>*

M. M. R. Costa, M. J. M. de Almeida and J. A. Paixão ..... 31

### *On the quantum harmonic oscillator with time-dependent frequency*

Francisco M. Fernández and Eduardo A. Castro ..... 39

### *The emission measure and ultraviolet spectra of T Tauri stars*

João J. F. G. Afonso Lima and Maria Teresa Vaz Torrão Lago ..... 44

# PORTUGALIAE PHYSICA

VOLUME 21

FASC. 3/4

1992

SOCIEDADE PORTUGUESA DE FÍSICA

## PORTUGALIAE PHYSICA

Fundada em 1943 por A. Cyrillo Soares, M. Telles Antunes, A. Marques da Silva e M. Valadares

### *Director*

J. M. Machado da Silva (Faculdade de Ciências, Universidade do Porto)

### *Co-Directores*

M. Salete Leite (Faculdade de Ciências, Universidade de Coimbra)  
Alexandre Quintanilha (ICBAS, Universidade do Porto)

### *Directores-Adjuntos*

Olivério Soares (Faculdade de Ciências, Universidade do Porto)  
Maria Helena Vaz de Carvalho Nazaré (Universidade de Aveiro)  
Teresa Mora (Universidad Autónoma de Barcelona)  
Margarida Costa (Universidade de Coimbra)  
J. Bartolomé (Universidad de Zaragoza)

### *Comissão Redactorial*

B. Barbara (Laboratório Louis Néel, CNRS — Grenoble)  
Kim Carneiro (Instituto Dinamarquês de Metrologia. Lyngby)  
F. Bragança Gil (Faculdade de Ciências, Universidade de Lisboa)  
I. R. Harris (Departamento de Metalurgia, Universidade de Birmingham)  
M. Salete Leite (Faculdade de Ciências, Universidade de Coimbra)  
N. Miura (Instituto de Física do Estado Sólido, Universidade de Tokyo)  
M. Ida (Faculdade de Ciências, Universidade de Kobe)  
F. D. Santos (Faculdade de Ciências, Universidade de Lisboa)  
J. M. Machado da Silva (Faculdade de Ciências, Universidade do Porto)  
J. B. Sousa (Faculdade de Ciências, Universidade do Porto)  
R. Stinchcombe (Departamento de Física Teórica, Universidade de Oxford)  
M. Velarde (Faculdade de Ciências, UNED — Madrid)  
J. P. Burger (Université de Paris, Orsay)  
F. R. N. Nabarro (University of Witwatersrand, Johannesburg)

### *Anteriores Directores*

A. Cyrillo Soares (1943-1949), A. Monteiro (1951-1954)  
A. da Silveira (1965-1975), J. M. Araújo (1979-1986)

# PORTUGALIAE PHYSICA

VOLUME 21

FASC. 3/4

1992

SOCIEDADE PORTUGUESA DE FÍSICA



# PROCEEDINGS

«FÍSICA 92» CONFERENCE (Invited talks)

Vila Real - Portugal • September 1992



## GASEOUS DETECTORS IN ASTROPHYSICS, MEDICINE AND BIOLOGY

FABIO SAULI

CERN, Geneva, Switzerland

**ABSTRACT** - Fast, position sensitive gaseous detectors have been developed mostly to satisfy the needs of elementary particle physics experimentation. We present some examples of use of those devices in other applied fields, from astrophysics to biology and medical research.

### 1. INTRODUCTION

Ionization chambers, proportional and Geiger counters have been in use for decades for detection of radiation. Large area, fast position-sensitive gaseous detectors based on the Multiwire Proportional Chamber (MWPC) [1] have been developed, primarily to satisfy the stringent demands encountered in particle experimental physics. Rather complex instruments, and therefore requiring dedicated operators, MWPCs and their offsprings represent in many cases unique tools for detection and localization of radiation; the continuing efforts to increase the ruggedness and reliability of the devices and the introduction of performing wireless detectors (parallel plate and microstrip gas chambers) permit to foresee an increasing use of gaseous detectors in other applied fields. This paper describes some examples of use of gaseous devices in medicine, biology and astrophysics.

### 2. APPLICATIONS OF MWPC

In a standard MWPC (see Fig. 1), electrons released by ionization in the gas are multiplied in the high electric field around thin wires. Various methods can be used to achieve localization: detection of pulses over threshold on anode wires, measurement of the center of gravity of signals induced by the avalanches on cathode strips, coupling of the signals to an external delay line, measurement of the collection or drift time of charges.

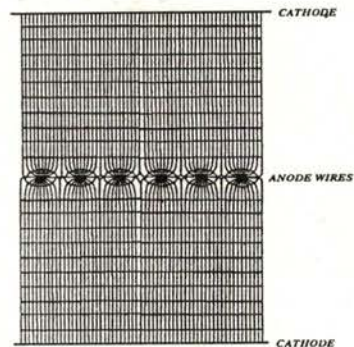


Fig. 1: Schematics of the Multiwire Proportional Chamber, showing the electric field lines and equipotentials.

Each method has advantages and drawbacks, and the choice is therefore application-specific.

In medicine and biology, a widely used readout method makes use of delay lines, that transform the space coordinate of the induced signals on cathodes into

time delays, the signal detected on the anode wire plane being used to provide the reference time. The rate limitations and single hit capability of such readout method are compensated by the great simplicity and low cost.

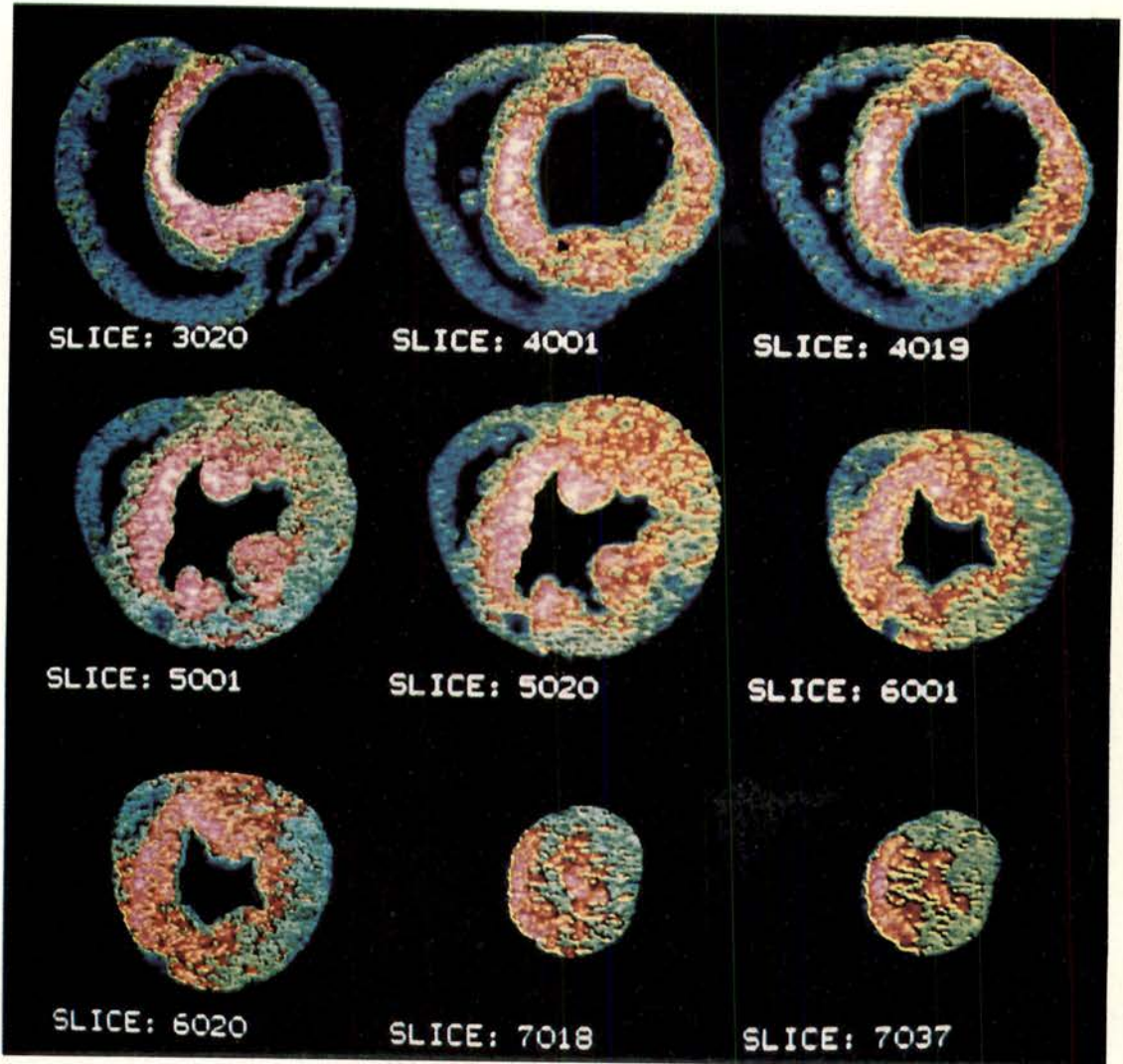


Fig. 2: Activity distribution in a slice of a dog's heart is recorded following repeated stimulation of specific cardio-pulmonary nerves after injection of triziated deoxyglucose.

Fig. 2 shows the beta activity distribution recorded with a MWPC with delay line readout in anatomical samples (slices of a dog's heart) labelled with tritiated deoxyglucose [2]. The experiment aims at studying the regional uptake of sugars in the heart under different stimulation conditions. Animals are open-chested after anesthesia, and se-

lected efferent axons of cardiopulmonary nerves stimulated after injection of tritiated deoxyglucose. After excision, the distribution of the labeller is detected with the chamber and compared to normal distributions. Several hundred preparations can be analyzed in relative short times as compared to the use of photographic methods.

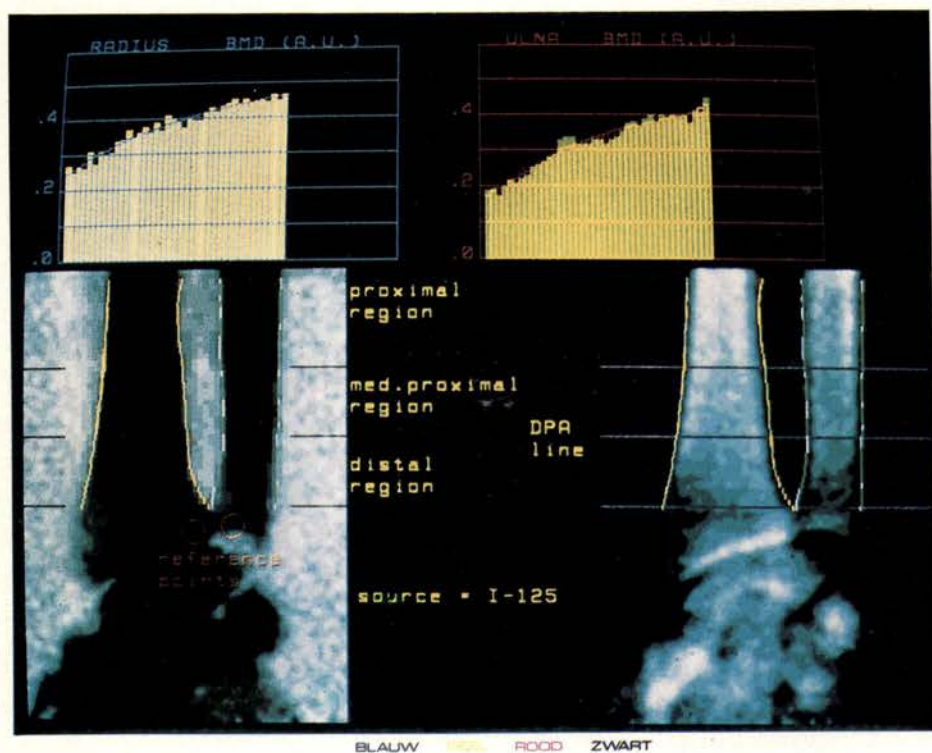


Fig. 3: Transmission radiography of limbs realized with a MWPC, showing examples of bone mineral content computed along selected directions.

With a similar apparatus, optimized for the detection of x rays in the range between 20 and 60 KeV, the same group has demonstrated the superior qualities of digital methods over photography in the clinical measurement of bone

mineral content in the peripheral skeleton [3]. A pressurized (3 bars) xenon-filled MWPC with delay line readout is used to detect and localize the photons at rates up to few hundred kHz. Single photon absorption (SPA) transmission

images are obtained using radioactive sources emitting photons at 27.4 KeV ( $^{125}\text{I}$ ) and 42 KeV ( $^{153}\text{Gd}$ ) (Fig. 3); the limb to be imaged is immersed in water, and the contribution of soft tissues can be subtracted making a transmission image of the bolus alone. In

Double Photon Absorption (DPA), the soft tissue contribution is cancelled recording two images at different energies (27.4 KeV from  $^{125}\text{I}$  and 60 KeV from  $^{241}\text{Am}$ ) and logarithmically subtracting the two after weighting.

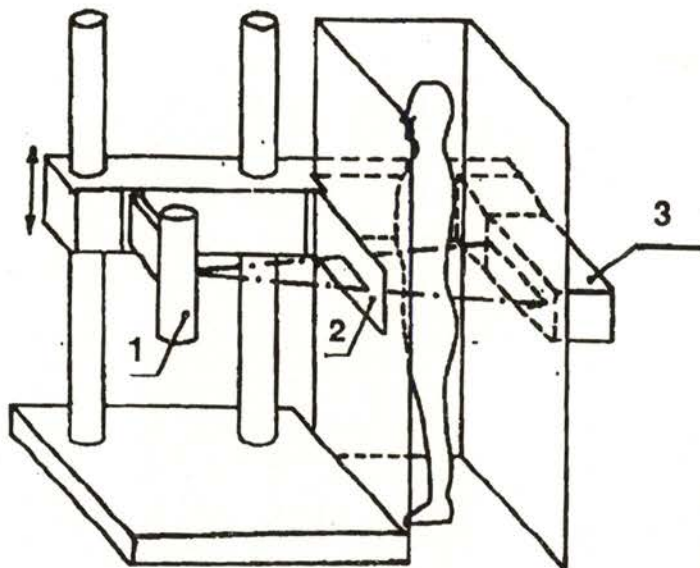


Fig. 4: Scanning system for transmission radiography using a high rate digital MWPC.

MWPC of conventional design are limited in their use to moderate acquisition rates, several hundred kHz or so over the whole detector, mostly because of the time necessary for transferring and recording the coordinate information. A simple counting of the hits on a wire can be done at much higher rates, but does not provide two-dimensional localization in conventional MWPC. A rather ingenious geometrical construction has been used to fully profit from the high intrinsic rate capability of the gas detectors for x-ray transmission radiography [4] (see Fig. 4).

The object is exposed to a beam of x rays emitted from a point source; the position detector, a pressurized xenon MWPC, is built with a particular geometry having non-parallel anode wires pointing to the source. To compensate for the variable distance between anodes, affecting the gas gain, the anode to cathode distance is increased along the wires. All x-rays with the same angle are therefore detected by the same wire, and the counting rate on wires provides the absorption profile in the slice. Successive slices are obtained scanning through the body with the generator-detector system.

The system can acquire data at a rate in excess of 300 kHz per wire, with a position accuracy around 0.8 mm fwhm. Fig. 5 shows an example of transmission digital radiography of the chest obtained

with the described apparatus in clinical conditions. The very low exposure dose (few mREM skin value) allows to foresee the use of the device in radiation-sensitive areas of the body.

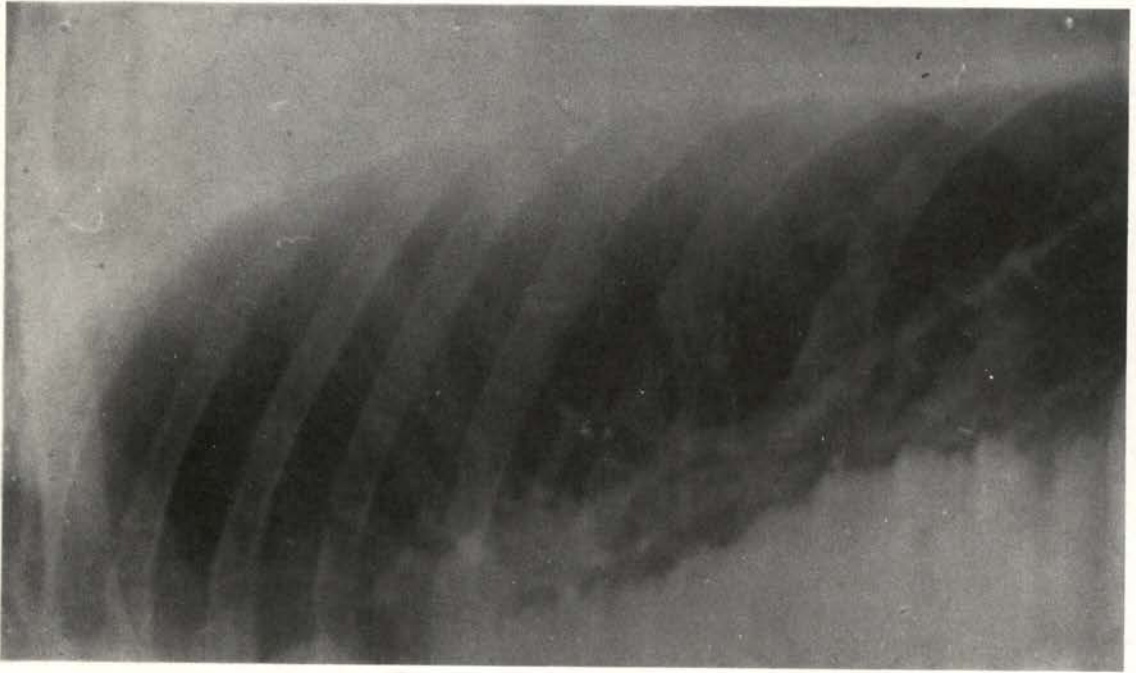


Fig. 5: Absorption radiography of the chest obtained with the high rate digital MWPC.

An example of direct use in astrophysics of technologies developed originally in high energy physics is given by the Cosmic Ray Tracking project, aimed at detection of extended air showers produced in the upper atmosphere by energetic photons [5]. The basic element of detection is shown in Fig. 6: it consists of a pair of large volume drift chambers separated by an iron plate-scintillator

sandwich used for triggering and as muon filter. Tracking is realized measuring the drift time on anode wires and the induced signals on arrays of cathode pads in the central wire plane; muon identification is obtained by comparison of the tracks measured before and after the muon filter (electrons will either be absorbed or generate an electromagnetic shower).

Fig. 7 shows an example of cosmic shower detected recording the time profile of signals detected on six adjacent wires. The project foresees the installation of around 400 detector modules arranged in concentric rings and covering an area of about  $3.10^5$  square meters; thanks to the two-track resolu-

tion of a few mm, as compared to centimeters in existing scintillation counters arrays, the detector improves sensitivity to extended air showers by two orders of magnitude in energy downwards, from  $10^{14}$  to  $10^{12}$  eV for the incoming photon.

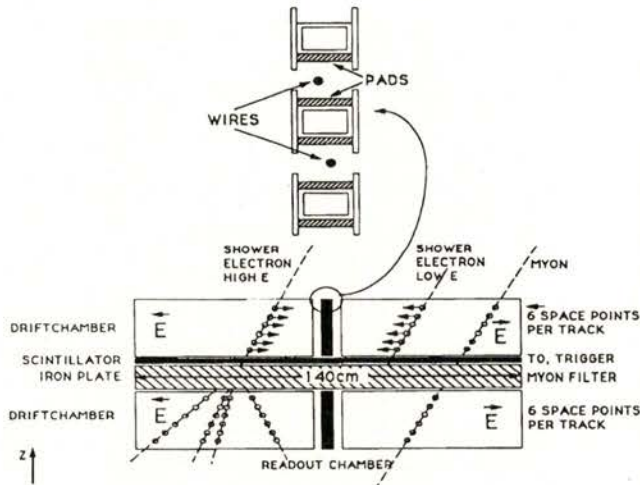


Fig. 6: Detector module for the cosmic ray tracking project. It consists of two independent chambers separated by a muon filter and scintillator.

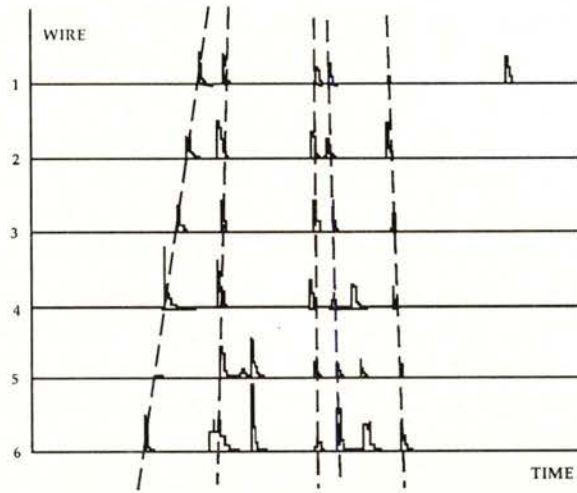


Fig. 7: A cosmic shower recorded by six drift wires equipped with flash analogue-to-digital converters.

### 3. THE IMAGING CHAMBER

Charge multiplication is exploited in gaseous counters for amplification of the ionization signal; photons are also

copiously emitted in the avalanche as a result of molecular excitation and recombination processes. In imaging chambers, one detects and visualizes the emitted photons.

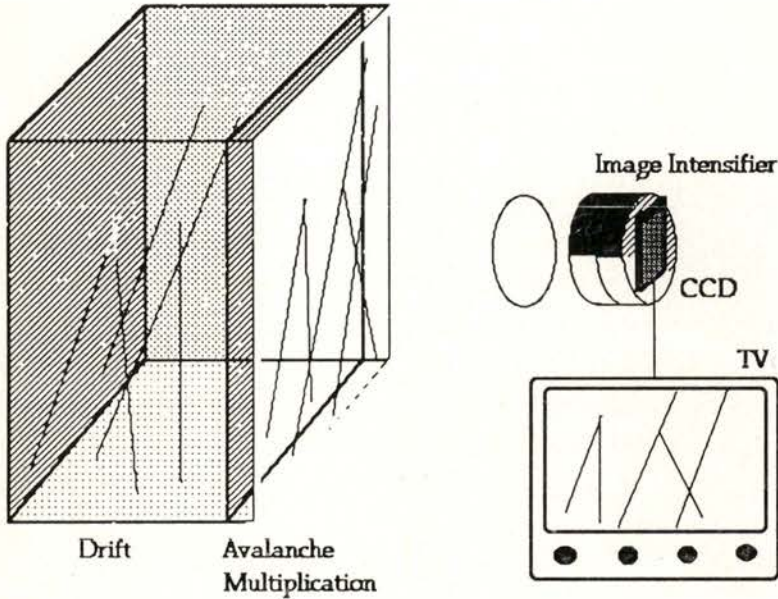


Fig. 8: Schematics of the imaging chamber. Electrons released in the gas volume drift to the parallel plate avalanche chamber. Photons emitted by the avalanches are detected by an image intensifier coupled to a solid state camera.

Addition of low ionization threshold vapors such as TEA\* and TMAE<sup>+</sup>, together with the use of a parallel plate geometry (as against a MWPC structure), largely enhance the emission in a spectral region convenient for optical detection [6]. The structure of an Optical Imaging Chamber (OIC) is

\* TEA: Triethylamine,  $(C_2H_5)_3N$

+ TMAE: Tetrakis (dimethylamine) ethylene  
 $[(CH_3)_2N]_2C = C[N(CH_3)_2]_2$

shown schematically in Fig. 8; electrons released in a gas by ionizing radiation drift under the influence of an electric field towards a region of very high field between two semi-transparent grids. During the avalanche development, photons are emitted and detected through a suitable window. An image intensifier is used to amplify the signal to a level compatible with the sensitivity of a solid state camera; the image can be

recorded directly or after digitization. To obtain high gains, one can use instead of a single amplification gap a multistep avalanche chamber ; to better tune the spectral emission to the sensitivity of the photon detector a thin foil wavelength shifter can be mounted in contact with the last electrode [7].

The simplicity and the high granularity of the device has suggested the application of the OIC in fields where these performances largely compensate for the

modest data acquisition rate obtainable. An example is the visual detection in real time of cosmic rays is shown in Fig. 9. A device of this kind is operated at the Universal Exhibition in Sevilla to illustrate technological developments at CERN; a similar detector, installed at the CERN permanent exhibition "Microcosm", allows direct visualization of tracks produced by 5 MeV alpha particles .



Fig. 9: An example of cosmic activity recorded in a single frame with the video digitizer.

Use of the imaging chamber is being considered for an experiment aimed at detection of weakly interacting massive particles (WIMPs) [8]. The apparatus consists in a large volume of gas where recoil protons ejected off hydrogen or methane can be detected through amplification of the ionization trail in a geometry like the one shown in Fig. 8. To

obtain measurable ranges for the low energy recoil protons (few KeV), the detector is operated at low pressures; in order to decrease the dispersing effect of diffusion on the drifting electrons, particularly large at low pressures, the device is operated in a strong magnetic field parallel to the drift direction. Simulations show that a distribution of

the end point of the recorded tracks, compensated for the daily rotation of earth, should be able to pinpoint galactic sources of the hypothetical WIMPs with a good degree of confidence. One can

foresee the use of the imaging chamber in other astrophysics applications, for example in the detection of extended air showers generated by energetic gamma rays, described in the previous section.

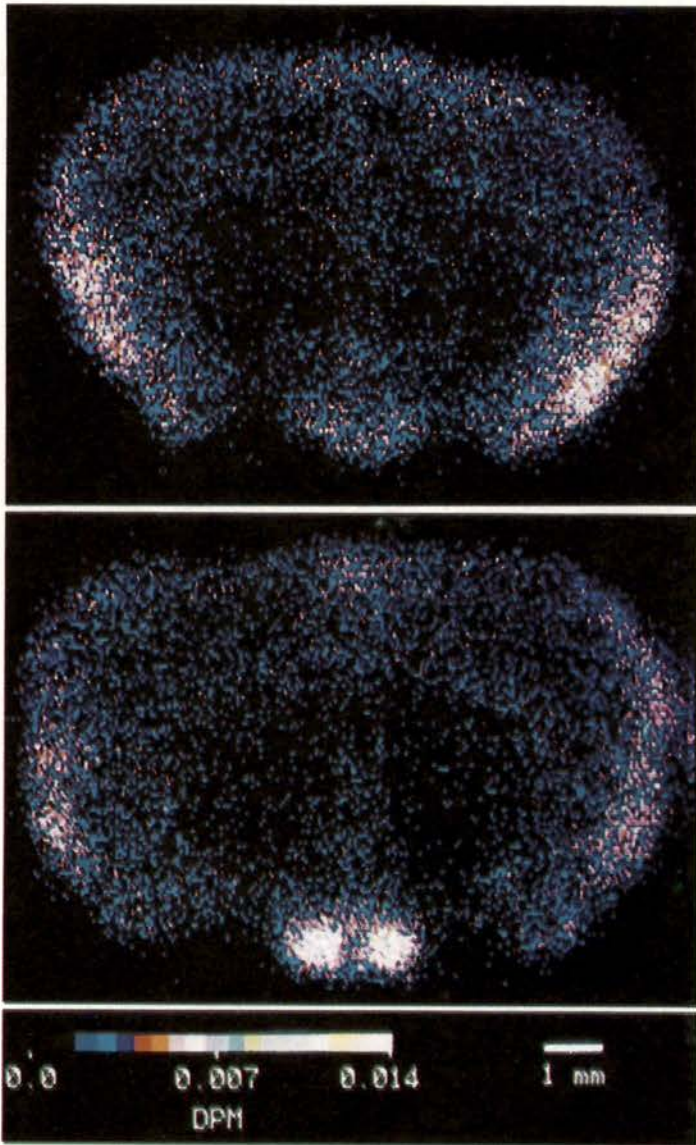


Fig. 10: Activity distribution in brain slices of male and female rats labelled with tritiated vasopressin (real size about 10 by 5 mm<sup>2</sup>).

The OIC is being used in biology to map the two-dimensional activity distribution in anatomical samples marked with radioactive labellers [9]. Fig. 10 shows examples of activity distributions in anatomical samples (brain slices of male and female rats labelled with tritiated vasopressin\*) recorded with the imaging chamber [10]; the study aims at establishing the effects of hormones release at the early stages of development on the sex of mature animals. Due to the sensitivity to individual radioactive decays, comparable contrasts are obtained with exposure times one or two order of magnitude shorter with the gaseous device as compared to film. This obviously allows the realization of exposure-intensive studies. Another advantage of the gas detector over conventional contact auto-radiography with is the linearity of the response over an extended range of activity, see Fig. 11 [10]; this allows quantitative analysis in a single exposure.

#### 4. Microstrip Gas Chambers

This recently introduced gaseous detector [11] allows to overcome some restrictions met in classic multiwire structures, in particular the resolution and rate limitations resulting from the practical minimum wire pitch (a mm or so). As shown in Fig. 12, a Gas Microstrip Chamber (GMSC) consists in a set of

thin parallel metal strips on an insulating substratum, alternately connected as anode and cathode; an upper electrode defines the sensitive volume of the chamber. Electrons released in the gas drift to the anode strips, where the high electric field induces avalanche multiplication as in a wire counter; a potential applied to the back plane prevents the collection of ions on the insulating substratum and minimizes gain-perturbing charging up processes.

The GMSC allows to reach gas gains around  $10^4$  with remarkably good energy resolutions (12% fwhm for the 5.9 keV x-rays [12]). The fast collection of most of the ions produced in the avalanche by the neighboring cathode strips imply also a very high rate capability, close to a MHz/mm<sup>2</sup> [13].

Several schemes can be used to readout the space coordinates of the detected radiation in the GMSC. A simple amplifier-discriminator on each anode strip will provide an accuracy corresponding to the pitch, while recording the profile of induced charge on cathode strips allows to get an accuracy of 30  $\mu$ m rms for minimum ionizing particles [12]. A charge division readout method has been developed for the x-ray detector of the Soviet-Danish Röntgen Telescope, SO-DART, (Fig. 13 [14]). Groups of cathode strips are connected through a resistive chain, with readout amplifiers in discrete positions. The second coordinate is provided by a similar system mounted on an induction grid above the amplifying structure.

\* AVP, [<sup>3</sup>H] vasopressin

Although limited to moderate rates, the scheme allows to reduce the number of electronics channels to a minimum, a stringent requirement for space applications. Operating the detector with a xenon-CH<sub>4</sub> mixture, the authors have

demonstrated a position resolution around 340  $\mu\text{m}$  rms for 5.9 keV x-rays; in two separate detectors optimized to cover the low and the high energy x-ray region respectively, the energy spectra shown in Fig. 14 a) and b) have been obtained.

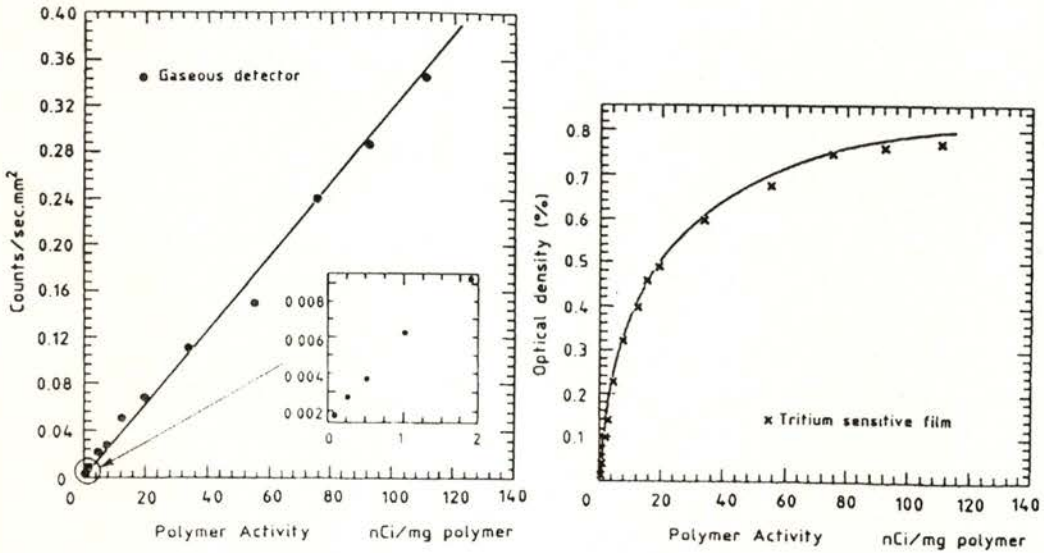


Fig. 11: Response of the imaging chamber (left) and of conventional film autoradiography to increasing activities of a tritiated polymer standard.

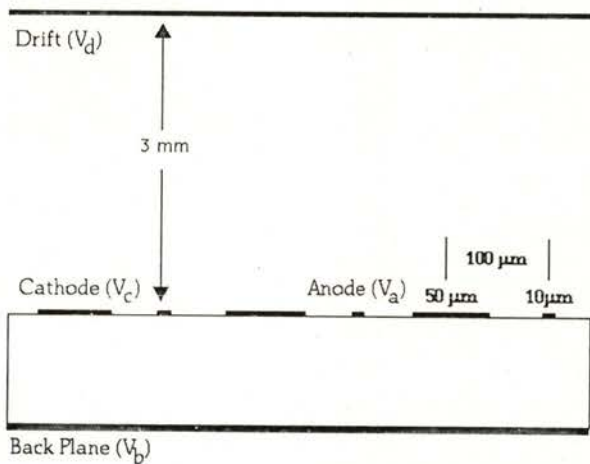


Fig. 12: Schematics of the microstrip gas chamber.

Use of the MSGC as detector for x-ray transmission radiography is also appealing because of the very high rate capability of the device. It has been recently demonstrated that MSGC can reliably

operate in xenon mixtures at pressures up to 6 bars, a necessary requirement for obtaining efficient detection of x-rays at the energies used for clinical applications [15].

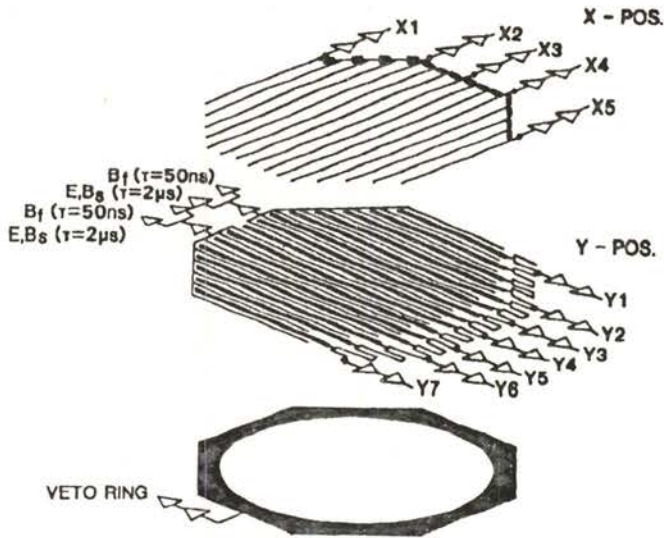


Fig. 13: Schematics of the charge division system foreseen for the readout of a MSGC used in the soviet-danish Röntgen telescope (SODART).

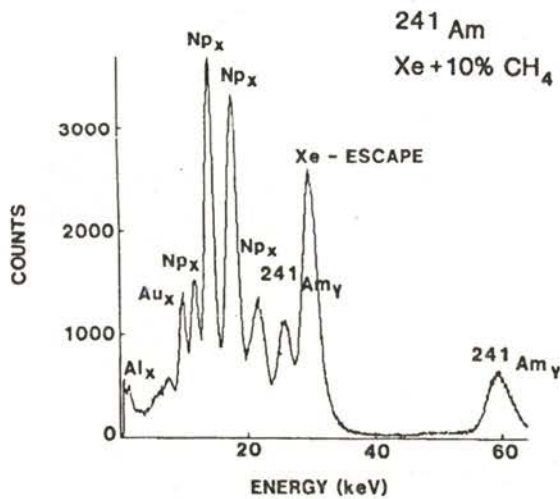


Fig. 14: Energy resolution of the MSGC built for SODART in the high energy x-ray region.

## REFERENCES

- [1] G. Charpak, *Ann. Rev. Nuclear Sci.* **20** 195 (1970).
- [2] M. G. Trivella, J.A. Armour, M. Dalle Vacche, C. Paoli, R. Porinelli, R. Bellazzini, G. Pelosi, P. Camici, L. Taddei, G. A. Klassen and A. L'Abbate, *Cardiovascular Research* (1992).
- [3] F. Angelini, R. Bellazzini, A. Brez, M.M. Massai, M. R. Torquati, G. Perri, D. Trippi, F. Beghé, *Investigative Radiology* **24** 684 (1989).
- [4] S.E. Baru, A.G. Khabakhpashev, L.I. Shekhtman, *Nucl. Instr. Methods* **A283** 431 (1989).
- [5] M. Feuerstack, J. Heinze, P. Lennert, B. Müller, S. Polenz, B. Cshmidt, J. Spizer, B. Stadler, S. Gamp, W. Hofmann, T. Kihm, J. Knöppler, M. Panter, B. Povh, C. Wiedner, *Nucl. Instr. Methods* **A310** 287 (1991).
- [6] G. Charpak, J.-P. Fabre, F. Sauli, M. Suzuki and W. Dominik, *Nucl. Instr. Methods* **A258** 177 (1987).
- [7] R. Bouclier, M. Bourdinaud, G. Charpak, P. Fonte, G. Million, F. Sauli and D. Sauvage, *Nucl. Instr. Methods* **A300** 286 (1991).
- [8] K. Buckland, M. Lehner, G. Masek, M. Mojaver, *Optical Readout of Prototype TPC WIMP Detector*, Int. Rep. Univ. of California San Diego (Jan. 1992).
- [9] W. Dominik, N. Zaganidis, P. Astier, G. Charpak, J.C. Santiard, F. Sauli, E. Tribollet, A. Geissbühler and D. Townsend, *Nucl. Instr. Methods* **A278** 779 (1989).
- [10] E. Tribollet, J.J. Dreifuss, G. Charpak, W. Dominik and N. Zaganidis, *Proc. Nat. Acad. Sci. USA* **88** 1466 (1991).
- [11] A. Oed, P. Convert, M. Berneron, H. Junk, C. Budtz-Jørgensen, M.M. Madsen, P. Jonasson, H.W. Schnopper, *Nucl. Instr. Methods* **A284** 223 (1989).
- [12] F. Angelini, R. Bellazzini, A. Brez, M.M. Massai, G. Spandre, M. Torquati, R. Bouclier, J. Gaudaen and F. Sauli, *Nucl. Phys.* **23A** 254 (1991).
- [13] R. Bouclier, J.J. Florent, J. Gaudaen, G. Million, A. Pasta, L. Ropelewski, F. Sauli and L.I. Shekhtman, *Proc. Int. Vienna Wire Chamber Conf.* 1992.
- [14] C. Budtz-Jørgensen, A. Bahnsen, C. Olesen, M.M. Madsen, P. Jonasson, H.W. Schnopper, A. Oed, *Nucl. Instr. Methods* **A310** 82 (1991).
- [15] F. Angelini, R. Bellazzini, A. Brez, M.M. Massai, L. Shekhtman, G. Spandre and M.R. Torquati, *Proc. Int. Vienna Wire Chamber Conf.* 1992.



# MAIN PROPERTIES OF THE NEW HIGH $T_C$ SUPERCONDUCTORS RELATED TO THERMODYNAMIC FLUCTUATIONS AND TO THE MAGNETISM OF COPPER.

J. P. BURGER

Laboratoire Physique des Solides E.S.P.C.I. 10, rue Vauquelin, 75231 Paris Cedex 05

**ABSTRACT** - After a short analysis of classical superconductors, we discuss the atomic and electronic structure of the new superconductors. A strong atomic anisotropy with two-dimensional character can lead to thermodynamic fluctuations of the superconducting order parameter which do not favour the  $T_C$  value nor the superconducting properties. For the classical low- $T_C$  superconductors there was always a strong decrease of  $T_C$  due to magnetic impurities; this occurs much less for these new high- $T_C$  superconductors with Gd, Fe, Ni, impurities. The existence of antiferromagnetic (AF) Copper in the fundamental superconducting Copper-oxygen planes seems to favour this new type of superconductivity. The substitution of  $Cu^{++}$  by non-magnetic  $Zn^{++}$  lowers  $T_C$  very significantly. For that reason one can consider that the two dimensional (2D) AF of  $Cu^{++}$  can be at the origin of these new superconductors that have a much higher  $T_C$ . We will present some theoretical models on the correlation between this magnetism and the superconductivity. A fundamental result is that  $T_C$  disappears when the 2D AF disappears, even when the electrical conductivity becomes much larger.

## I - INTRODUCTION

1 - The classical superconductors with  $T_C \leq 23$  K.

The origin of this superconductivity was well explained by the BCS theory [1] that described the formation of conducting Cooper pairs due to an attractive interaction induced by the electron-phonon interaction with

$$T_C = 1.14 \theta_D \exp\left(-\frac{1}{g}\right)$$
$$g = \lambda - \mu^* \quad (1)$$

( $\theta_D$  is the Debye temperature,  $\lambda$  is the attractive interaction parameter while

$\mu^*$  corresponds to a repulsive Coulomb interaction between conduction electrons; of course the occurrence of superconductivity is related to  $\lambda > \mu^*$ ).

Three problems of these classical superconductors may concern also the new superconductors:

-  $T_C$  goes always to zero for thin films i.e. for two dimensional (2D) systems,  $T_C$  is suppressed by thermodynamic fluctuations.

- For bulk materials  $T_C$  is strongly decreased by very low concentrations of magnetic impurities, a fact related to the destruction of Cooper pairs when a magnetic exchange interaction exists between the impurity spins and the two spins of the Cooper pairs of opposite

signs. The decrease in  $T_C$  can be well explained by the Ginzburg-Landau model i.e.:

$$\Delta F_S + F_{MS} = -\alpha \Psi^2 + \frac{\beta}{2} \Psi^4 + \gamma \Psi^2 \langle \delta M^2 \rangle. \quad (2)$$

Here  $\Delta F_S = F_S - F_N$  is the free energy difference between the superconducting and normal states,  $\Psi^2$  is the superconducting order parameter while  $\alpha = \alpha_0(T_C - T)$ .

Furthermore  $F_{MS}$  is related to the exchange interaction  $J$  between the Cooper pair spins and the localized impurity spins with  $\gamma \equiv J^2$  while  $\langle \delta M^2 \rangle$

$= 2 \chi k_B T$  is the thermodynamic fluctuation of the impurity magnetization ( $\chi$  is the paramagnetic susceptibility). The minimization of  $\Delta F_S + F_{MS}$  leads to

$$T_C(\gamma) = T_C - \frac{\gamma}{\alpha_0} \langle \delta M^2 \rangle \quad (3)$$

Most of the  $T_C$  values are suppressed by less than 1% of magnetic impurities. For ferromagnetic transitions below  $T_C(\gamma)$ , this  $T_C(\gamma)$  also disappears; this is not entirely if an antiferromagnetic (AF) transition occurs.

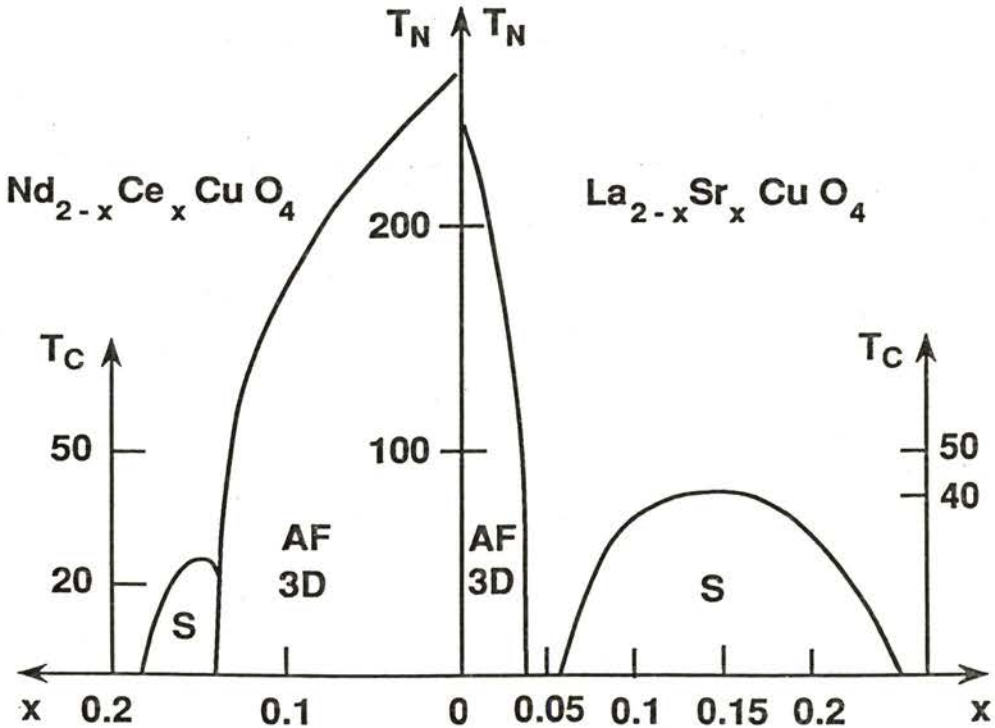


Fig 1:  $x$  dependence, related to the conduction carrier density, of the magnetic and superconducting transition temperatures  $T_N$ ,  $T_C$  for  $La_{2-x}Sr_xCuO_4$  and  $Nd_{2-x}Ce_xCuO_4$ .

- A further problem which can be important for the new superconductors, concerns the situation where two superconducting films of thickness  $d_S$  are separated but in contact with an intermediate normal metallic or even insulating film of thickness  $d_N$ : a weak superconducting order parameter can be induced in this intermediate film by the so called proximity or Josephson effects; it leads also to a decrease in  $T_C$  that will depend on the values of  $d_S$  and  $d_N$ .

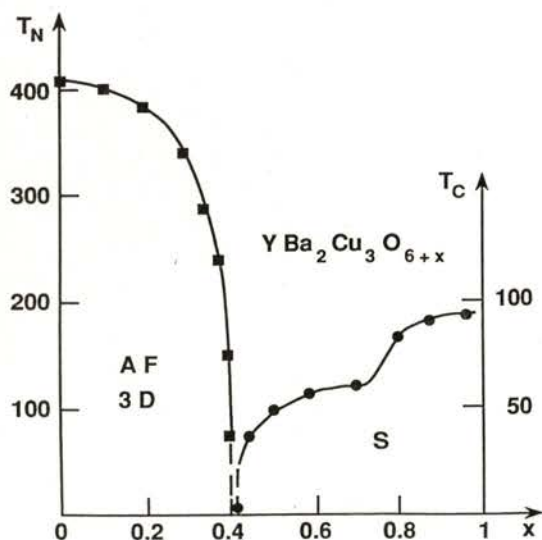


Fig 2.  $x$  dependence, related to the conduction carrier density, of the magnetic and superconducting transition temperatures of the 123 compounds

2 - The new high- $T_C$  superconductors.

a) - The new copper oxide compounds. There are mainly four types of materials [2]:

-  $\text{La}_{2-x}\text{Sr}_x\text{CuO}_4$  ( $T_C \leq 39$  K) and  $\text{Nd}_{2-x}\text{Ce}_x\text{CuO}_4$  ( $T_C \leq 42$  K); for  $x = 0$  we have insulators with AF transitions of copper. The three dimension (3D) AF disappears when  $x \geq 0.03$  while superconductivity appears for  $x \geq 0.07$  (Fig 1);  $T_C(x)$  increases as a function of  $x$  up to  $x \approx 0.15$  and then decreases to zero for  $x \approx 0.25$ .

- the 123 compounds  $\text{YBa}_2\text{Cu}_3\text{O}_{6+x}$  ( $T_C \leq 93$  K) which are also insulators with (3D) AF for  $x = 0$ ;  $T_C(x)$  appears and increases beyond  $x \geq 0.4$  up to  $x = 0.6$  with a second increase up to  $x \approx 0.9$  (Fig. 2) while the (3D) AF disappears near  $x \approx 0.40$ .

- the 2201, 2212 and 2223 compounds of Bi and Tl i.e.  $\text{Bi}_2\text{Sr}_2\text{Ca}_{n-1}\text{Cu}_n\text{O}_{2n+4}$  and  $\text{Tl}_2\text{Ba}_2\text{Ca}_{n-1}\text{Cu}_n\text{O}_{2n+4}$  with  $n = 1, 2, 3$ .  $T_C$  is maximum for  $n=3$ , and reaches 110 K for the Tl compounds. As a function of oxygen concentration,  $T_C$  goes through a maximum at  $2n+4$ , a situation similar to the first compound (see Fig 1).

b) - Atomic structure effects: a very particular situation arises related to the fundamental  $\text{CuO}_2$  planes. For  $\text{La}_{2-x}\text{Sr}_x\text{CuO}_4$  and the 2201 compounds there is one  $\text{CuO}_2$  plane per unit cell while for the 123 and 2212 compounds there are two and for the 2223 compounds there are three such planes per unit cell (Fig. 3). But inside the unit cell we can distinguish less metallic and less superconducting planes (Fig. 3). For that reason along the axis perpendicular to the  $a, b$  axis of the planes there can be proximity or Josephson effects for the less superconducting

planes but also more important thermodynamic fluctuations for the fundamental superconducting  $\text{CuO}_2$  planes. There is also a large ratio between the two electrical resistivities  $\rho_c$  and  $\rho_{ab}$  [3] which clearly indicates the large anisotropy of the atomic and electronic structures.

c) - Electronic structure effects. Here we have two fundamental models.

- By considering that these compounds are ordinary metals [4] [5] (with  $U < T$ , where  $U$  corresponds to the Coulomb energy for two electrons on the same atom while  $T$  corresponds to the conduction band width) one can relate

the conduction band to the  $\text{Cu}^{++} = 3d^9$  state or to antibonding and bonding bands due to the oxygen-copper hybridization. For such a half filled band with a 2D atomic structure, the Fermi surface corresponds exactly to a square which leads to a large Van Hove electronic density of states (Fig 4A). This modifies the BCS model in which  $N(e)$  was considered nearly constant for  $\epsilon = \epsilon_F \pm k_B \theta_D$ : very high values of  $T_c$  can be expected even if  $\lambda$  is small, because  $\theta_D$  is replaced by a Fermi like temperature  $T_F$ .

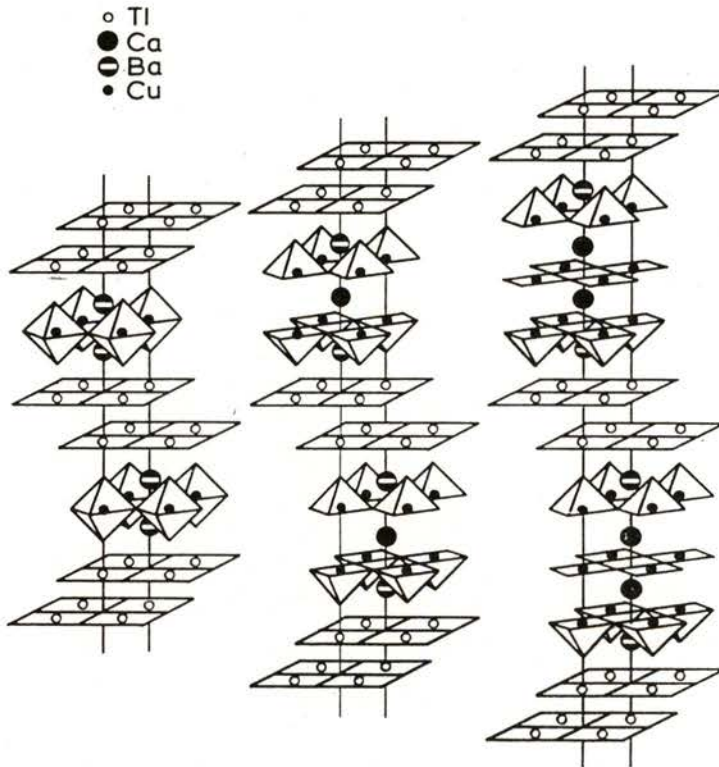


Fig 3. Atomic structure of  $\text{Tl}_2\text{Ba}_2\text{Ca}_{n-1}\text{Cu}_n\text{O}_{2n+4}$  with  $n=1,2,3$

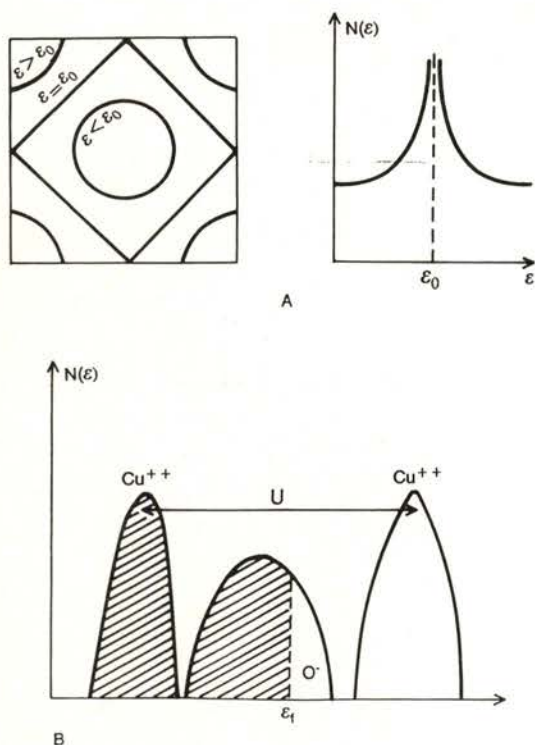


Fig 4. Fermi surface and density of state for a 2D metal for which  $\epsilon_0$  corresponds to a half filled band (A) ; if the Coulomb interaction  $U$  is larger than the band width, the half filled band of  $\text{Cu}^{++}$  is split into a filled and empty bandwidth, a possible intermediate oxygen band (B).

- For the Hubbard-Mott model [6] [7], for which  $U \gg T$ , the half filled band of  $\text{Cu}^{++}$  is split into two bands separated by the energy  $U$ : the low Hubbard band which is entirely filled by one electron/atom and the high empty Hubbard band. In the case of  $x = 0$  i.e.  $\text{La}_2\text{CuO}_4 = \text{La}_2^{+++}\text{Cu}^{++}\text{O}_4^{--}$  we have an

insulator with even an obligatory AF of the localized  $\text{Cu}^{++}$  spin electrons in the low Hubbard band (for which  $J_{dd} \equiv T^2/U$ ). For  $x \neq 0$  i.e.:

$\text{La}_{2-x}\text{Sr}_x\text{CuO}_4 = \text{La}_{2-x}^{+++}\text{Sr}_x^{++}\text{Cu}^{++}\text{O}_{4-x}^{--}\text{O}_x^-$ , the conductivity can be related to the oxygen band between the two Hubbard bands of Cu (Fig 4B); here the  $\text{O}^-$  corresponds to an insulating state (the filled oxygen band) while  $\text{O}^-$  corresponds to a conducting oxygen hole which is favoured by the positive Hall effect. The electronic structure is obviously different inside the  $\text{CuO}_2$  planes and outside these planes in the  $c$  direction, where the conducting resistivity  $\rho_c$  is due essentially to the apical oxygen  $\text{O}^-$  outside the  $\text{CuO}_2$  planes (the BaO planes for the 123 compounds). The destruction of the (3D) AF can be related also to the mobility of the  $\text{O}^-$  holes which can be perturbed by this AF if there is an  $\text{O}^- - \text{Cu}^{++}$  exchange interaction.

## II - MAIN RESULTS RELATED TO THERMODYNAMIC FLUCTUATIONS AND MAGNETISM.

1 - Thermodynamic fluctuations due to the anisotropic structure:

An important feature arises from the 2D character of the  $\text{CuO}_2$  planes and the amplitude of their coupling. To evaluate the thermal fluctuations we use the G.L. model i.e. [8] [9]:

$$F_S - F_N = -\alpha\psi^2 + \frac{\beta}{2}\psi^4 + \frac{\hbar^2}{2m_c} |\nabla\psi|^2 \quad (4)$$

(with  $\alpha = \alpha_0 (T_{CO} - T)$  where  $T_{CO}$  is the mean field transition temperature,  $m_c$  is the mass of a Cooper pair i.e.  $m_c = 2m^*$ ). Concerning the thermal fluctuations  $\langle \delta\psi^2 \rangle = \sum_q \langle \delta\psi_q^2 \rangle$  one obtains:

$$\psi^2 = \frac{\alpha}{\beta} - \langle \delta\psi^2 \rangle$$

$$T_c = T_{CO} - \frac{\beta}{\alpha_0} \langle \delta\psi^2 \rangle = \frac{T_{CO}}{1+x} \quad (5)$$

$$\langle \delta\psi \rangle^2 \equiv k_B T \frac{2m_c}{\hbar} \sum_q \frac{1}{q^2}$$

The term  $q^2$  is only valid for an isotropic structure, while for anisotropic structures one has to replace it by  $(q_{\parallel}^2 + (\xi_{\perp}^2/\xi_{\parallel}^2) q_{\perp}^2)$  where  $q_{\parallel}$  and  $q_{\perp}$  are wave vectors parallel and perpendicular to the  $\text{CuO}_2$  planes while  $\xi_{\parallel}$  and  $\xi_{\perp}$  are the corresponding superconducting coherence lengths. For an isotropic 3D atomic structure one obtains  $x \ll 1$  while for anisotropic structures one can obtain  $x \gg 1$  with

$$x = \frac{2k_B T_{CO}}{n} \frac{m^*(\text{Log } 2 + \Pi/2)}{\Pi \xi_{\perp} \hbar} \quad (6)$$

( $n$  is the density per unit volume of the

conducting electrons or holes). Large values of  $x$  are obtained for large values of  $T_{CO}$  and  $m^*$  and for low values of  $n$  and  $\xi_{\perp}$ . An important result is that for  $x \gg 1$ :

$$k_B T_c = \left( \frac{\Phi_0}{2\Pi} \right)^2 \frac{\xi_{\perp} \lambda_L^{-2}}{2(\text{Log } 2 + \Pi/2)} \quad (7)$$

This result can easily predict values of  $T_c$  between 10 and 100 K. The fact that the initial increase in  $T_c$  is always proportional to the inverse London penetration depth, namely  $\lambda_L^{-2}$ , has been observed by reference [10]: the theoretical value of  $dT_c/d\lambda_L^{-2} = 0.5 \cdot 10^{-7}$  is very close to the experimental value of  $0.4 \cdot 10^{-7}$ . For that reason one is obliged to consider that values of  $T_{CO} \gg 100$  K are related to the true electronic structure of the  $\text{CuO}_2$  planes and the attractive interactions of Cooper pairs. This very large value of  $T_{CO}$  is decreased by thermodynamic fluctuations so that we expect maxima in  $T_c \equiv 100$  K. The value of  $T_c$  will be sensitive also to proximity effects because between the superconducting planes there are metallic but non-superconducting planes for which a weaker superconducting order parameter is induced; this necessarily decreases  $T_c$  such that  $T_c(\text{proximity}) = T_c(1-Y)$  with  $Y$  proportional to  $d_S^{-2}$ , to  $\xi_{\perp}^{-4}$  and to  $d_N^2$ : for that

reason  $Y$  can decrease if  $d_s$  increases due to the occurrence of more superconducting planes per unit cell; but  $Y$  can increase if  $\xi_{\perp}$  decreases or if  $d_N$  increases ( $d_N$  and  $d_s$  are thickness of the non-superconducting and superconducting planes respectively). Nevertheless for  $n > 3$ ,  $T_c$  never increases even if  $d_s$  decreases because the electronic structure of all the  $\text{CuO}_2$  planes are not exactly similar.

A fundamental experimental result for the thermodynamic fluctuations and the proximity effect concerns the application of magnetic fields  $H < H_{c2}(T)$ . This often leads to a large increase in the resistive transition (Fig 5) which is related not only to the vortex flux flow but also to an increase of the thermodynamic fluctuations and the proximity effect. In the case of the proximity effect it was shown [11] that  $\xi_{\perp}(H) < \xi_{\perp}(0)$  so that  $T_c(H) < T_c(0)$ . But this field  $H$  has a non homogeneous repartition inside the sample so that the transition width  $\Delta T_c$  (Fig 5) can be related to  $T_c(0) - T_c(H)$  because of a non percolating situation. Experimentally evidence arises from magnetoresistance measurements which are the same above and below  $T_c(0)$  [12], and the existence of a gap  $D(T)$  which goes to zero at  $T_c(H)$  [13] and therefore, cannot be related to  $H \cong H_{c2}$ .

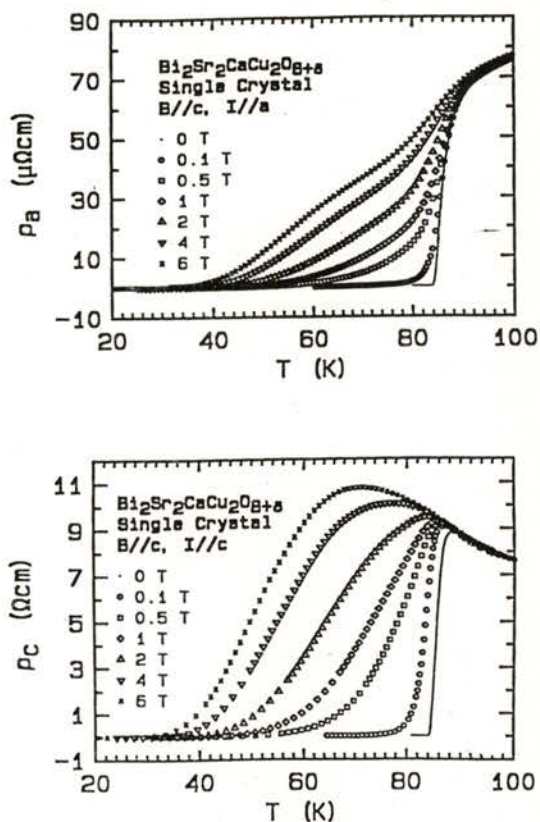


Fig 5. Effects of magnetic fields on the transition width of the electrical resistivity.

## 2 - AF Magnetism of Copper:

a) - (3D) AF: There is no coexistence of the antiferromagnetic transition  $T_N(3D,x)$  and the superconducting transition  $T_c(x)$  because  $T_N(3D,x)$  decreases strongly with  $x$  while  $T_c(x)$  only appears a bit later (Fig 1, 2). The value of  $T_N(3D,x)$  is related to two exchange interactions of  $3d^9 \text{Cu}^{++}$  spins i.e.  $J_{\parallel} = J_{dd}$  inside the

$\text{CuO}_2$  planes and  $J_{\perp} \ll J_{\parallel}$  for  $\text{Cu}^{++}$  spins between different  $\text{CuO}_2$  planes along the  $c$  axis. For  $x \equiv 0$  it leads to:

$$T_{N(3D)} \equiv \frac{J_{\parallel}}{1 + \text{Log} \frac{J_{\parallel}}{J_{\perp}}} \quad (8)$$

while for  $x \neq 0$ ,  $T_{N(3D,x)}$  decreases due to the interaction with  $\text{O}^-$  holes whose density increases with  $x$ . Nevertheless for  $\text{Nd}_{2-x}\text{Ce}_x\text{CuO}_4$  (Fig 1) and  $\text{YBa}_2\text{Cu}_3\text{O}_{6+x}$  (Fig 2) there is a common border between  $T_{N(3D,x)}$  and  $T_c(x)$ , an effect which can be explained by the Ginzburg-Landau model [14] for which

$$\Delta F_S = -\alpha_1 \Psi^2 + \frac{\beta_1}{2} \Psi^4$$

$$\Delta F_N(\text{AF}) = -\alpha_2 M^2 + \frac{\beta_2}{2} M^4 \quad (9)$$

$$F_{NS} = \gamma M^2 \Psi^2$$

with  $\alpha_1 = \alpha_{10}(T_{CS}^0 - T)$  and  $\alpha_2 = \alpha_{20}(T_{CS}^0 - T)$ .  $M$  is the AF order parameter, while  $\gamma > 0$  is related to the opposition of the two order parameters, and  $\Psi$  is the same as in formula (2). In the case of  $\gamma = 0$ ,  $T_c(x)$  and  $T_{N(3D,x)}$  coexist (Fig 6). Then one can show that for  $\gamma^2 < \beta_1 \beta_2$ , the coexistence continues to hold for  $T_c(\gamma,x)$  and  $T_{N(\gamma,x)}$  but their values decrease with  $\gamma$ . But for  $\gamma^2 > \beta_1 \beta_2$  there can be no coexistence but there can be a common border if the two condensation energies  $-\alpha_1^2/2\beta_1$ ,  $-\alpha_2^2/2\beta_2$  are not very different (Fig 6). For  $\text{La}_{2-x}\text{Sr}_x\text{CuO}_4$  (Fig 1), there is no common border which cannot be

explained by  $\gamma$  and which is related to the interaction of  $\text{Cu}^{++}$  and  $\text{O}^-$  holes. This non coexistence where  $x$  represents the density of  $\text{O}^-$  holes, can be explained by the fact that when decreasing  $x$  one approaches the metal-insulator transition with a weak mobility of the  $\text{O}^-$  holes responsible of the superconductivity: this can favour the repulsive Coulomb interaction between  $\text{O}^-$  holes and  $T_c(x)$  can disappear if  $\mu^* > \lambda$ . We should also note also that the attractive interaction  $\lambda$  can decrease if  $x$  decreases.

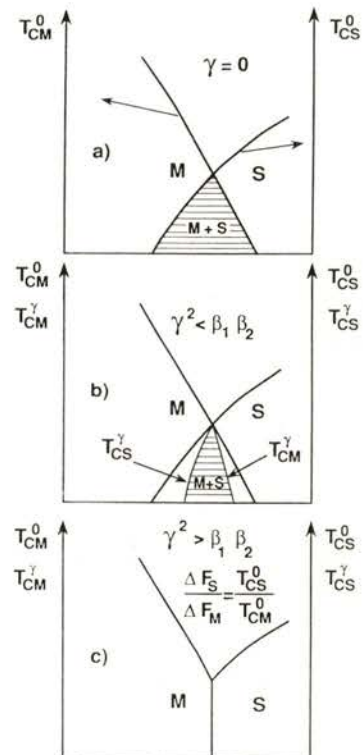
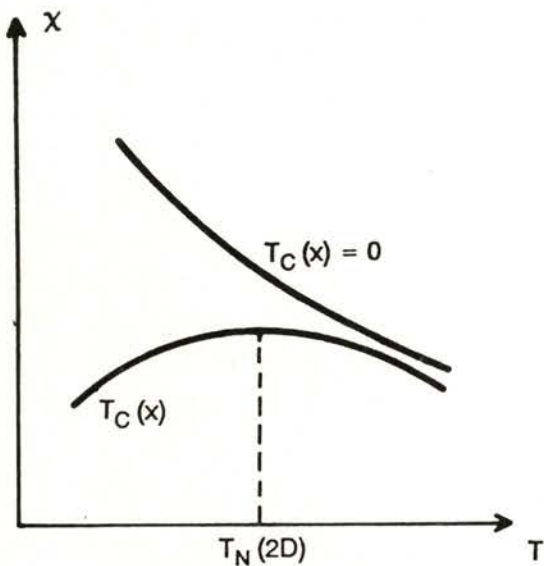
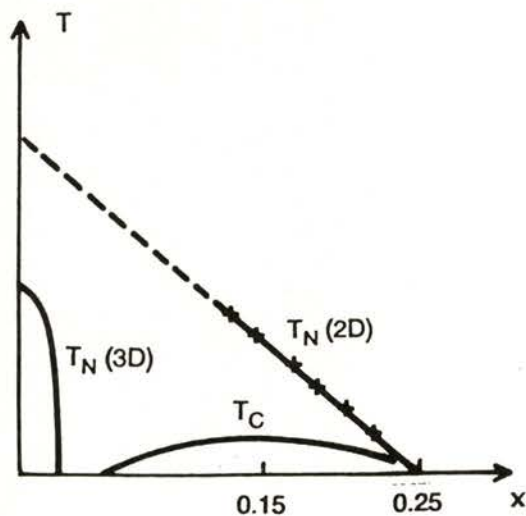


Fig 6. Variation as a function of  $x$  of the superconducting (S) and magnetic (M) transition for (a)  $\gamma = 0$ , for (b)  $\gamma^2 < \beta_1 \beta_2$  and for (c)  $\gamma^2 > \beta_1 \beta_2$  with  $(\Delta F_M / \Delta F_S) \equiv (T_{CM}^0 / T_{CS}^0)$



a



b

Fig 7. For  $\text{La}_{2-x}\text{Sr}_x\text{CuO}_4$ , the magnetic susceptibility above  $T_C(x) \neq 0$  shows a 2D Néel temperature (a) whose values tends to zero like  $T_C(x)$  for  $x > 0.25$  (b).

b) - (2D) AF: of course even for  $x \equiv 0$  there appears above  $T_N(3D)$  a two dimensional AF in the  $\text{CuO}_2$  planes for which the susceptibility continues to increase beyond 1000 K because  $T_N(2D) \equiv J_{\parallel}$ . Neutron scattering studies show that the coherence length of this (2D) AF decreases with T above  $T_N(3D)$  [15].

But when as a function of x,  $T_N(3D,x)$  disappears there is now well documented experimental evidence by neutron scattering [16] [17] studies and susceptibility measurements above  $T_C$  [18] that there is coexistence between the superconductivity and this (2D) AF in the  $\text{CuO}_2$  planes for which there are also thermodynamic fluctuations and a short AF coherence length which decreases with x [16] [19] down to 4 Å for the 123 compounds when  $x \equiv 1$  i.e.  $T_C \equiv 92\text{K}$ . The susceptibility measurements also shows AF Néel transitions of (2D) character with a very large maximum as a function of T (Fig. 7a). This favours of course the Hubbard model. A second fundamental effect observed for  $\text{La}_{2-x}\text{Sr}_x\text{CuO}_4$  and Bi 2212 compounds concerns the fact that  $T_C$  and  $T_N(2D)$  disappear together when x increases and they become more metallic (Fig. 7b) [18]. It is easy to understand that the good mobility of  $\text{O}^-$  holes does not favour the (3D) and (2D) AF of  $\text{Cu}^{++}$  if there is an exchange interaction  $J_{pd}$  between  $\text{Cu}^{++}$  spins and  $\text{O}^-$  spins. This situation suggests strongly that the origin of these higher  $T_C$  superconductors can be related also to

an attractive interaction between  $O^-$  holes or, even more likely, to the exchange of magnetic singlet-triplet excitations of the nearly singlet pair liquid of  $Cu^{++}$  namely the  $Cu^{++} \uparrow Cu^{++} \downarrow$  which can replace the phonon excitation for the classical superconductors. Because this singlet-triplet excitation favours the  $O^-$  mobility one can obtain two attractive interactions i.e. (Fig 8):

$$\lambda = N(\xi_F) \frac{t^2}{J_{dd}} \quad [6]$$

$$\lambda = N(\xi_F) \frac{J_{pd}^2}{J_{dd}} \quad [20]$$

with  $T_{CO} \equiv J_{dd} e^{-1/\lambda}$ . Of course  $\lambda$  can be very large leading to large  $T_{CO}$  values because  $J_{dd} \equiv 1500$  K. There are also theoretical models which indicate that the resistivity above  $T_c$  is more related to magnetic fluctuating excitations than to phonons, but one cannot entirely exclude the attractive interaction due to phonons and to magnetic excitations. It is also easy to show that  $\lambda$  due to magnetic excitations can decrease if the AF coherence length increases, because it does not favour completely the singlet-triplet excitation of the  $Cu^{++}$  singlet pair liquid if there are AF correlations between neighbouring singlets. For that reason it is evident that  $\lambda$  decreases when one approaches the metal-insulator transition which favours the (3D) AF, while  $\lambda$  decreases also when one approaches the more metallic situation which destroys the (2D) AF. All this favours the importance of the (2D) AF magnetic excitation.

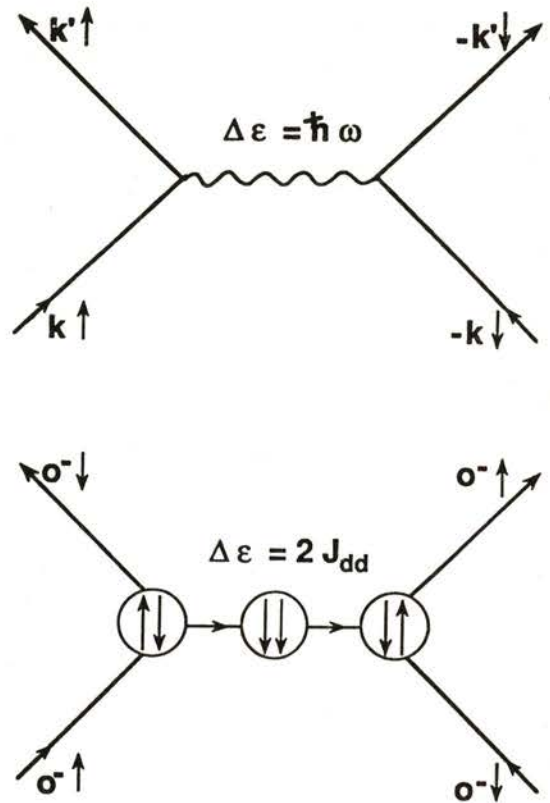


Fig 8. Attractive interaction between two electrons or two  $O^-$  holes through the exchange of a phonon energy  $\Delta \epsilon = \hbar \omega$  or a magnetic singlet-triplet energy  $\Delta \epsilon = 2 J_{dd}$  between two  $Cu^{++}$  spins.

### 3 - Effects of magnetic and non magnetic impurities on $T_c$ :

a) - Effects of Gd, Fe outside the  $CuO_2$  planes :

- For  $Y_{1-x}Gd_xBa_2Cu_3O_7$  there is no change of  $T_c$  even up to  $x = 1$ . This

means that there is no magnetic interaction between Gd and the conducting Cooper pairs in the  $\text{CuO}_2$  planes. But for  $\text{Gd}_{1+x}\text{Ba}_{2-x}\text{Cu}_3\text{O}_7$  the value of  $T_C$  decreases as a function of  $x$  (Fig 9) because  $\text{Gd}^{3+}$  is in the  $\text{Ba}^{2+}$  plane implying that the decrease of  $T_C$  is more related to a change of the electronic structure due to the decrease of the  $\text{O}^-$  holes transformed into  $\text{O}^{2-}$ .

- A similar effect is obtained by  $\text{Fe}^{3+}$  which goes mainly into the chain planes  $\text{Cu}(1)\text{O}$  outside the  $\text{CuO}_2$  planes. For that reason there can be a strong decrease of  $T_C$  (Fig 9) for  $\text{YBa}_2\text{Cu}_{3-y}\text{Fe}_y\text{O}_{7+\delta}$ . There is experimental evidence that this effect is not related to magnetic interactions with the Cooper pairs but only to a change of the electronic structure. It has been shown that there is no change of  $T_C$  for  $\text{YBa}_2\text{Cu}_{3-y}\text{Fe}_y\text{O}_{7+y}$  (Fig 9):  $\text{Fe}^{3+}$  which substitutes  $\text{Cu}^{2+}$  can destroy  $\text{O}^-$  holes which are recreated by  $\text{O}_y$ . Furthermore [21] the  $T_C$  decrease due to  $\text{Fe}^{3+}$  can be compensated by the substituting  $\text{Y}^{3+}$  with  $\text{Ca}^{2+}$ ; in this case, the decrease of  $T_C$  is much smaller for  $\text{Y}_{1-x}\text{Ca}_x\text{Ba}_2\text{Cu}_{3-y}\text{Fe}_y\text{O}_7$  if  $x \equiv y$  because  $\text{Fe}^{3+}$  decreases the  $\text{O}^-$  hole density while  $\text{Ca}^{2+}$  increases it.

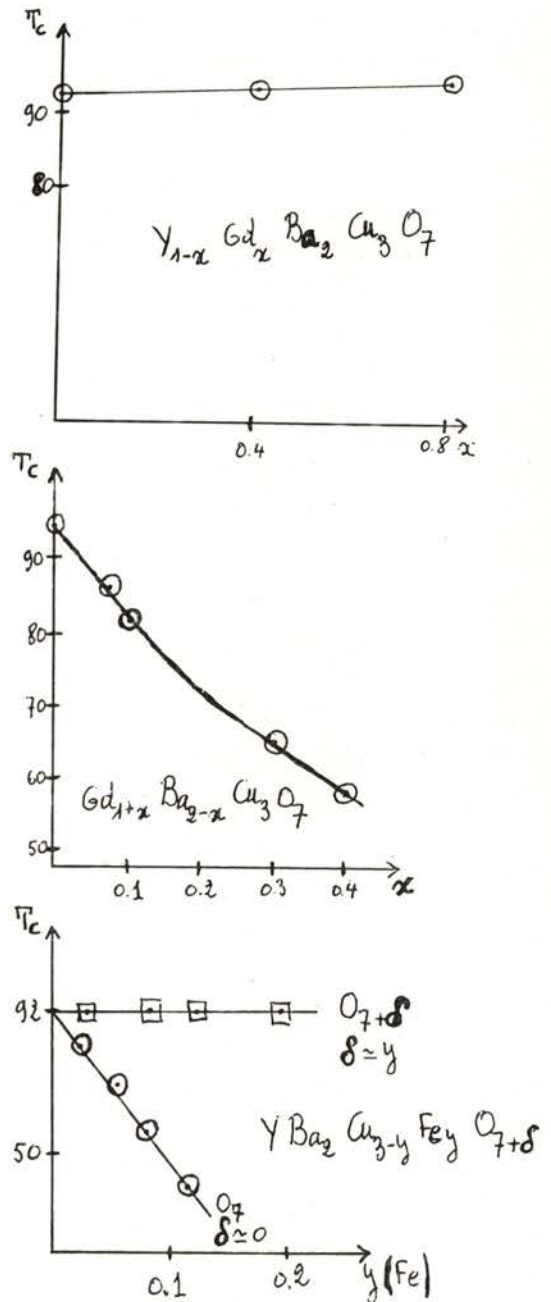


Fig 9. Variation of  $T_C$  for  $\text{Gd}_{1+x}\text{Ba}_{2-x}\text{Cu}_3\text{O}_7$  and  $\text{YBa}_2\text{Cu}_{3-y}\text{Fe}_y\text{O}_{7+\delta}$  as a function of  $x$  and  $y$  concentrations. But for  $\delta \equiv y$ ,  $T_C(y)$  does not change.

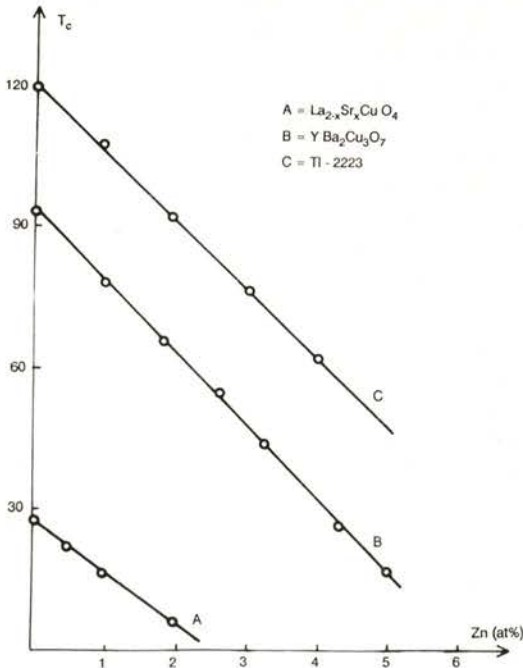


Fig 10.  $T_C$  dependence of several high  $T_C$  compounds by the substitution of Cu by Zn.

b) - Effects of  $Ni^{++}$  and  $Zn^{++}$  substituting  $Cu^{++}$  inside the  $CuO_2$  planes:

A surprising result is that  $T_C$  decreases much more for non magnetic Zn; in fact  $\Delta T_C \cong 13$  K for 1% of Zn [22] (Fig 10). This effect can be explained because Zn changes the (3D) AF.  $T_N(3D)$  goes to zero rapidly for  $YBa_2Cu_{3-y}Zn_yO_{6+x}$  (i.e at  $x = 0.25$  for  $y = 0.037$ ) which is very different from what is shown in Fig 2. But Zn can also destroy the (2D) AF if a

copper singlet  $\uparrow Cu^{++} Cu^{++} \downarrow$  is transformed into  $\uparrow Cu^{++} Zn^{++}$ . This means that there are three different reasons for the decreases of  $T_C$ : i) the attractive interaction related to a singlet-triplet excitation decreases because this singlet-triplet excitation disappears near Zn. ii)  $Zn^{++}$  creates also a local paramagnetic moment of  $Cu^{++}$  whose interaction with  $O^-$  hole pairs can destroy these pairs. iii) decreased mobility of the  $O^-$  holes due to the atomic disorder created by Zn: this can favour the repulsive Coulomb interaction between  $O^-$  holes i.e.  $\mu^*$ . The  $Zn^{++}$  does not change the  $O^-$  hole density as shown by the Hall effect (only above 300 K) [23].

The effect of  $Ni^{++}$  on  $T_C$  may be less important because it does not suppress the magnetic singlet-triplet excitation and does not create isolated paramagnetic  $Cu^{++}$  moments. There can be nevertheless an atomic disorder with less mobility of the  $O^-$  holes and an increase of  $\mu^*$ .

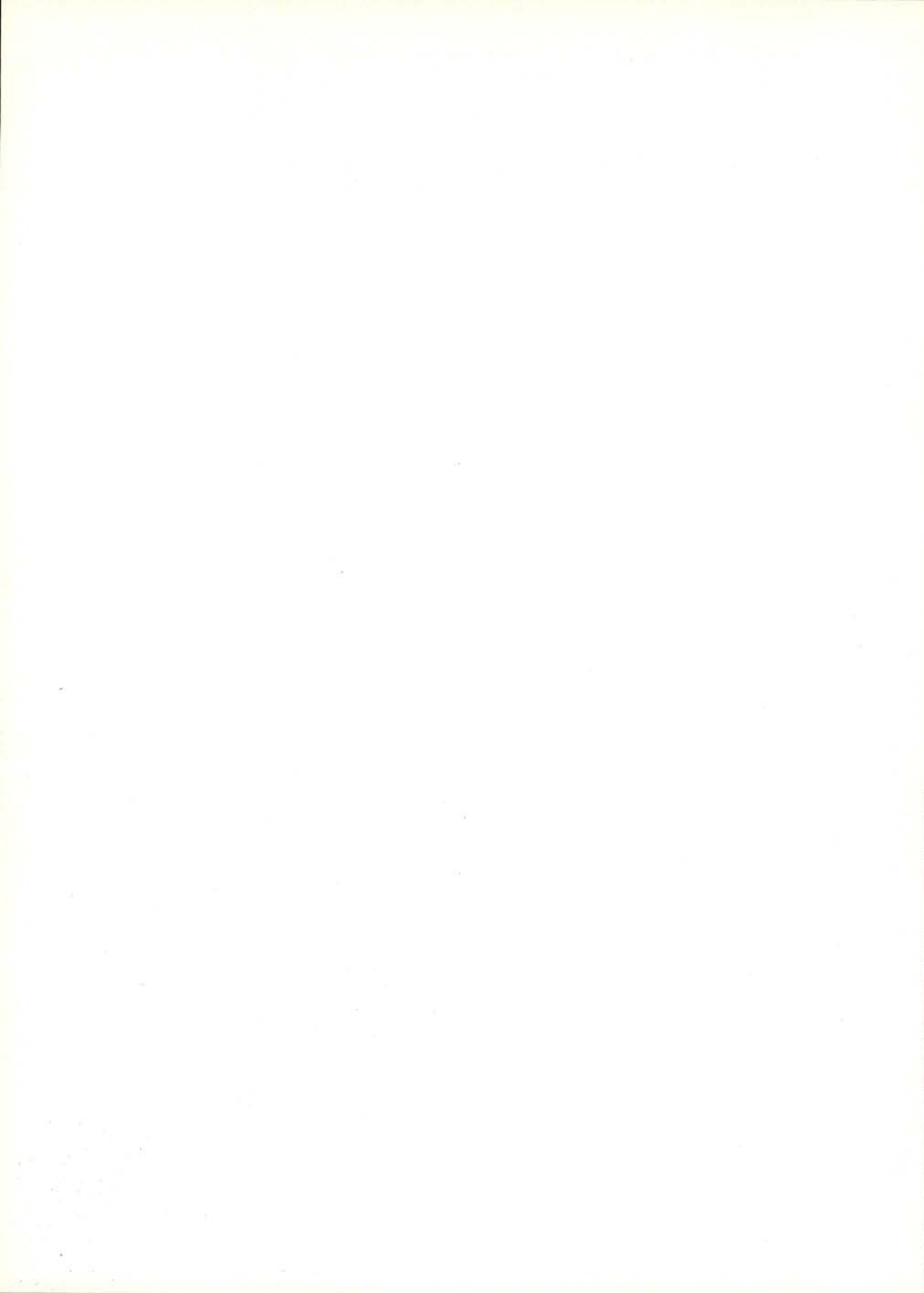
### III - CONCLUSION

It has become increasingly evident that the magnetism of copper [but only the (2D) AF] has an enhancing effect on  $T_C$  which is apparently related to an attractive interaction due to singlet-triplet excitations. However electron-phonon attractive interactions could also

explain the negative effects due to thermal phonons near  $T_c$  as in the case of some classical superconductors. The (2D)-like atomic structure decreases the true very high mean field value  $T_{CO}$ , and favours (near  $T_c$ ) the thermodynamic fluctuations of the superconducting order parameter and also the vortices. The effect of Zn has a fundamental effect on the decrease of  $T_c$  which can be related to i) the localization of the oxygen holes related to atomic disorder ii) the perturbation of the (2D) AF with occurrence of paramagnetic moments of  $Cu^{++}$ .

## REFERENCES

- [1] Superconductivity, Ed. R.D. Parks, M. Dekker INC New York (1969)
- [2] Studies of High Temperature Superconductors, Ed. A. Narlikar Nova Science Publishers (1989)
- [3] K. Kadowaki, J.N. Li, J.J.M. Franse, J. Magnetism and Magn. Mat. **90-91** 678 (1990)
- [4] J. Labbé, J. Bok, Europhy. Lett. **3** 1225 (1987)
- [5] C.C. Tsuei, D.M. News, C.C. Chi, P.C. Pattnaik : Phys. Rev. Lett. **65** 2724 (1990)
- [6] M. Heritier: J.Phys. (Paris) **48** 1849 (1987)
- [7] F.C. Zhang, P.M. Rice Phys. Rev. **B37** 3759 (1988)
- [8] S. Hirooka, T. Tanaka: Phys. Rev. **B41** 11588 (1990)
- [9] J.P. Burger, M. Nicolas : C.R.A.S. (Paris) t.312, Serie II, 355 (1991)
- [10] Y.J. Uemura and al : Phys. Rev. Lett. **62** 2317 (1989)
- [11] M.A.M. Gijs and al : Sol. St. Com. **71** 575 (1989)
- [12] H. Raffy, O. Laborde, S. Labdi, P. Monceau : C.R.A.S. (Paris) t.311 Serie II, 599 (1990)
- [13] L.C. Brunel, S.T. Louic, G. Martinez, S. Labdi, H. Raffy : Phys. Rev. Lett. **66** 1346 (1991)
- [14] J.P. Burger, Y. Zanoun : C.R.A.S. (Paris) t. 314 serie II 763 (1992)
- [15] S. Chakravarty, B.I. Halperin, D.R. Nelson : Phys.Rev. **B39** 2344 (1989)
- [16] R.J. Birgenau and al : Rev. **B39**, 2868 (1989)
- [17] S.K. Sinha Int. Conf. on superconductivity, Bangalore (India) Ed. S.K. Joshi, C.N.R. Rao p.269 (1990)
- [18] M.Oda, H. Matsaki, M. Ido : Sol St. Com. **74** 1321 (1990)
- [19] J.Rossat-Mignod and al : Int. Conf. on Neutron Scattering, Oxford, UK (1991)
- [20] S. Kurihara : Phys. Rev. **B39** 6600 (1989)
- [21] Suryanarayanan and al : to be published
- [22] A.V. Narlikar : Int. Conf. on Superconductivity World Scientific Ed. S.K. Joshi, C.N.R. Rao p. 103 (1990)
- [23] S.K. Agarwal, R. Suryanarayanan, O. Gorochov, V.N. Moorthy, A.V. Norlikar : Sol. St. Com. **79** 857 (1991).



## FRACTALS AND PHASE TRANSITIONS

D. STAUFFER

Institute for Theoretical Physics, Cologne University, d-W-5000 Köln 41, Germany

**ABSTRACT-** A wire has a mass proportional to its length, the mass of a disk varies proportional to the squared radius, and the mass of an iron sphere is proportional to the third power of the radius. Therefore these objects have a dimension equal to one, two or three. FRACTALS are objects where the mass varies with some other power of the radius, and that power is called the fractal dimension  $D$ . We show examples, in particular from the physics of phase transitions, where  $D$  is smaller than the normal dimension by  $\beta/\nu$ .

### 1. INTRODUCTION

Fractals today are spread all over the scientific literature and continents, as is quite appropriate for the person of Mandelbrot (from Lithuania, Poland, France, and the USA) who invented the general concept[1]. Fractal elements appeared centuries ago in Italian church paintings and flood dike constructions [2] and are inherent also in clouds and trees. Fractal Mandelbrot sets have been printed on covers of scientific journals without apparent relation to the content. The present review does not deal with fractals as a new and separate topic. Instead it wants to relate them to examples from traditional physics and their teaching.

### 2. BASIC CONCEPTS

If you look at the world around you, you can normally distinguish easily between man-made and natural objects: buildings, channels, and streets are dominated by straight lines, whereas trees, rivers, and coast lines are more complicated. Traditional teaching of mathematics and physics deals with straight lines, circles, spheres and other simple objects; so how can we describe the more complicated objects like trees? The circumference and area of a circle of radius  $R$  are  $2\pi R$  and  $\pi R^2$ , whereas surface and volume of a sphere are  $4\pi R^2$  and  $4\pi R^3/3$ , respectively. What are surface and volume of a tree with height  $R$ ? Clearly that is a more difficult

question, and it is not just of academic interest: due to man-made combustion processes, the carbon-dioxide level in the atmosphere has increased significantly over the last century. This increase may, via the *greenhouse effect*, lead to an increase of the average temperature, causing larger deserts and flooding of low-lying areas. Trees counteract the greenhouse effect by consuming carbon dioxide through the surface of their leaves. So the effect of cutting a tree in the Amazon basin on the atmospheric temperature depends on the surface of a tree.

Many objects follow simple power laws, and so we may generalize the above formulas to a proportionality between mass  $M$  and radius  $R$ :

$$M \propto R^D$$

with some empirical exponent  $D$ . Thus  $D = 2$  and  $3$  for circle and sphere if we identify the volume with the mass; and  $D = 1$  and  $2$  if instead we identify the surface with the mass. So in these simple artificial examples,  $D$  or  $D+1$  equals the Euclidean dimension  $d$  of the space, depending on whether we look at volume or surface. Such objects are not called fractals. If, however, the exponent above  $d$  is different from the Euclidean dimension  $d$  or  $d-1$  and thus in general not an integer, then we call these objects fractal with a *fractal dimension*  $D$ .

So what about the fractal dimension of plants? Fig.1 shows diffusion-limited aggregates with 10 and 30 million sites on a plane, and the branches of this figure have a clear similarity with branches of plants. Comparing such aggregates of different mass (the mass is measured by the number of sites) one finds a fractal dimension near 1.7 on a plane, and about 2 on three-dimensional space. The power laws in such computer-generated objects are supposed to be valid only asymptotically, that means for large enough clusters. The author of Fig.1, Peter Ossadnik in Hans Herrmann's group at HLRZ Supercomputer Center Jülich, Germany, competes with Mandelbrot's group for the world record. In natural fractals, as opposed to computer-generated or mathematical objects, the power laws are often valid only in a suitable mass interval: Very young small trees, and extremely high trees, may show deviations.

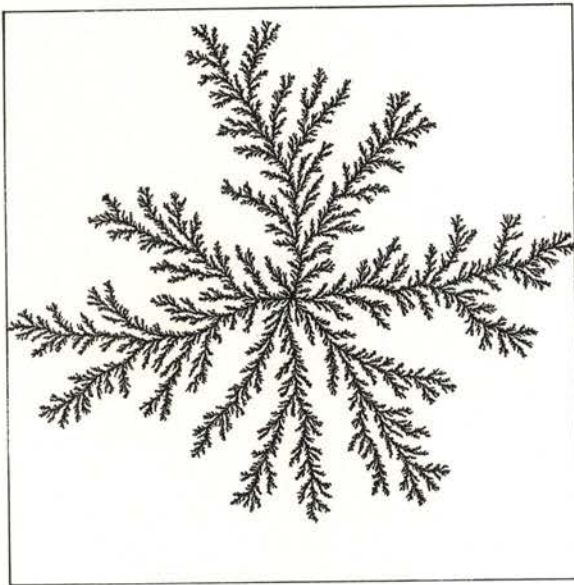
How is Fig.1 generated? One starts with an occupied site in the center of the plane, and then one adds one particle after the other to the growing cluster in the following way: A new particle is put onto the plane somewhere away from the cluster. Then this new particle diffuses, that means it randomly moves in arbitrary directions like a molecule in the air. Once it hits the cluster it stays at that place forever and becomes part of the cluster. If we simplify the simulation by letting all particles move and sit on a

square lattice only, we see the anisotropic lattice structure and get a lower fractal dimension if we simulate multi-million clusters.

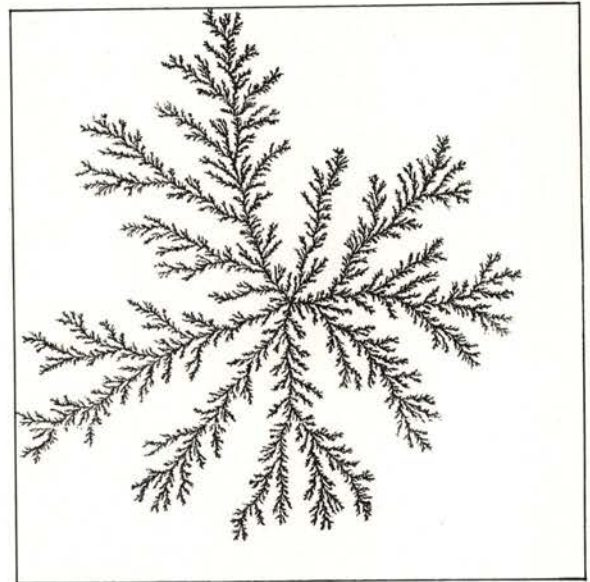
Fig.1 also illustrates the concept of *self-similarity*: A big branch looks quite similar to one of its small branches, and this small branch looks similar to a twig emanating from it. Alternatively, whole clusters with different numbers of sites look similar to each other, Fig.1. A mathematical

description of "looks similar" is difficult, however, and therefore I recommend to talk about self-similarity only if one knows what it means, e.g for deterministic fractals like the Sierpinski gasket [1].

These diffusion-limited aggregates were invented in 1981 and thus hardly constitute traditional physics subjects. Thus the next two sections instead deal with the phase transition between water and its vapor.



*Off-lattice DLA with 30,000,000 particles*  
Peter Ossadnik, HLRZ, KFA Jülich



*Off-lattice DLA with 10,000,000 particles*  
Peter Ossadnik, HLRZ, KFA Jülich

Fig.1: Diffusion-limited aggregates, by P. Ossadnik, with 10 and 30 million sites ( $D = 1.7$ ).

### 3. CLOUDS AND PERCOLATION

When water vapor condenses in the atmosphere, it forms small droplets around some solid particles which then grow to micron size. Many of these droplets form a cloud, and if the droplets grow too large they fall down as rain. How do clouds look like? Clouds move in three dimensions but what we see from them are two-dimensional projections (except if the clouds are very transparent). The interior of these clouds, as projected onto a two-dimensional surface, is usually dense, and thus behaves like a circle: projected

area  $\propto R^2$  for a cloud of radius  $R$ . Thus the area is not fractal. More interesting is the perimeter of the cloud, that means the number of empty sites which touch a cloud site after the projection. [We imagine the coordinates of the clouds to be discretized, where for example each square meter corresponds to one site and is either wet (cloud) or dry (surrounding).] This perimeter for a simple circle would vary as  $R$  but for clouds it was found empirically to vary roughly as  $R^{1.3}$  or  $\text{area}^{2/3}$ . Fig.2 shows a computer model of the cloud projection[3] which agrees roughly with this fractal dimension.

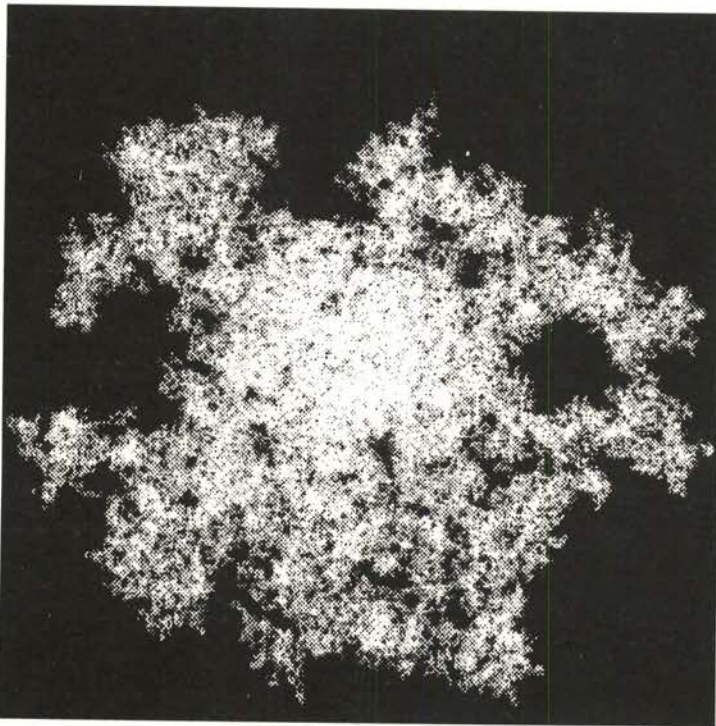


Fig.2: Computer model of three-dimensional cloud projected onto two dimensions ( $D = 1.3$ ); from ref.3.

A simplified form of this computer model was investigated by two high-school students[4] who had not yet even studied at the university. They looked at percolation[5], a model originally invented by chemistry Nobel laureate Flory to describe the gelation of branched polymers (boiling eggs, milk-to-cheese transition, formation of gelatine pudding). On a simple cubic lattice first occupy the center site. Then add one site after the other by selecting a new neighbor of an already occupied site. Occupy this neighbor with probability  $p$  and leave it empty with probability  $1-p$ . After a site is determined as being empty or occupied, it stays in that status during the whole process of building up this cluster. We now observe a transition: For probabilities  $p < p_c$  with a threshold  $p_c$  near 0.3116 only finite clusters are formed, whereas for  $p > p_c$  sometimes this growth process continues up to infinity (i.e. until it touches the borders of the simulated lattice.) Right at  $p = p_c$  the clusters are fractal with a fractal dimension  $D$  near 2.53. In Ref.4 the authors produced such fractal clusters at  $p = p_c$  on an Amiga computer, projected them onto a two-dimensional plane, and found the perimeter of these projections to follow roughly the same power law as a function of radius or area as the clouds and as the more complicated model of ref.3. We see, good physics research can also be done on small computers and without a long university curriculum. Historically, the percolation problem seems to be the first case where phase transitions were coupled to fractal concepts [6].

#### 4.FRACTAL DROPLETS IN ISING MODELS

How can we understand by a simple model the phase transition between a liquid and its vapor? The Ising model of 1920 allows each site for a large lattice to be either occupied or empty; occupied sites attract each other. Mathematically this model has an interaction energy

$$J = \sum_{i \langle k} S_i S_k - B \sum_i S_i$$

where the "spin"  $S_i$  is +1 for an occupied and -1 for an empty site and where  $i$  and  $k$  in the double sum correspond to nearest neighbors on the lattice. A simple *cellular automata* simulation for  $B=0$  takes into account the conservation of energy: Starting with a random fraction  $p$  of all sites occupied, and the rest empty, we go sequentially through the lattice and flip a spin if and only if it has as many occupied as empty neighbors. Low  $p$  correspond to low energies and thus low temperatures, whereas  $p \approx 1/2$  corresponds to a high energy at very high temperatures. For  $p$  above a critical concentration, 7.55 percent on the square lattice, after many sweeps through the lattice we have as many occupied as empty sites, which corresponds to a supercritical fluid like air at room temperature. For smaller  $p$  the majority of sites remains empty, corresponding to the vapor phase below the critical temperature. This model is

symmetric with respect to occupied and empty. Thus for  $p$  above 92.45 percent, again we will not get a density of 1/2 but a majority of sites occupied, corresponding to the liquid phase at low temperatures, like very cold liquid air. Thus the Ising model, which can also be simulated by other methods, shows one fluid phase above the critical temperature, and two phases (vapor and liquid) below this temperature, just as real fluids so. The Ising behavior very near this critical temperature is known to agree even quantitatively with real fluids.

Fig.3 shows the configuration obtained in a few seconds on a workstation at  $p = 0.15$ , that means at

temperatures somewhat above the critical temperature. (Ref. 2b lists a simple BASIC program; I have used this problem to teach university students even in their first weeks.) Half of the sites are occupied and the other half is empty, but the distribution is not at all random: due to the interaction between neighboring sites the occupied sites tend to cluster together, and to leave large holes. These pictures are very similar to those obtained experimentally for real fluids in recent years[9] and give rise to *critical opalescence*, the strong scattering of light near the fluid critical point.



Fig.3: Ising configuration for part of a 79\*79 square lattice after 1000 sweeps through the lattice with the cellular automata algorithm. Only the occupied sites are shown.



Fig.4: A large droplet from Fig.3 shown isolated after taking into account the helical boundary conditions. The droplet was isolated manually (can you find my error ?); ref.5 gives a computer program.

This critical point is known since more than a century, and van der Waals made the first theory for it in his 1873 thesis. Can we do better today ? Let us transform these impressions into a quantitative droplet picture[5]. A droplet is a group of neighboring occupied sites, as shown in Fig.4.

(Experts require in addition that the sites are connected with a probability  $1 - \exp(-2J/k_B T)$ .)

In a classical ideal gas we have only single molecules, no larger droplets, and  $PV = Nk_B T$  connects pressure, volume, particle number, Boltzmann's constant, and absolute temperature. If we have  $N_s$

droplets of  $s$  molecules each, due to the clustering shown above, then

$$PV = \sum_s N_s k_B T$$

is a reasonable generalization, neglecting the interactions between different droplets. (Similarly, the total atmospheric pressure is the sum of the partial pressures of nitrogen, oxygen, water vapor, carbon dioxide, etc.) The number of molecules

$$N = \sum_s N_s s$$

is even exact. We know that the density difference  $N_c - N$  of a vapor to the critical

density  $N_c$  (for molecules with unit mass in a unit volume) varies slightly below the critical temperature  $T_c$  as  $(T_c - T)^\beta$ . Here  $\beta = 1/8$  or  $0.32$  in two and three dimensions is one of the critical exponents for which Kenneth G. Wilson got the 1982 Physics Nobel prize. Thus

$$\sum_s (N_s(T_c) - N_s(T)) s \propto (T_c - T)^\beta$$

Another quantity of interest is the spatial extent  $\xi$  of the correlations, the correlation length. We expect it to vary as the typical cluster radius  $R_s$ , or

$$\xi^2 \propto \sum_s R_s^2 s^2 N_s / \sum_s s^2 N_s$$

The droplet radius then gives a fractal dimension  $d$  through  $R_s^D \propto s$ . The correlation length, on the other hand, is known to diverge near the critical point as  $(T - T_c)^{-\nu}$ . Scaling arguments[5] then give

$$D = d - \beta/\nu$$

for the fractal dimension in  $d$  dimensions;  $D = 15/8, 2.49,$  and  $3$  for  $d = 2$  to  $4$  (in the van der Waals theory,  $D = d - 1$ ). The droplet volume varies as  $R_s^d$ , and thus the average density within a droplet decays as  $s / R_s^d \propto s^{-\beta/D\nu} = s^{-1/\delta}$ . (Here the critical exponent  $\delta$  relates pressure and density on the critical isotherm:  $P(T_c) - P_c = (N(T_c) - N_c)^\delta$ .) due to this

decrease of the density with increasing droplet mass the critical droplets are fractal and differ from simple raindrops.

[This fractal dimension is valid exactly at the critical point. Below the critical temperature we expect large droplets to be quite spherical,  $D = 3$ , whereas above the critical temperature they should be similar to the so-called *lattice animals* with  $D = 2$  in three dimension.]

Thus we see that the fractal dimension can be expressed as a combination of critical exponents which were of interest to physicists since decades. And more qualitatively, the well-known critical opalescence is the scattering of light on fractal droplets. direct experimental determinations[9] of the droplet radius as a function of the number  $s$  of molecules in the droplet have, to my knowledge, not yet been made. Computer simulations[7] in the Ising model, on the other hand, have confirmed within about one percent the predicted values for  $D$ , nearly two decades after which the first speculations were published. Unfortunately, such accuracy is not yet good enough to distinguish between the fractal dimension of the Ising model and that of percolation, nor has the claim  $D=2$  above  $T_c$  been confirmed reliably by simulations.

But computers get faster and better every year, equilibrium is reached faster by flipping whole droplets together instead of only single spins[10], and I think that with hundreds of processors, coupled

together already today in large parallel computers[8], such accuracy may be possible now. Let us see if the experimental physicists beat the computational physicists in the determination of fractal dimensions at the critical point of fluids. This Ising model is a nice example where old problems are getting solved better and better even today, through new ideas, faster computers, and international cooperation.

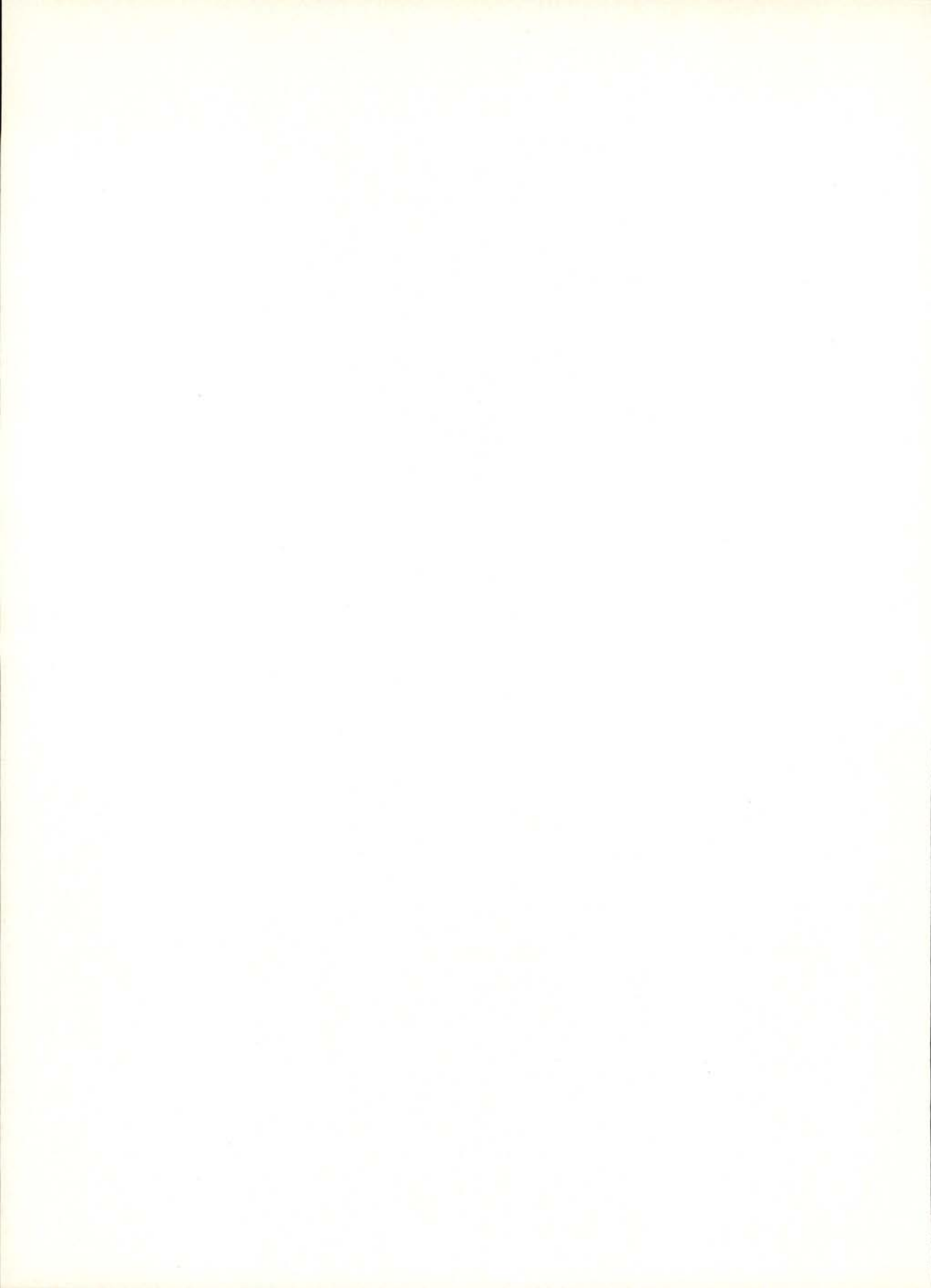
We thank J.A.M.S., Duarte for advice on this conference.

#### REFERENCES

- [1] Mandelbrot, B. B. "The Fractal Geometry of Nature", Birkhauser, Boston, 1982.
- [2] Guyon, E. and Stanley, H.E., "Fractal Forms", Elsevier / North Holland, Amsterdam 1991; see also Stauffer, D. and Stanley, H.E.,

"From Newton to Mandelbrot", Springer Verlag, Heidelberg, 1990.

- [3] Nagel, K. and Raschke, E., *Physica A* **182**, 519 (1992).
- [4] Schneider, T. and Wöhlke, T., *Physica A*, in press (1992).
- [5] Stauffer, D. and Aharony, A., "Introduction to Percolation Theory", Taylor and Francis, London, 1992.
- [6] Leath, P.L., *Phys.Rev.* **B 14**, 5046 (1976).
- [7] Alexandrowicz, Z., *Physica A* **160**, 310 (1989); Wang, J. S. and Stauffer, D., *Z.Physik* **B 78**, 145 (1990); Jansen, K. and Lang, C.B., *Phys. Rev. Letters* **66**, 3008 (1991).
- [8] Flanigan, M. and Tamayo, P., *Int. J. Mod. Phys. C*, in press.
- [9] Guenoun, P., Perrot, F. and Beysens, d., *Phys.Rev.Lett.* **63**, 1152 (1989).
- [10] Wang, J.S. and Swendsen, R.H., *Physica A* **167**, 565 (1990).



## MODELLING WITH THE COMPUTER AT ALL AGES

JON OGBORN

Professor of Science Education  
Institute of Education University of London

**ABSTRACT** -The paper discusses how modelling with the computer can help Physics Education, for students in a wide age range, from Primary School to University. Different kinds of computational modelling, including iterative dynamic models, qualitative models and object-oriented models are discussed, with examples. It is argued that the different types of models fit naturally into a developmental sequence, matching modelling at various ages to student's intellectual abilities. A radical re-sequencing of teaching about Mathematics in Physics is proposed. Similar ideas are discussed in Ogborn 1990 and 1991.

### 1 Making models on the computer

An example is often the best way to see something general. So let us begin by making a model. Consider something which interests most people: how to get money, specifically money for one's department. All departments argue for more money in the coming year than they had in the previous year. Suppose to begin with that the increase is constant in each year. To model this in the modelling system we call 'Cell Modelling System' or CMS (Ogborn and Holland 1986), we define three computational cells which are rather like the cells of a spreadsheet, as in Figure 1.

Each cell has a name of a variable in the first slot, and says how to calculate that variable in the second slot, using other

variables if required. Thus 'money' is calculated by adding 'increase' to the current value of 'money'. The cell 'increase' defines a constant value (100).

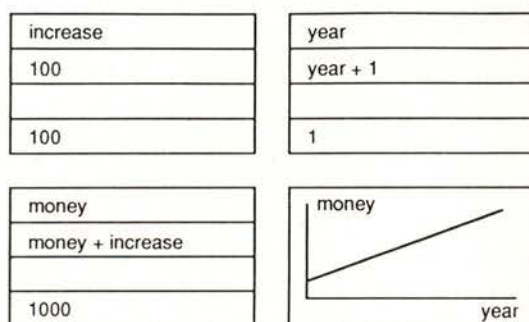


Fig. 1 A primitive model for increasing money

The value of the variable appears in the last slot, putting any initial value required in that slot before running the model. (The third slot, unused in Fig-

ure 1, is for comments.) When the model runs, the cell calculations iterate. Thus 'year' increases by unity at each iteration, and 'money' increases linearly from the initial value 1000, adding 100 on each iteration. Any cell can be converted into a graphics display, plotting any one variable against any other. The

graph cell in figure 1 shows the linear increase of money with time.

Of course, no department is satisfied with this! The large departments say that the increase should be in proportion to the money they have already. How big the multiplying factor is depends on how fiercely they argue. Figure 2 shows the disastrous model that results.

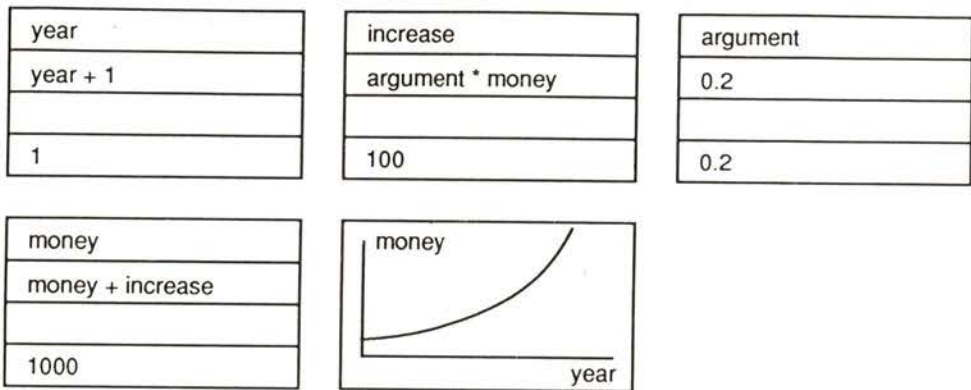


Fig. 2 Exponential increase

If the argument is strong enough to get a 20 percent increase each year, the money grows exponentially. A wise administration realises that this will grow without limit until all the resources of the institution are absorbed. However, exponential growth models are very relevant in for example bacterial growth and epidemics, while the corresponding exponential decay models are relevant in Physics to radioactive decay and to charge on capacitors.

Suppose that a money limit is imposed, such that the increase calculated in Figure 2 is further multiplied by a factor  $f$

such as  $(1 - \text{money}/\text{limit})$  so that as the money approaches the limit, the increase is reduced until at the limit it is zero. Figure 3 shows the resulting model.

Figure 3 is logistic growth, common in population studies where a population initially grows exponentially until it starts to run out of food or space. As is now well known, logistic growth models can exhibit chaotic behaviour at large growth rates. If the parameter 'argue' in Figure 3 is made equal to about 2.0, the graph bifurcates and oscillates above and below the 'limit'. At 'argue' = 2.5 the

bifurcation has bifurcated, and at about 2.9 the graph goes up and down chaotically (see Figure 4). This behaviour, studied by Feigenbaum on a pocket calculator, was an important source of our

current ideas about chaos. Thus in a few simple steps we have gone from the trivial case of a linear increase, known to any child in secondary school, to near the edge of part of modern mathematics.

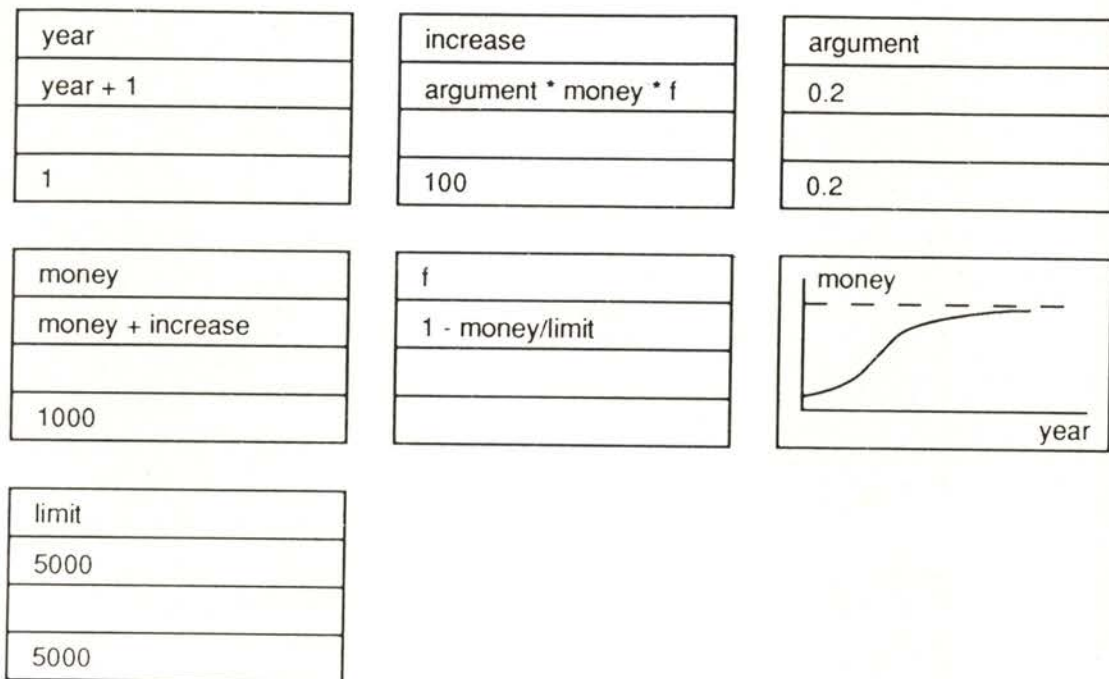


Fig. 3 Logistic growth model.

To take another example, it is not hard to make the Lorenz model of convection currents in a fluid heated from above (see e.g. Marx 1987), as shown in Figure 5.

Air near the ground is warmed and rises, while air high in the atmosphere is cooled and falls. When the warm air has risen it is cooled, and when the cool air has fallen near the ground it is warmed, so the convection can continue.

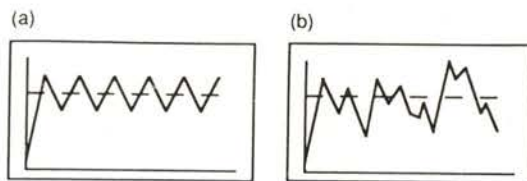


Fig. 4 (a) bifurcation (b) chaos

But if the convection is rapid, warm air is carried over the top of the convection

cell without having time to cool, and cool air is carried over the ground without warming. If cool air starts going up and warm air starts coming down, the convection rate will reduce or may even reverse.

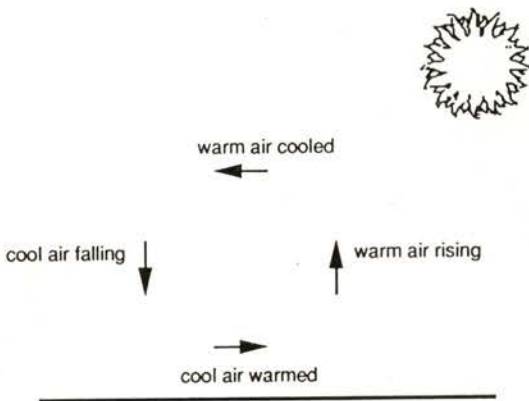


Fig. 5 Convection current in atmosphere

An idealised form of the Lorenz equations relating the rate of circulation to the horizontal and vertical temperature gradients is:

$$\begin{aligned} dx/dt &= 10(y - x) \\ dy/dt &= -xz + 28x - y \\ dz/dt &= xy - (8/3)z \end{aligned}$$

and is easy to put into a modelling system such as that described here, and will generate the well known Lorenz strange attractor if  $x$ ,  $y$  and  $z$  are plotted against one another.

## 2 DINAMIX: another modelling program

DINAMIX is a modelling system developed in Portugal in the project MINERVA by Vitor Duarte Teodoro of the Technological University in Lisbon. Unlike CMS, in DINAMIX models are expressed directly as differential equations.

As in Figure 6, a model in DINAMIX is written by giving one or more differential equations, specifying initial values and constants, and asking for graphs. A stroboscopic graph option makes it possible to show the motion as well as graphs of speed and position against time.

Figures 7 and 8 show how the very elementary model of Figure 6 can be developed into a model of a harmonic oscillator.

Such a progression suggests how a computer modelling program can be used to teach calculus. Simple models like Figure 6 introduce the idea of a derivative, and relate the derivative to the slope of a graph. In the model of Figure 7 the derivative itself has a derivative, so that the slope of the graph of  $x$  against time is continually changing. In Figure 8, the rate of change of velocity is itself determined by  $x$ , which is changing. We have a negative feedback loop, from displacement to rate of change of velocity, which determines

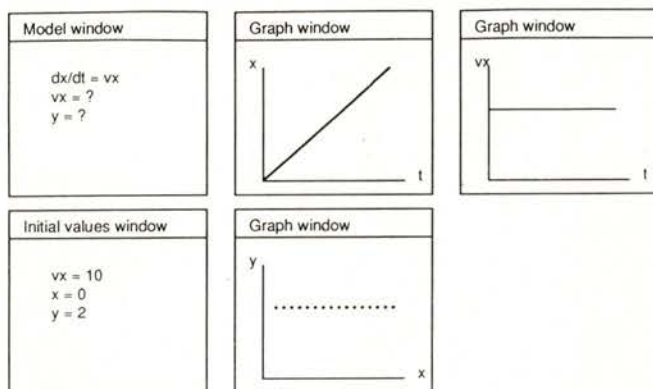


Fig. 6 DINAMIX model of constant velocity

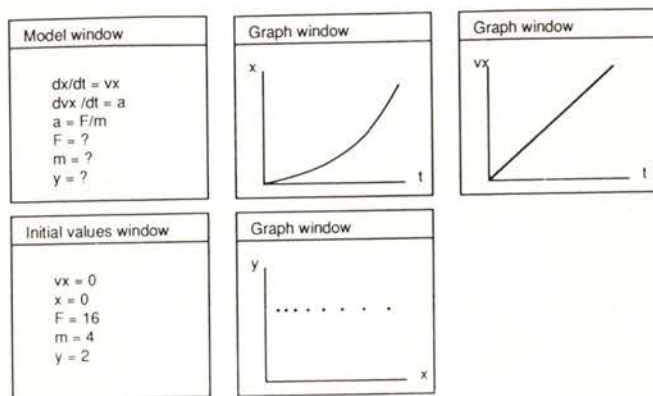


Fig. 7 DINAMIX model of constant acceleration under a constant force

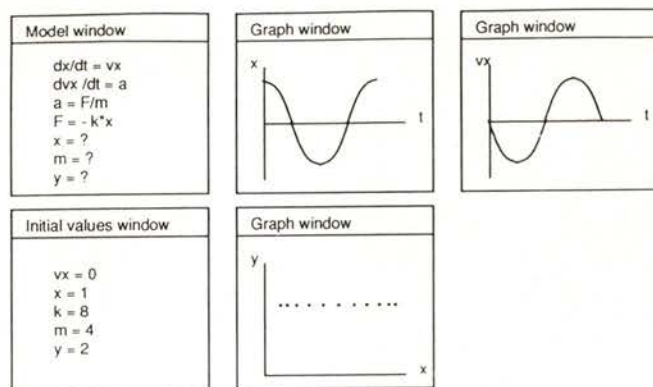


Fig. 8 DINAMIX model of harmonic oscillator

the velocity, which itself determines the displacement. As in other cases we will see later, this is an example of a general system principle:

*negative feedback plus delay gives oscillation*

<i>System</i>	<i>machine</i>	<i>country</i>
Dynamic Modelling System	BBC/IBM	UK
Cell Modelling System	BBC/IBM	UK
DINAMIX	IBM	Portugal
STELLA	Macintosh	USA

### 3 Iterative dynamic models

All the models we have looked at so far are iterative dynamic models (Roberts et al 1983). Several systems for iterative dynamic modelling exist, amongst them:

The Cell Modelling System (Ogborn and Holland 1986) came after our earlier Dynamic Modelling System (Ogborn 1984). STELLA (1987) exploits the graphic capabilities of the Macintosh microcomputer. However, if one has no access to such a system and wants to

avoid direct programming, the best solution is to use a commercial spreadsheet (Folha de Calcul) such as EXCEL (Ogborn 1986). Just to make the point, Figure 9 shows a model of radioactive decay built with a spreadsheet.

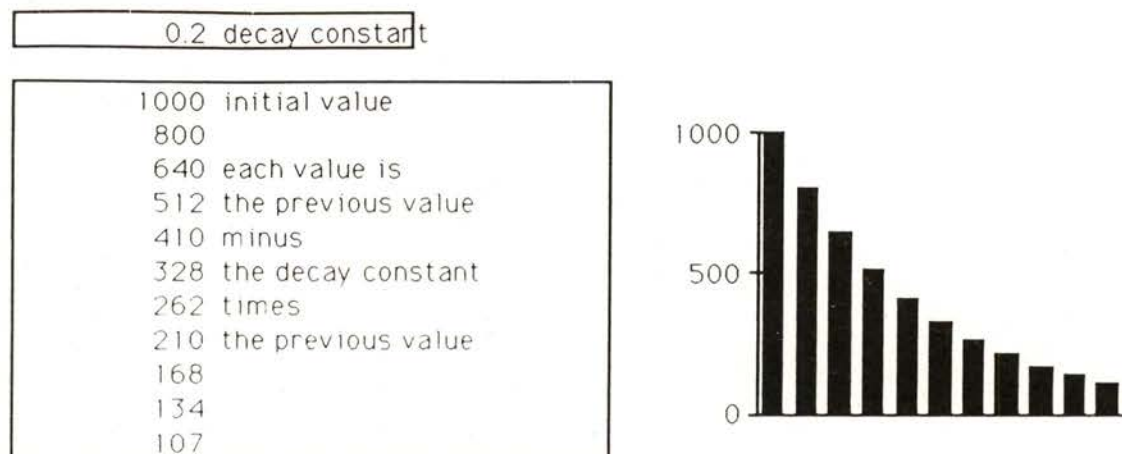


Fig. 9 Spreadsheet model of exponential decay

These modelling systems are suitable for any problem involving solving differential equations or finite difference equations, which is to say, a great number of problems in Science in general and in Physics in particular. Relevant applications include:

### Physics

#### Mechanics

Projectiles, Planetary motion,  
Oscillator, Relativistic motion

#### Electricity and magnetism

RC circuits, LR circuits, LRC circuits,  
particles moving in electric and  
magnetic fields

#### Optics

Two slit interference, Diffraction at a  
slit, Diffraction grating

#### Heat

Conduction

### Chemistry

#### Reaction rates

Temperature dependence,  
Concentration dependence

#### Equilibria

Pressure dependence, Temperature  
dependence

#### Analysis

Titration, pH

#### Transport

diffusion, effusion, pumping

### Biology

#### Populations

exponential growth, limited (logistic)  
growth

#### Ecology

competition between species,  
interdependence of species

#### Animal and plant biology

energy balance of organisms, animal  
and plant growth

#### Cell biology

enzyme reactions, cell growth, nerve  
impulses

#### Applied and general problems

Road traffic

Home heating

Electricity supply and demand

Nuclear power stations

Diet and slimming

The general concept of iterative dynamic modelling is to identify important variables which describe a system, and formulate how they change in time as a result of the values of other variables and constants. The rules for evolution of a system are thus the rules for computing the next value of each variable. Such equations may have, but will not always (or even often) have, analytic solutions. The tradition in Science teaching has for a long time been to focus exclusively on those equations which do have analytic solutions. Let us compare the advantages and disadvantages of the computational and analytic approaches:

*Computational solutions*

Steps close to physical reality

Accessible early in learning

Adding complexity is easy

Only particular solutions

*Analytic solutions*

Formal methods of integration

Needs previous mathematics

Adding complexity is difficult

General, manipulable solutions

In general, each step of a computational solution corresponds to some real physical relationship or process, and so has a direct interpretation in reality. The computational process reflects the physical process. The same can not be said of the procedures used to obtain analytic solutions: nothing physical corresponds, for example, to the process of integration by parts. For these reasons, computational solutions are accessible earlier in learning, since learning the Physics is also learning the steps in the solution, while to obtain analytic solutions one normally needs other prior mathematical knowledge of functions and of methods of integration.

Because the existence of analytic solutions is very sensitive to the detailed structure of the differential equations (in particular often requiring them to be linear) adding a small real life complexity to a problem may produce a very sharp rise in the mathematical difficulty of

solving it. Adding damping to an oscillator makes solving the equations harder, and adding non-linear damping may make an analytic solution impossible. By contrast, in computational solutions, adding complexity will often only add a line or two to a program. Figure 10 fancifully sketches a relation between the difficulty of getting a solution and the amount of reality the model includes.

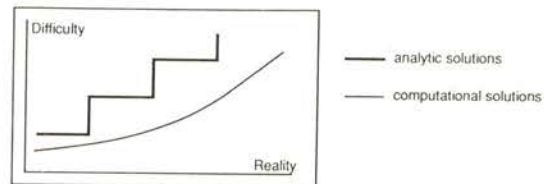


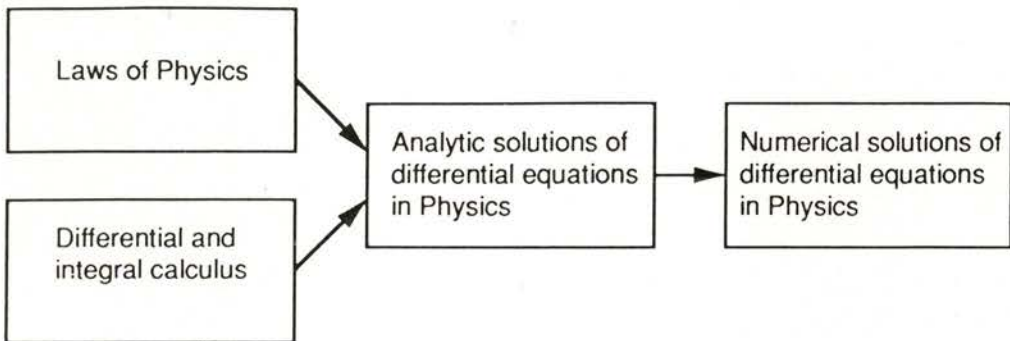
Fig. 10 Difficulty and reality

There is, however, a very good reason for the dominance of analytic solutions. An analytic solution, expressed in a closed form mathematical expression, is quite general and can itself be manipu-

lated and operated on. By contrast, computational solutions are always particular cases. One can move some way towards generality by varying parameters to generate families of solutions, but the computational solutions remain as displays of results rather than manipulable mathematical expressions. Thus analytic solutions will always have an

important role to play. They are like diamonds, uniquely valuable, but rare and costly. The question is not whether to do without them in favour of computation, but when and how to include them. Figure 11 contrasts the common traditional sequence of teaching with one which might serve us better (Ogborn 1989).

(a) traditional sequence



(b) a better sequence?

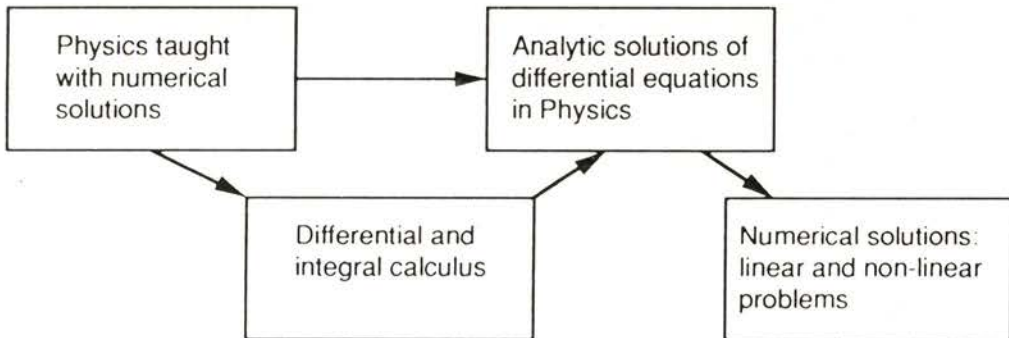


Fig. 11 Traditional and computational learning sequences

Traditionally, we teach Physics and some calculus alongside one another, so as later to be able to develop analytic solutions for differential equations in Physics. Much later, perhaps only in graduate school, is the student introduced to numerical methods. The alternative, which I believe would be better, is to teach Physics by means of some very elementary numerical methods, and to use this to develop the ideas of the calculus so as later to develop analytic methods and numerical methods in parallel.

#### 4 Modelling without mathematics

Up to now, what has been suggested is hardly revolutionary, and fits well with the nature of modern Physics. The next suggestion is however more shocking: it is that we need to begin modelling without, or with the absolute minimum of, mathematics. Consider what is needed if one is to make models of the kind discussed so far:

- 1 Imagining the world constituted of *variables*
- 2 Conceiving physical relations as *mathematical relations* between variables
- 3 Giving appropriate *values* to variables
- 4 Seeing a model as a *structure* with *possibilities*.

Of these, the first is perhaps the hardest. As Physicists we have become so used to imagining the world as analysable as the interaction of quantitative variables that we forget what a huge step in imagination this is. There is good evidence, supported by commonsense observation, that young students see the world as built of *objects and events*, not as built of variables.

We have built, and tested with students in the age range 12-14 years, a modelling programme which focuses just on imagining variables and the connections between them, without having to specify the form of mathematical relations. It was developed in the project *Tools for Exploratory Learning*, in association with Joan Bliss, Rob Miller, Jonathan Briggs, Derek Brough, John Turner, Harvey Mellor, Dick Boohan, Tim Brosnan, Babis Sakonidis, Caroline Nash and Cathy Rodgers. The background to this project is given in Bliss and Ogborn (1988, 1989). The design of the modelling programme is in Miller et al (1990) and results are discussed in Bliss, Ogborn et al (1992) and Bliss and Ogborn (1992).

The modelling system is called IQON (Interacting Quantities Omitting Numbers). In IQON one creates and names variables, and links them together graphically. Again, the best introduction may be by example.

Figure 12 shows what the previous example of an oscillator looks like when expressed in IQON.

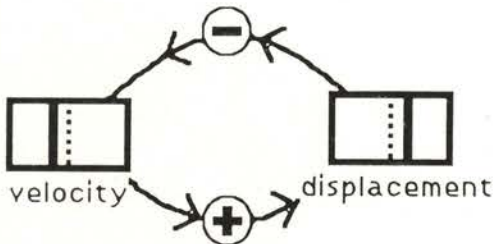


Fig. 12 An oscillator in IQON

A positive velocity progressively increases the displacement, through the 'plus' link. But a positive displacement progressively *decreases* the velocity, through the action of a spring, represented via the 'minus' link. The outcome is that the system oscillates, an example of the principle mentioned before, that negative feedback plus delay gives oscillation. What is shown in Figure 12 is all that the user has to do: to create and name two variables and to link them as shown. No equations are written at all.

However, IQON is also intended for thinking about systems where we have much vaguer ideas about quantities and their relationships. Consider the quality of this very meeting. We may imagine that much depends on the quality of the workshops. If that is high, the participants become happier and happier as the week goes by. But if they are happy they may perhaps participate more ac-

tively in workshops, so that the quality of workshops itself increases. Figure 13 shows this idea expressed in IQON.

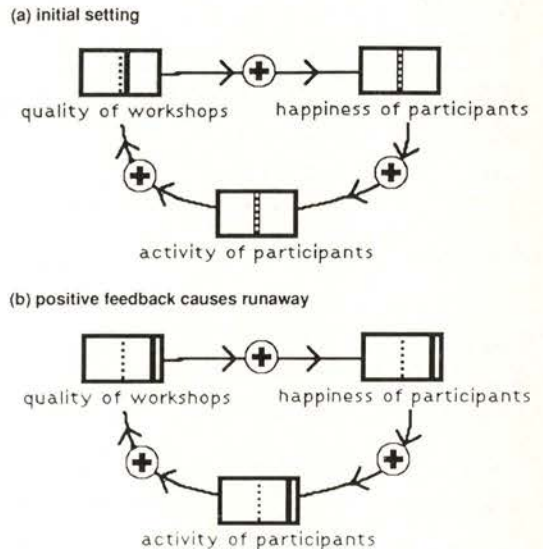


Fig. 13 An IQON model for success of workshops

This model is notably optimistic. It contains positive feedback, so that if as in Figure 13(a) the quality of workshops is somehow increased by a small amount, then after some time all the variables are driven to their positive limits. It does not matter whether the model is correct; what matters is that such effects are possible and will certainly arise in some cases, whatever the details of the system. An increase in global temperature causing melting of polar ice, which by reducing reflectivity increases the energy absorbed from the

Sun and so leads to a further increase of global temperature is an example.

In its present implementation, all IQON variables are alike. Any input from other variables simply modifies the rate of increase or decrease of a variable. Each has a central 'neutral' position at which its output has no effect. Figure 14 shows this schematically.

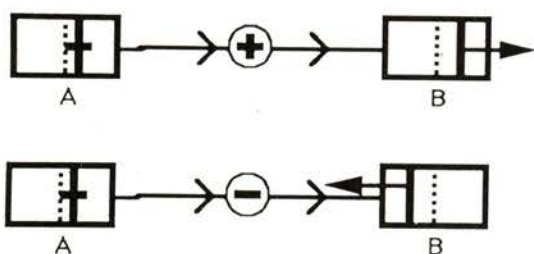


Fig. 14 Behaviour of linked variables in IQON

If variable 'A' is above 'neutral', a positive link from it to variable 'B' drives 'B' up progressively until it reaches the limit of its box. Similarly, a negative link to 'B' drives 'B' progressively down. Thus 'A' determines the rate of change of 'B'. Multiple inputs to a variable are simply averaged, taking account of sign, to determine the rate of change, though some inputs can be given greater weight than others. The response of each variable is made non-linear, through a 'squashing function' which restricts its values to the range minus one to plus one. A variable also has some (adjustable) internal damping. In fact, the behaviour is similar to that of some

forms of artificial neuron (McClelland and Rumelhart 1987). One may of course also regard a variable as a (non-linear) integrator of its inputs.

These features mean that any system of inter-linked variables a user designs will have a smooth behaviour, with no tendency for variables to go to infinity or to produce large step function outputs, and that any system will have a unique stable condition from a given starting point.

Figures 15 and 16 show two examples of models created by pupils aged about 13 (Bliss and Ogborn 1992).

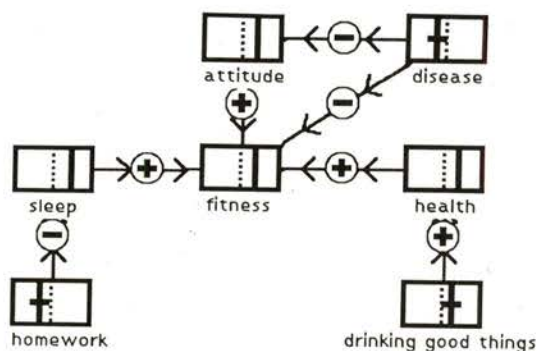


Fig. 15 Nancy's IQON model for keeping fit

Nancy (Figure 15) sees fitness depending both on general health and on whether one is getting plenty of sleep, and additionally on attitude. Jokingly, she says that if the school gives her a lot of work to do at home she gets less sleep. Health she sees as affected posi-

tively by sensible diet and negatively by disease, in both cases sliding a little away from quantitative variables towards events. Disease has a direct negative effect on fitness, and also an indirect effect via attitude. The point is not whether Nancy is right, but that she has produced a model which is discussable, and whose results when run may surprise her and lead her to think some more.

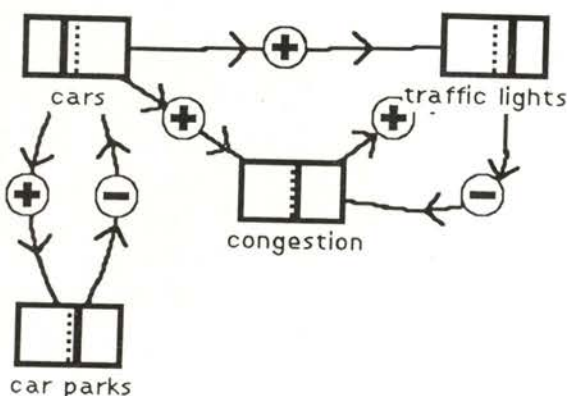


Fig. 16 Burgess' IQON model for traffic congestion

Burgess (Figure 16) was modelling traffic congestion. His 'variables' are more like objects than like amounts of something. Because of the feedbacks in the model, when it is run it can give surprising results. Increasing 'car parks' can at first decrease 'congestion' but, because of the loops between 'cars' and 'car parks' and between 'traffic lights' and 'congestion', the model is liable to oscillate. Again, what matters is that this is likely to lead the pupil to reconsider ideas.

Overall, the results of our studies with IQON (Bliss and Ogborn 1992) can be stated as follows:

- all pupils could make *some* model
- half or more made models with fairly sophisticated interconnections
- those who *made their own* models were more radical in criticising or reformulating them than were those who were given previously prepared models
- many had difficulty creating amount-like variables. The tendency was to create *objects* and *events*.
- some pupils could argue about feedback effects
- most pupils' work produced *discussable ideas*, capable of leading to progress in modelling.

In summary, we have a simple graphic modelling facility, for pupils to build such models out of just a few building bricks, and for them to be able to see some of the basic qualitative interactions at work, without yet having to consider exact functional relations between variables. The significant information is in the *qualitative pattern of relationship and change* amongst variables.

In Physics, one might *begin* with such qualitative models. Later, it would be time to see how well defined relationships in similar models can give more precise answers, in numerical simulations.

### 5 Modelling with objects and events

If one wants to make computational models with young pupils - say 8 to 12 years - then it would seem to be a good idea to model not variables but objects

and events. We have been developing a modelling system for this purpose, called WorldMaker (Boohan, Ogborn and Wright, forthcoming).

A WorldMaker model of sharks preying on fish might look like Figure 17.

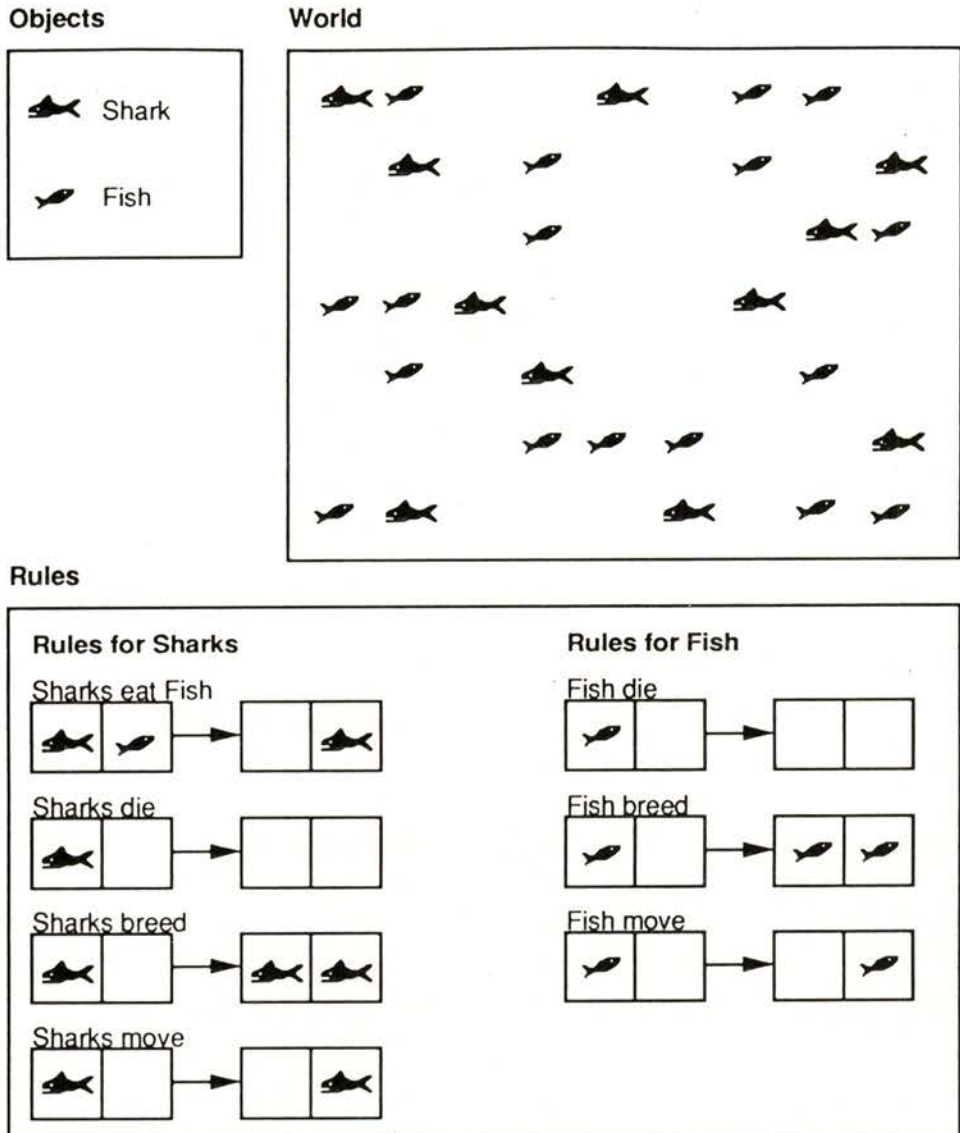


Fig. 17 Predator and prey in WorldMaker

A WorldMaker world consists of objects on a grid. Rules telling the objects what to do are defined graphically. Thus in Figure 17, the two kinds of object, sharks and fish, swim around the grid, being placed on it using drawing tools. Rules are specified by drawings, too. A shark next to an fish eats the fish. A shark on its own may die. A shark next to an empty space may breed or may move. The three rules for fish are similar to the last three rules for sharks. All rules have the form 'condition - effect'. Any rule can be set to 'fire' with a probability selected by a slider bar, so that for example relative breeding rates can be altered, or sharks can be made very long-lived. In this model, if sharks breed too fast, they can destroy the fish population and then themselves die out. As is well known, such predator-prey systems can oscillate. The concept of WorldMaker derives from that of Von Neumann's cellular automaton (one of the best known instances being Conway's Game of Life), with the addition of moving objects each of which retains its identity, and of the possibility of random choices of allowed changes. A cell automaton consists of an array of cells, each of which has a small finite number of states. The state of a cell changes in relation to its own present state and those of its immediate neighbours. Thus the rules for evolu-

tion of the system are local rules, the same everywhere. A useful general account is given by Toffoli and Margolus (1987).

The system as a whole is not represented explicitly at all, but is visible to a person watching the model evolve, as some pattern of behaviour of the assembly of objects.

A simple model suitable for young pupils addresses the question why buses in town always seem to come in groups. Figure 18 shows the idea.

If buses stop to pick up people when they are there, the buses soon become clustered on the road around which they travel. WorldMaker allows directions of movement to be given to an object by the background it is on, making it simple to construct paths or tracks for objects. The example illustrates one of the several ways in which backgrounds and objects can interact, which include either changing the other into a different one. An example of such changes is a 'farmer' who moves around the grid 'planting crops' (i.e. changing bare earth to plants) and one or more 'pests' who move around destroying the crops. Another is shown in Figure 19, in which a creature moves purely at random, but moves frequently in the 'light' and rarely in the 'dark'. The result is that any initial distribution of creatures ends up with most of them in the 'dark' region.

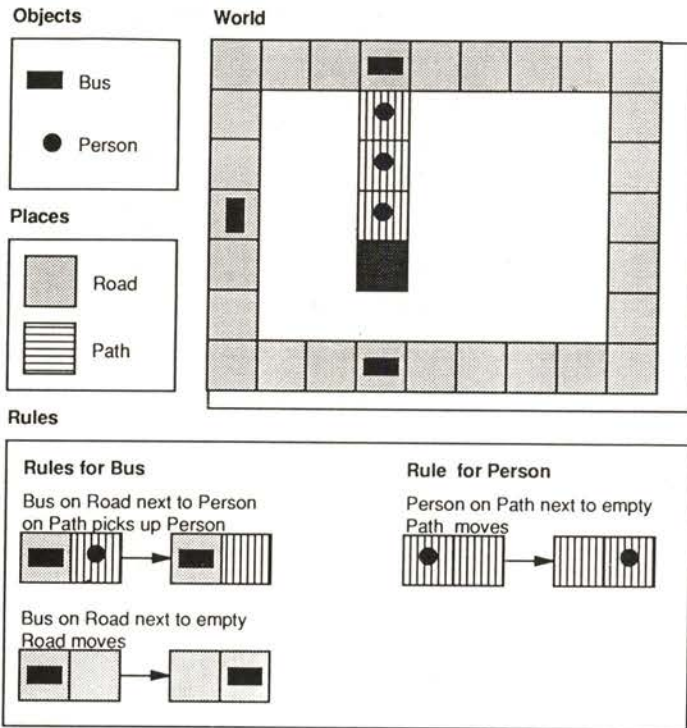


Fig. 18 WorldMaker for buses travelling in groups

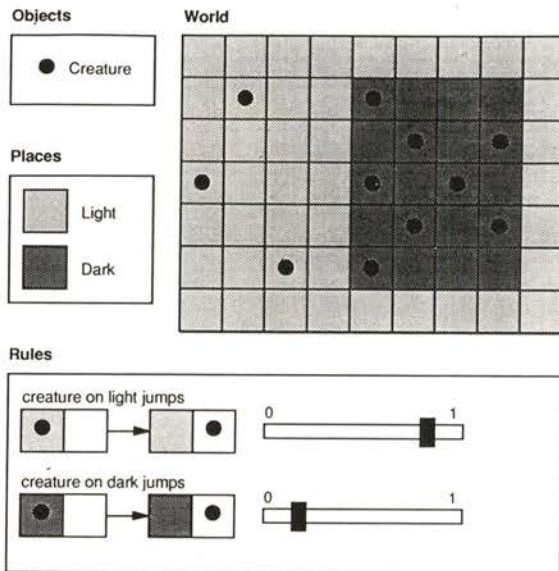


Fig. 19 WorldMaker model of preferential random distribution

An even simpler system, is able to illustrate molecular diffusion, as in Figure 20. The walls can be drawn anywhere one likes, and the initial distribution can be varied. The educational lesson here is important. A large scale, macroscopic appearance of systematic change can be generated by what is at the microscopic level random. Exactly the same rule will produce the outward diffusion of particles placed in a cluster at the centre of an otherwise empty screen.

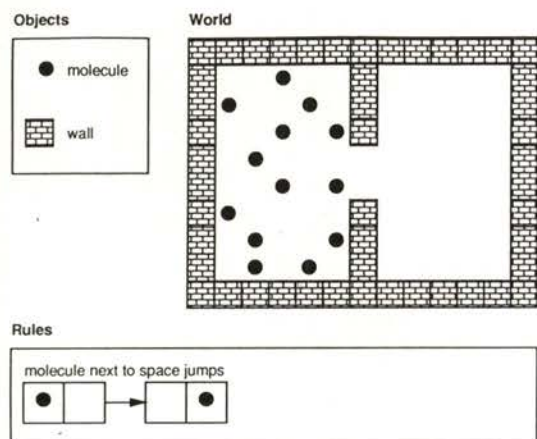


Fig. 20 WorldMaker model of molecular diffusion.

An adaptation of the model in Figure 20 leads to a model of diffusion limited aggregation. One just adds another object, a seed, which does not move, and the additional rule that a molecule alongside a seed is captured and turns into a seed. Figure 21 illustrates the kind of fractal structure which can re-

sult. It is not as impressive as the examples given by Professor Stauffer in his lecture (this issue) but students or teachers can make the model themselves. Other examples mentioned by Professor Stauffer can also be modelled, including cloud formation and the Ising model.

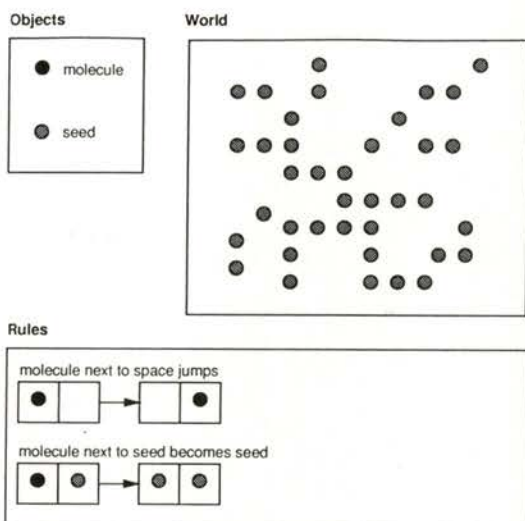


Fig. 21 WorldMaker model of diffusion limited aggregate

Let us mention some other models, simple and more advanced, which WorldMaker makes possible. One is radioactive decay, in which the rule is simply that an object representing a nucleus has a finite probability of changing to a stable nuclide. Such a model is readily extended to a decay chain.

Marx (1984) gives the example of a forest fire, which belongs to the large class of percolation problems. A cell can be empty, or can contain a tree which is alive or is burnt. Trees are placed at random with a certain density over the screen, and one of them is 'set on fire' (figure 22). A tree burns if one or more of its neighbours burns. Will the fire travel all through the forest? It turns out

that there is a critical density of trees for this to be likely. An equivalent problem is that of whether a mixture of conducting and insulating grains will be conducting, or of whether there are continuous percolation paths for oil through cracked rock strata. Marx (1984, 1987) gives many other interesting similar ideas.

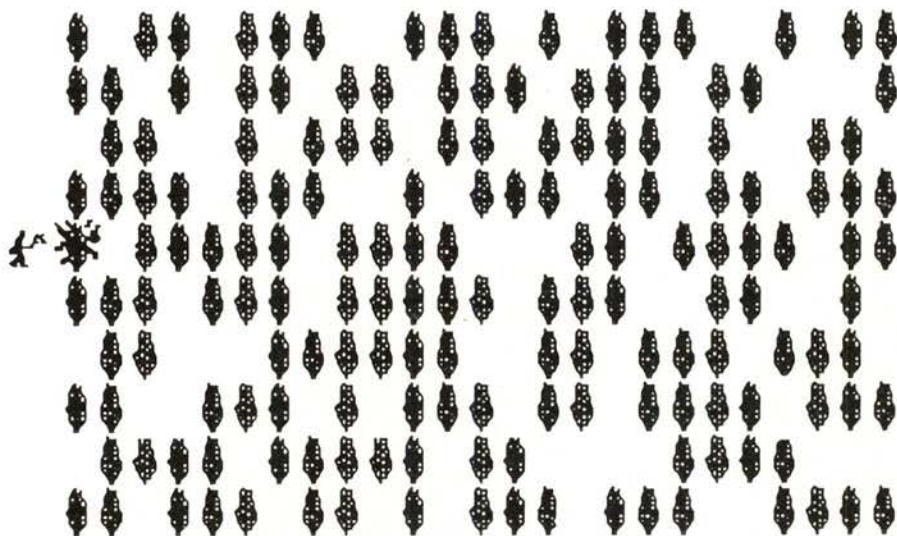


Fig. 22 Forest fire: one tree is set on fire - will all the forest burn?

Simple examples of chemical reactions can be modelled by having cells filled with two or more species of 'molecule'. Molecules may move to empty cells or may combine with others nearby to make product molecules, which themselves may react in the reverse direction.

In teaching thermodynamics, use can be made of models in which energy quanta move from particle to particle at random. Atkins (1984) describes a simple model in which cells have only two energy states, which offers an elegant introduction to temperature as understood statistically.

All these models have the great advantage that the *objects* one is talking about are directly represented on the computer screen. If the work concerns sharks eating fish, there are icons of sharks and fish to look at. If the problem is about molecules, one looks at an array of entities representing molecules, not at a display of variables such as temperature and pressure (though the system might in addition calculate these). The behaviour of the whole system is represented to the student by the visible pattern of behaviour of the objects, not as values of system variables. In general, the rules for the behaviour of entities are simple and intuitive, usually relating directly to their behaviour in the real world. Despite this simplicity, quite complex and analytically intractable systems can be studied.

## 6 Conclusions

I have in this paper suggested three things:

(a) that there is an important role in science teaching for quantitative system modelling;

(b) that there is scope for qualitative computational modelling of systems of variables.

(c) that use can be made of models which manipulate the objects in a system

rather than the variables, and that cell automata provide a useful formalism for this concept;

Systems to provide for (a) already exist, and are in use in some schools, mainly in the upper age range. Those who cannot get or afford such a system, or who prefer an alternative already known to many pupils, can do a great deal with a spreadsheet program. The possibility is opened up of teaching Physics through modelling without having to wait until students know the calculus, and indeed of teaching the calculus in this way.

Suggestion (b) is more radical. We have built and tested a prototype, and can say that with it quite young pupils can produce interesting models. There are good psychological reasons for thinking that qualitative reasoning about variables is important, because of its pervasiveness in all human thought. The opportunity offers for teaching quite young students about systems of variables and effects of feedback, before they are ready to deal with quantitative formalised relations between variables.

Plenty of simulations which belong within the concept of (c) already exist, and are not difficult to program, though speed may be a problem. What I have suggested is the value of a generalized facility for building such models, and I have described one such system. Here we can see how the idea of modelling could be extended to pupils even in the Primary School.

I have tried to take a very broad view of what modelling with the computer might be, in the context of education. Thus let me finally try to put these thoughts in a more general perspective.

I will begin by noting that the normal order in which people come to appreciate the role of computational models, is far from ideal. The normal order is that first one is supposed to learn functional relations between quantities (Ohm's law, Newton's laws etc.), then some differential calculus, then integration, then numerical methods, and finally one is expected to see the unity in all this. This path is followed hardly any distance by most pupils, and the whole distance by almost none except the best doctoral students.

This leads me to propose in a sense to reverse the normal order. We should perhaps concentrate from the beginning on *form*, defined at first loosely and then more precisely. At present we leave form until last, if we ever reach it at all.

If it is true that children would find computational representations of *objects* easier to deal with than representations of *system variables*, then this suggests one kind of beginning with modelling in which the child tells the objects what to do, not the variables. *Form* is then represented by patterns of behaviour of collections of objects.

A second beginning, directed towards analysing systems into related variables, might be with modelling systems supporting qualitative reasoning, or patterns of cause and effect, involving variables. Here one has the possibility of looking at form as the typical kind of behaviour of systems with a given structure. The reason why oscillators oscillate is fundamentally the same. The reasons why stable systems are stable are often basically similar.

Thus, at this general level, I want to emphasize the very real importance, equally for young pupils and for the best experts, of qualitative reasoning about form. The young child can often guess how things may go, and can look at a model on the computer to see if it 'goes right' or not. The expert is an expert just by virtue of having passed beyond the essential stage of being able to do detailed calculations, to have reached the even more essential stage of knowing what kind of calculation to do, and what kind of result it will give.

To create a world, whether constituted of variables or of objects, and to watch it evolve is a remarkable experience. It can teach one what it means to have a model of reality, which is to say what it is to think. It can show both how good and how bad such models can be. And by becoming a game played for its own sake it can be a beginning of purely theoretical thinking about forms. The

microcomputer brings something of this within the reach of most pupils and teachers.

## References

Atkins P W (1984) *The Second Law* W H Freeman

Bliss J, Ogborn J (1988) *Tools for exploratory Learning* Occasional Paper InTER/5/88/: InTER, University of Lancaster.

Bliss J, Ogborn J (1989) 'Tools for Exploratory Learning', *Journal of Computer Assisted Learning*, Vol 5, pp 37-50

Bliss J, Ogborn J, Boohan R, Briggs J, Brosnan T, Brough D, Mellar H, Miller R, Nash C, Rodgers C, Sakonidis H (1992) 'Reasoning supported by computational tools' *Computers in Education* Vol 18, No 1-3, pp 1-9, reprinted in

Kibby M R, Hartley J R (Eds) (1992) *Computer Assisted Learning* Pergamon Press

Bliss J, Ogborn J (1992) *Tools for Exploratory Learning: End of Award Report* (available from the authors)

Boohan R, Ogborn J, Wright S (forthcoming) *WorldMaker* Software, Teachers' Guide and Manual: ESM Cambridge

Marx G (1984) *Games Nature Plays* (with associated software): Lorand Eötvös University, Budapest and National Centre for Educational Technology, Veszprém, Hungary.

Marx G (1987) (Editor) *Welcome to our non-linear Universe*, Volume 1, Proceedings of the International Workshop on teaching non-linear phenomena in schools and universities; Bala-

ton, Hungary April 1987: National Centre for Educational Technology, Veszprém, Hungary.

McClelland J L, Rumelhart D E (1987) *Parallel Distributed Processing*, Vols 1, 2 and 3, Cambridge Mass.: MIT Press

Miller R, Ogborn J, Turner J, Briggs J H, Brough D R (1990) 'Towards a tool to support semi-quantitative modelling' *Proceedings of International Conference on Advanced Research on Computers in Education*, July 1990, Gakushuin University, Tokyo

Ogborn J (1984) *Dynamic Modelling System*, Microcomputer software, London: Longmans

Ogborn J, Holland D (1986) *Cellular Modelling System*, Microcomputer software, London: Longmans

Ogborn J (1986) 'Computational Modelling in Science', in Lewis R, Tagg E *Trends in Computer Assisted Learning*, Oxford: Blackwell

Ogborn J (1989) 'Computational modelling: a link between Mathematics and other subjects' in Blum W et al *Modelling, Applications and applied problem solving* Ellis Horwood

Ogborn J (1990) 'Modellizzazione con l'elaboratore: possibilità e prospettive' *La Fisica nella Scuola*, Anno XXIII, n. 2 pp 32-43

Ogborn J (1991) 'Modelação com o computador: Possibilidades e perspectivas' in Teodoro V D, de Freitas J C (eds) (1991) *Educação e computadores* Ministério da Educação: Lisbon, Portugal

Roberts N, Anderson D, Deal R, Garet M, Shaffer W, (1983) *Introduction to Computer Simulation*, New York: Addison Wesley

STELLA (1987) High Performance Systems,  
13 Dartmouth College Highway, Lyme, New  
Hampshire, 03768, USA.

Toffoli T, Margolus N (1987) *Cellular Auto-  
mata Machines: a new environment for  
modelling*, Cambridge Mass.: MIT Press

# COMPUTER SIMULATIONS OF WIDOM'S MICROEMULSION MODEL

D. STAUFFER

Institute for Theoretical Physics, Cologne University, D-W-5000 Köln 41, Germany

**ABSTRACT** - Microemulsions are mixtures of oil, water and "soap" (amphiphilic molecules). The Widom model of 1986 describes them by a spin  $1/2$  Ising model with competing interactions to nearest and further neighbors. We review the Monte Carlo simulations of this Widom model, for static and dynamic properties.

## 1. INTRODUCTION

If poor people wash their dishes or rich people extract crude oil from the earth, in both cases "soap" may help. These soap molecules are called detergents for dish washing and are a part of the "brine" fluid pumped into the rocks for enhanced oil recovery. Thus not surprisingly, scientists at Shell Laboratories in Amsterdam made computer simulations for both problems. And I will report here on simpler simulations of a lattice model for microemulsions invented several years ago by Benjamin Widom[1] at Cornell University, for which together with Naeem Jan (Canada), Debashish Chowdhury (India), and others lots of simulations were made since 1987.

## 2. BASIC CONCEPTS

Microemulsions[2] consist of oil, water, and amphiphilic molecules. These am-

phiphilic molecules have hydrophilic head attracted by water, and a hydrophobic tail attracted by oil. For simplicity we denote the amphiphiles as "soap" molecules. Since they can easily move between oil and water, the soap molecules can drastically reduce the interface tension between the oil phase and the water phase. As a result, one of the possible states of a microemulsion are small oil droplets in water, or small water droplets in oil, where the whole droplet surface is coated by soap to reduce the interface tension. The droplet radii are in the nanometer range; thus the microemulsion is transparent to light, differently from milk. A third possible phase for microemulsions is called bi-continuous, where water, oil, and soap are intermingled together in a non-periodic but also non-random way. A simple computer simulation should use a lattice on which the molecules are moved by a Monte Carlo procedure.

Molecular dynamics simulations where molecules follow Newton's law of motion are usually much more demanding in computer time and programming effort. Each lattice site then carries a discrete variable, called a spin by physicists, which determines which type of molecule sits there. The obvious choice, taken by many authors[2], are three possible states for each spin, corresponding to oil, water, and soap. The elegance of the Widom model[1] and the reason that more Monte Carlo simulations were made for this than for other microemulsion models is that it uses only two states, spin up and spin down. The three types of molecules are then represented by the bonds between neighbor spins on the lattice: Two up spins correspond to water, two down spins to oil, one up and one down spin to soap. The spins are thus either hydrophilic or hydrophobic (molecules or parts of molecules). Also some of the molecular dynamics simulations[3] follow this simplification of only two types of elements; amphiphiles in these simulations are chains of hydrophilic and hydrophobic elements. Simplicity is a matter of taste but I find this Widom model simpler than the later lattice models[2] having at least three states for each spin. Also from the computational point of view the two states per site are easier to store and treat in single bits[4] than three or more states. A disadvantage is that we need now interactions to more than just nearest neighbors. On a square or simple cubic lattice the interaction energy (Hamiltonian) is

$$H = -J \sum S_i S_j - 2M \sum S_i S_k - M \sum S_i S_l, \quad S_i = \pm 1$$

with positive  $J$  and negative  $M$ , where all sums count each pair only once; the first sum goes over nearest neighbors, the second over next-nearest neighbors, and the third over neighbors two lattice constants away. No interaction with neighbors at distance  $\sqrt{3}$  is used, and instead of the factor  $2M$  one has also used a free interaction parameter here. This interaction energy is completely symmetric with respect to spin up or spin down; a difference between oil and water has been obtained by using a field term proportional to  $\sum_i S_i$ . When  $M$  is set to zero we recover the standard Ising model. This model now can be simulated with standard Monte Carlo techniques[5]: A spin is flipped with a probability proportional to  $\exp(-\Delta E/k_B T)$  where  $\Delta E$  is the energy change associated with such a flip. Ref.6 gives dirty tricks to facilitate vectorization. Many other lattice models have been studied but except for the three-phase coexistence to be discussed below few qualitative differences between their phase diagrams and those of the Widom model seem established. Thus we ignore them here and try to review only all simulations of the Widom model. Mean field theories[7] of the Widom model are useful qualitative guides but may give transition temperatures differing by a factor three from the simulation

value; they may also have difficulties in distinguishing between first and second order phase transitions. Since this conference is for physicists, we will use mainly a magnetic language to describe the Widom model results. Ferromagnetism with a positive (negative) spontaneous magnetization then corresponds to a water-rich phase (an oil-rich phase), paramagnetism to a more or less random mixture of water and oil. In both cases, soap separates the oil molecules from the water molecules. The Curie temperature corresponds to the demixing temperature; for lower temperatures oil and water no longer mix homogeneously.

### 3. EQUILIBRIUM

To describe the results at finite temperatures we use Widom's notation  $j = J/k_B T$  and  $m = M/k_B T$  to describe the phase diagram. In three dimensions for  $m = 0$  we get the second-order Ising transition at  $j = 0.221656$  between a ferromagnet and a paramagnet. For negative  $m$  ferromagnetism is becoming more difficult, and the phase transition temperature is diminished ( $j$  increases). At about  $j = 0.9$ ,  $m = -0.09$  a higher order critical point is reached, and from then on the phase diagram becomes more complicated[8]. Near that higher-order point the interface tension gets very small[8], as required for microemulsions. We increase the positive ratio  $r = -m/j$  and then for a fixed  $r$  de-

crease the temperature (increase  $j$ ). Then for small  $r$  up to 0.1 we find the above-mentioned second order phase transition from paramagnetism to ferromagnetism. For large  $r$  we find first-order phase transitions to various periodic phases, like one plane of spins up, the next plane down, and so on in an up-down period of length two. These periodic phases are expected to depend on the lattice structure and are thus hardly realistic; we might identify them with liquid crystals. The transition between ferromagnets and paramagnets, on the other hand, is known to occur also without a lattice in a similar way[9] and thus is much less determined by the lattice approximation of the Widom model. Therefore for a discussion of microemulsions we restrict ourselves to ratios  $r$  between zero and about 0.1. (In two dimensions the phase diagram is similar but somewhat simpler[10,11].) Most of the phase diagram of ref. 8 was confirmed by the simulations of ref. 12. Near  $j = 1.1$ ,  $m = -0.12$  some discrepancy appeared (ferromagnetism or layered phase?), with ref.5 later reconfirming ref.8. With a low-temperature perturbation expansion, ref.12 found a phase with period six: Three planes of up spins followed by three planes of down spins, and so on. This phase was not found in the Monte Carlo simulations[8,5] perhaps because their temperature was not low enough. (Ref.11

gives the oil, water and soap concentrations as a function of  $j$ ,  $m$ , and "magnetic field".)

Lots of recent Ising research concerns the behavior near solid walls, and also for the Widom model such simulations were made. In particular, is the correlation function (concentration profile) near the wall monotonic or oscillating? The simulations[13] indicate that the concentrations decay monotonically (oscillatory) in the paramagnetic phase if for the same interaction ratio  $r$  at lower temperatures the ordered phase is ferromagnetic (periodic). Perhaps only paramagnetic phases with oscillating correlations should be identified with the bicontinuous phase of microemulsions.

If the free space between the walls gets smaller and smaller, and the walls are replaced by a more disordered geometry, we have microemulsions in porous media: Oil and brine in rocks. The extreme limit is the randomly diluted Widom model, where single sites randomly either carry a spin ( $S_i = \pm 1$ ) or are inert ( $S_i = 0$ ). In this extremely fine "sand" the critical temperature was found to decrease roughly linearly with increasing sand concentration, until at some threshold it seems to vanish, in both two [19] and three[6] dimensions. Monte Carlo simulations are not very suited for the very low temperatures near that threshold; series expansions could be helpful here.

Microemulsions may produce micelles of a fixed size, that means small oil droplets surrounded by soap molecules and swimming freely in the water (or alternatively water drops in oil). Does the ferromagnetic phase of the Widom model show such micelles? Yes and no! The answer is yes if we regard a single spin as a nanodroplet of oil (or water). Then at low temperatures in the ferromagnetic region nearly all spins show in one direction, with very few *isolated* spins pointing oppositely. These isolated overturned spins then correspond to micelles. Of course, such "micelles" occur also in the simple Ising model. If, on the other hand, we identify the single spins with single molecules, then a micelle is a cluster of many parallel spins. And of course, again as in normal Ising models[14], such clusters do exist[8]. But the cluster size distribution decays monotonically whereas experimentally micelles seem to have a preferred size. Note that in molecular dynamics simulations[3] a peak in the cluster size distribution was observed only when the soap molecules were rather long, and not when they were short as in the Widom model.

Another disadvantage of the Widom model is the lack of the experimentally observed three-phase coexistence of oil-rich, water-rich, and bicontinuous phases. So far we may either have coexistence of water-rich and oil-rich phases

(magnetization up and magnetization down), or the bicontinuous phase (paramagnet) alone, since the phase transition is second order. (Ferromagnetic and layered phases may coexist but this is not what we are looking for.) If as a function of temperature one may get a first-order transition, then near that transition ferro- and paramagnet may coexist, leading to the desired three-phase coexistence in the microemulsion model. This property can be achieved by adding a four-spin interaction[15] to the energy.

#### 4. DYNAMICS

This section discusses the bursting of soap bubbles, the mixing process, and electrical transport.

If we look at time-dependent effects we have to distinguish between models with fixed particle numbers (canonical ensemble) and those with fixed interaction constants  $J$ ,  $M$ , magnetic field (grand canonical ensemble). The first method is computationally easier, the second more realistic. But also the first method is adequate if we study nucleation events proportional to  $\exp(-\text{energy}/k_B T)$ .

As we all know, soap bubbles burst after some time. Very thin soap films, called Newton black films, are thought to have a monolayer of water separated from the

air (or a solid) by two layers of amphiphiles. We model this Newton black film by the Widom model (replacing oil by air in our interpretation). Thus we take one layer of down spins on top, one layer of up spins in the middle, and one layer of down spins at the bottom as our initial configuration of the film. In the simulations all these spins can flip up and down with the usual probabilities. The neighbor planes above the upper layer and below the lower layer are kept spin down. Thus initially we have a plane of water molecules separated from the surrounding air by soap.

This configuration was found in our simulations[13,16] to be metastable. Somewhere a hole (small cluster of down spins) is formed in the water layer which then grows and lets the soap bubble burst. However, the lower the temperature was, the longer was the lifetime of this configuration as is shown in Fig.1. For long lifetimes we see a nice Arrhenius law as in standard nucleation theories: lifetime proportional to  $\exp(-E_0/k_B T)$  with some energy barrier  $E_0$  which a hole has to overcome before it can grow and destroy the bubble. The lifetime is much shorter if initially we have already some down

spins also in the (predominantly up) center plane; with 20 percent such down spins the lifetime is very short. This behavior agrees qualitatively with that found experimentally by Exerowa and Kashchiev[17]; no such behavior was found for the simple Ising model,  $M = 1$ . One difference between laboratory and computer experiment is that in the Widom model we did not find completely stable films whereas in experiments their lifetime was found to diverge at some critical water concentration in the central layer. While we had found (see previous sections) periodic layered phases in fully three-dimensional phases, the present set-up with only one water layer is different and apparently not stable. Indeed, when we increase the thickness of the simulated water layer [13] its lifetime increased drastically.

An entirely different question for microemulsions is: Given a vessel with oil on top, soap in the middle, and water at the bottom, how long does it take before we get a homogeneous (bicontinuous) phase? Clearly, we now must use a canonical ensemble where molecules diffuse through the system. Since in the Widom model the molecules sit on the bonds between the spins, it is no longer sufficient (as it is in usual Ising models with fixed magnetization) to flip nearest neighbor antiparallel spin pairs. We must check that the number of up neighbors of the two spins to be flipped are equal (not counting the two spins to be flipped); and only if that is the case may we consider

flipping both spins with the appropriate thermal probability.

As a result, the calculation is quite time consuming. Moreover, the relaxation to equilibrium is quite slow, roughly logarithmically in time[11], as also found in another model [18]. It would be interesting to make experiments to check this pseudo-logarithmic dependence which may arise from the superposition of many exponentially decaying Fourier components due to the normal diffusion law [11].

A third type of dynamics concerns electrical transport: When does an electric current flow through the microemulsion? A simple model assumes that only water carries the current. Then in the Widom model a continuous path of up spins is required to give a finite conductivity. Such percolation transitions are known[14] already in Ising models to be different from the demixing transitions. For the Widom model[20], electrical conduction sets in if the water concentration exceeds about 0.1. Gelatine dissolved in the nanodroplets may couple them to a rigid gel, which is then a third type of transition[20].

#### ACKNOWLEDGEMENTS

I thank Herr Professor Zuckermann for animated discussions about what is the simplest microemulsion model, N.Jan, D.Chowdhury, and A.Aharony for helpful cooperation in this field, and BMFT grant 0326657D and SFB 341 for partial support.

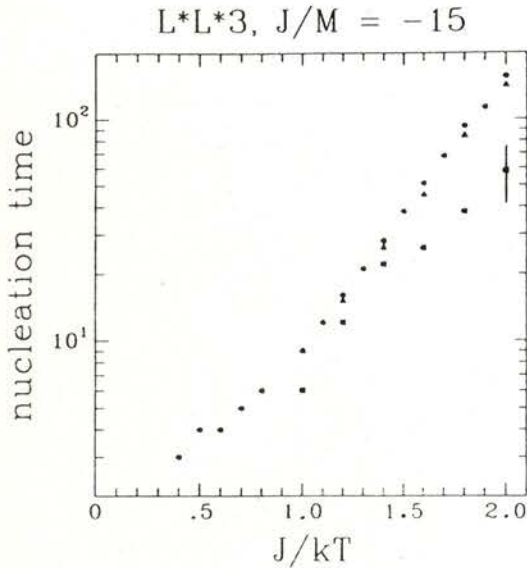


Fig.1: Nucleation time versus inverse temperature for large Widom films. A straight line corresponds to an Arrhenius law. The soap bubble is defined as bursting if the largest hole covers at least five percent of the total area[16].

## REFERENCES

[1] Widom, B., J. Chem.Phys. **84** 6943 (1986).  
 [2] For reviews see Davis, H.T., Bodet, J.F., Scriven, L.E., and Miller, W.G., in: "Physics of Amphiphilic Layers", edited by Meunier, J., Langevin, D., and Boccara, N., Springer-Verlag, Berlin 1987; "Modern Ideas and Problems in Amphiphilic Science", edited by Gelbert, W.M., Roux, D., and Ben-Shaul, A., Springer-Verlag, Heidelberg 1991; Schick M., Physica A

**172** 200 (1991); Matsen, M.D., Schick, M., and Sullivan, D.E., preprint.

[3] Smit B. et al., Nature **384** 625 (1990); J.Phys.Chem. **95** 6361 (1991); and Int. J. Mod. Phys. C, in press (PC '93 conference)

[4] Domrowe, M. and Rommerskirchen, A., project report, Bildungszentrum für Informationsverarbeitende Berufe, Bergisch-Gladbach, April 1992

[5] "Applications of the Monte Carlo Method in Statistical Physics", edited by Binder, K., Springer-Verlag, Heidelberg, 1987

[6] Stauffer, D., Ho, J.S., and Sahimi, M., J.Chem.Phys. **94** 1385 (1991)

[7] Dawson, K.A., Lipkin, M.D., and Widom, B., J.Chem.Phys. **88** 5149 (1988)

[8] Stauffer, D. and Jan, N., J. de Phys.(Paris) **49** 623 (1988)

[9] Wilding, N.B. and Bruce A.D., Phys.Rev.Lett. **68** (1992) 193; Rovere, M., Nielaba, P., and Binder, K., Z.Physik B, in press (1993)

[10] Jan, N. and Stauffer, D., J.Chem.Phys. **87** 6210 (1987)

[11] Morawietz, D., Chowdhury, D., Vollmar, S. and Stauffer, D., Physica A **187** 126 (1992)

[12] K.A. Dawson, B.L. Walker and A. Berera, Physica A **165** 320 (1990)

[13] Chowdhury, D. and Stauffer, D., J.Chem.Phys. **95** 7664 (1991)

[14] Stauffer, D. and Aharony, A., "Introduction to Percolation Theory", Taylor and Francis, London, 1992

[15] Hansen, A., Schick, M., and Stauffer, D., Phys.Rev. A **44** 3686 (1991)

[16] Chowdhury, D. and Stauffer, D., Physica A **186** 237 (1992) and in press (1992)

[17] Exerowa D. and Kashshiev, D., *Contemp.Phys.* **27** 429 (1986)  
[18] Laradji, M., Chu, H., Grant, M., and Zuckermann, M.J., *J.Phys. A* **24** L 629 (1991)

[19] Velgakis, M.J., *Physica A* **159** 167 (1989)  
[20] Stauffer, D., and Eicke, H.F., *Physica A* **182** 29 (1992)

CONTENTS  
FASCÍCULO 1-2

*Enhanced nuclear magnetism*

- B. Bleaney ..... 1

*The problem of spurious color bound states in Nambu Jona-Lasinio type lagrangians*

- Alex H. Blin, Brigitte Hiller and João da Providência ..... 15

*Structure and physical properties of the quaternary phase «Caalsifer» in industrial Fe-Si Alloys*

- F. Margarido and M. O. Figueiredo..... 21

*Electron density studies in the laves phase FeBe<sub>2</sub>*

- M. M. R. Costa, M. J. M. de Almeida and J. A. Paixão ..... 31

*On the quantum harmonic oscillator with time-dependent frequency*

- Francisco M. Fernández and Eduardo A. Castro ..... 39

*The emission measure and ultraviolet spectra of T Tauri stars*

- João J. F. G. Afonso Lima and Maria Teresa Vaz Torrão Lago..... 44

CONTENTS  
FASCÍCULO 3-4

<i>Gaseous detectors in astrophysics, medicine and biology</i>	
Fabio Sauli .....	55
<i>Main properties of the new high <math>T_c</math> superconductors related to thermodynamic fluctuations and to the magnetism of Copper</i>	
J. P. Burger .....	69
<i>Fractals and phase transitions</i>	
D. Stauffer .....	83
<i>Modelling with the computer at all ages</i>	
Jon Ogborn .....	93
<i>Computer simulations of widom's microemulsion model</i>	
D. Stauffer .....	115

## AUTHOR INDEX

ALEX H. BLIN, BRIGITTE HILLER, JOÃO DA PROVIDÊNCIA — The problem of spurious color bound states in Nambu Jona-Lasinio type lagrangians.....	15
B. BLEANEY — Enhanced nuclear magnetism .....	1
D. STAUFFER — Fractals and phase transitions .....	83
D. STAUFFER — Computer simulations of widom's microemulsion model .....	115
FABIO SAULI — Gaseous detectors in astrophysics, medicine and biology .....	55
F. MARGARIDO, M. O. FIGUEIREDO — Structure and physical properties of the quaternary phase «Caalsifer» in industrial Fe-Si Alloys .....	21
FRANCISCO M. FERNÁNDEZ, EDUARDO A. CASTRO — On the quantum harmonic oscillator with time-dependent frequency .....	39
J. P. BURGER — Main properties of the new high Tc superconductors related to thermodynamic fluctuations and to the magnetism of Copper.....	69
JOÃO J. F. G. AFONSO LIMA, MARIA TERESA VAZ TORRÃO LAGO — The emission measure and ultraviolet spectra of T Tauri stars .....	44
JON OGBORN — Modelling with the computer at all ages.....	93
M. M. R. COSTA, M. J. M. DE ALMEIDA, J. A. PAIXÃO — Electron density studies in the laves phase FeBe <sub>2</sub> .....	31



# SOCIEDADE PORTUGUESA DE FÍSICA

AV. REPÚBLICA, 37 - 4.º • 1000 LISBOA • PORTUGAL

PORTUGALIAE PHYSICA publishes articles or research notes with original results in theoretical, experimental or applied physics; invited review articles may also be included.

Manuscripts, with an abstract, may be written in English or French; they should be typewritten with two spaces and in duplicate. Figures or photographs must be presented in separate sheets and be suitable for reproduction with eventual reduction in size; captions should make the figures intelligible without reference to the text. Authors are requested to comply with the accepted codes concerning references.

There is page charge. Author(s) will get 50 free reprints (without covers); these are to be shared among all the authors of the article. Authors interested in more reprints should say so when sending their manuscripts; quotations shall be sent with the proofs.

Subscription rates for volume 21:

3.600 Escudos (US\$24) — individuals

9.000 Escudos (US\$60) — libraries

PORTUGALIAE PHYSICA may also be sent on an exchange basis; we welcome all suggestions to such effect.

All mail to be addressed to

PORTUGALIAE PHYSICA

C/O LABORATÓRIO DE FÍSICA, FACULDADE DE CIÊNCIAS

PRAÇA GOMES TEIXEIRA

4000 PORTO - PORTUGAL

# PORTUGALIAE PHYSICA

VOL. 21 • NUMB 3/4 • 1992

## CONTENTS

<i>Gaseous detectors in astrophysics, medicine and biology</i>	
Fabio Sauli.....	55
 <i>Main properties of the new high <math>T_c</math> superconductors related to thermodynamic fluctuations and to the magnetism of Copper</i>	
J. P. Burger .....	71
 <i>Fractals and phase transitions</i>	
D. Stauffer .....	83
 <i>Modelling with the computer at all ages</i>	
Jon Ogborn .....	93
 <i>Computer simulations of widom's microemulsion model</i>	
D. Stauffer .....	115